

AD-A176 015

12

DNA-TR-86-74

STOCHASTIC EFFECTS ON OBLIQUE HF PROPAGATION

L. J. Nickisch
Mission Research Corporation
P. O. Drawer 719
Santa Barbara, CA 93102-0719

31 January 1986

Technical Report

CONTRACT No. DNA 001-84-C-0253

Approved for public release;
distribution is unlimited.

DTIC
ELECTE
S JAN 14 1987 D
A

THIS WORK WAS SPONSORED BY THE DEFENSE NUCLEAR AGENCY
UNDER RDT&E RMSS CODE B322084466 S99QMXBB00040 H2590D.

DTIC FILE COPY

Prepared for
Director
DEFENSE NUCLEAR AGENCY
Washington, DC 20305-1000

87 1 14 011

Destroy this report when it is no longer needed. Do not return to sender.

PLEASE NOTIFY THE DEFENSE NUCLEAR AGENCY,
ATTN: STTI, WASHINGTON, DC 20305-1000, IF YOUR
ADDRESS IS INCORRECT, IF YOU WISH IT DELETED
FROM THE DISTRIBUTION LIST, OR IF THE ADDRESSEE
IS NO LONGER EMPLOYED BY YOUR ORGANIZATION.



DISTRIBUTION LIST UPDATE

This mailer is provided to enable DNA to maintain current distribution lists for reports. We would appreciate your providing the requested information.

- Add the individual listed to your distribution list.
- Delete the cited organization/individual.
- Change of address.

NAME: _____

ORGANIZATION: _____

OLD ADDRESS

CURRENT ADDRESS

TELEPHONE NUMBER: () _____

SUBJECT AREA(S) OF INTEREST:

DNA OR OTHER GOVERNMENT CONTRACT NUMBER: _____

CERTIFICATION OF NEED-TO-KNOW BY GOVERNMENT SPONSOR (if other than DNA):

SPONSORING ORGANIZATION: _____

CONTRACTING OFFICER OR REPRESENTATIVE: _____

SIGNATURE: _____

Director
Defense Nuclear Agency
ATTN: STTI
Washington, DC 20305-1000

Director
Defense Nuclear Agency
ATTN: STTI
Washington, DC 20305-1000

UNCLASSIFIED

SECURITY CLASSIFICATION OF THIS PAGE

AD-A176015

REPORT DOCUMENTATION PAGE

1a. REPORT SECURITY CLASSIFICATION UNCLASSIFIED		1b. RESTRICTIVE MARKINGS	
2a. SECURITY CLASSIFICATION AUTHORITY N/A since unclassified		3. DISTRIBUTION/AVAILABILITY OF REPORT Approved for public release; distribution is unlimited.	
2b. DECLASSIFICATION/DOWNGRADING SCHEDULE N/A since unclassified			
4. PERFORMING ORGANIZATION REPORT NUMBER(S) MRC-R-974		5. MONITORING ORGANIZATION REPORT NUMBER(S) DNA-TR-86-74	
6a. NAME OF PERFORMING ORGANIZATION Mission Research Corporation	6b. OFFICE SYMBOL (if applicable)	7a. NAME OF MONITORING ORGANIZATION Director Defense Nuclear Agency	
6c. ADDRESS (City, State, and ZIP Code) P. O. Drawer 719 Santa Barbara, CA 93102-0719		7b. ADDRESS (City, State, and ZIP Code) Washington, DC 20305-1000	
8a. NAME OF FUNDING/SPONSORING ORGANIZATION	8b. OFFICE SYMBOL (if applicable)	9. PROCUREMENT INSTRUMENT IDENTIFICATION NUMBER DNA 001-84-C-0253	
9c. ADDRESS (City, State, and ZIP Code)		10. SOURCE OF FUNDING NUMBERS	
		PROGRAM ELEMENT NO. 62715H	PROJECT NO. S99QMXB
		TASK NO. B	WORK UNIT ACCESSION NO. DH008307
11. TITLE (Include Security Classification) STOCHASTIC EFFECTS ON OBLIQUE HF PROPAGATION			
12. PERSONAL AUTHOR(S) Nickisch, L.J.			
13a. TYPE OF REPORT Technical	13b. TIME COVERED FROM 840107 TO 860131	14. DATE OF REPORT (Year, Month, Day) 860131	15. PAGE COUNT 102
16. SUPPLEMENTARY NOTATION This work was sponsored by the Defense Nuclear Agency under RDT&E RMSS Code B322084466 S99QMXB00040 H2590D. > Hg			
17. COSATI CODES		18. SUBJECT TERMS (Continue on reverse if necessary and identify by block number)	
FIELD	GROUP	SUB-GROUP	
4	1		HF propagation, Power spectra, Scintillation
20	6		Ionogram scaling, PSD, Spectral index
			Irregularities, Scattering, Striations
19. ABSTRACT (Continue on reverse if necessary and identify by block number) A model for the calculation of the stochastic effects on transionospheric radio wave propagation due to structured ionization, developed in recent years, under the sponsorship of the Defense Nuclear Agency, has been applied to internally reflected paths at high frequencies (HF). Measurements of signal spreading in the delay and doppler domains obtained by the HF Channel Probe experiment in the polar region were used to test the applicability of the transionospheric scintillation model to oblique, internal HF paths. Oblique soundings made by the Channel Probe experiment provide the ionospheric profile through which rays can be numerically traced and model calculations performed. A nonlinear regression routine is used to obtain model parameters providing the best fit to the data. We find that good fits are obtained and that the resulting model parameters are consistent with independent measurements.			
20. DISTRIBUTION/AVAILABILITY OF ABSTRACT <input type="checkbox"/> UNCLASSIFIED/UNLIMITED <input checked="" type="checkbox"/> SAME AS RPT. <input type="checkbox"/> DTIC USERS		21. ABSTRACT SECURITY CLASSIFICATION UNCLASSIFIED	
22a. NAME OF RESPONSIBLE INDIVIDUAL Betty L. Fox		22b. TELEPHONE (Include Area Code) (202) 325-7042	22c. OFFICE SYMBOL DNA/STTI

UNCLASSIFIED

SECURITY CLASSIFICATION OF THIS PAGE



PREFACE

The author would like to thank Roy P. Basler of SRI International for his cooperation in providing data from the HF Channel Probe experiment and for profitable conversations. I would also like to thank Blair E. Sawyer of MRC for enlightening discussions and for providing the three-dimensional scattering function plotting routines.



Accession For	
NTIS GRA&I	<input checked="" type="checkbox"/>
DTIC TAB	<input type="checkbox"/>
Unannounced	<input type="checkbox"/>
Justification	
By _____	
Distribution/	
Availability Codes	
Dist	Avail and/or Special
A1	

CONVERSION TABLE

Conversion factors for U.S. Customary to metric (SI) units of measurement

MULTIPLY \longleftrightarrow BY \longleftrightarrow TO GET
 TO GET \longleftarrow BY \longleftarrow DIVIDE

angstrom	1.000 000 X E -10	meters (m)
atmosphere (normal)	1.013 25 X E +2	kilo pascal (kPa)
bar	1.000 000 X E + 2	kilo pascal (kPa)
barn	1.000 000 X E -28	meter ² (m ²)
British thermal unit (thermochemical)	1.054 350 X E + 3	joule (J)
calorie (thermochemical)	4.184 000	joule (J)
cal (thermochemical)/cm ²	4.184 000 X E -2	mega joule/m ² (MJ/m ²)
curie	3.700 000 X E +1	*giga becquerel (GBq)
degree Fahrenheit	1.745 329 X E -2	radian (rad)
degree Celsius	t = (t°F + 459.67)/1.8	degree kelvin (K)
electron volt	1.602 19 X E -19	joule (J)
erg	1.000 000 X E -7	joule (J)
erg/second	1.000 000 X E -7	watt (W)
foot	3.048 000 X E -1	meter (m)
foot-pound-force	1.355 818	joule (J)
gallon (U.S. liquid)	3.785 412 X E -3	meter ³ (m ³)
inch	2.540 000 X E -2	meter (m)
jerk	1.000 000 X E +9	joule (J)
joule/kilogram (J/kg)(radiation dose absorbed)	1.000 000	Gray (Gy)
kilotons	4.183	terajoules
kip (1000 lbf)	4.448 222 X E +3	newton (N)
kip/inch ² (ksi)	6.894 757 X E +3	kilo pascal (kPa)
ktap	1.000 000 X E +2	newton-second/m ² (N-s/m ²)
micron	1.000 000 X E -6	meter (m)
mil	2.540 000 X E -5	meter (m)
mile (international)	1.609 344 X E +3	meter (m)
ounce	2.834 952 X E -2	kilogram (kg)
pound-force (lbs avoirdupois)	4.448 222	newton (N)
pound-force inch	1.129 848 X E -1	newton-meter (N·m)
pound-force/foot	1.751 268 X E +2	newton/meter (N/m)
pound-force/foot ²	4.788 026 X E -2	kilo pascal (kPa)
pound-force/inch ² (psi)	6.894 757	kilo pascal (kPa)
pound-mass (lbm avoirdupois)	4.535 924 X E -1	kilogram (kg)
pound-mass-foot ² (moment of inertia)	4.214 011 X E -2	kilogram-meter ² (kg·m ²)
pound-mass/foot ³	1.601 846 X E +1	kilogram/meter ³ (kg/m ³)
rad (radiation dose absorbed)	1.000 000 X E -2	**Gray (Gy)
roentgen	2.579 760 X E -4	coulomb/kilogram (C/kg)
shake	1.000 000 X E -8	second (s)
slug	1.459 390 X E +1	kilogram (kg)
torr (mm Hg, 0° C)	1.333 220 X E -1	kilo pascal (kPa)

*The becquerel (Bq) is the SI unit of radioactivity; 1 Bq = 1 event/s.

**The Gray (Gy) is the SI unit of absorbed radiation.

TABLE OF CONTENTS

Section		Page
	PREFACE	iii
	CONVERSION TABLE	iv
	LIST OF ILLUSTRATIONS	vi
	LIST OF TABLES	ix
1	INTRODUCTION	1
2	IONOGRAM SCALING	5
	2.1 INTRODUCTION	5
	2.2 PROPERTIES OF VERTICAL AND OBLIQUE IONOGRAMS	5
	2.3 METHODS OF SCALING OBLIQUE IONOGRAMS	11
	2.4 FITTING THE OBLIQUE IONOGRAM TO A QUASI-PARABOLIC LAYER	15
	2.5 HANDLING ABSOLUTE DELAY UNCERTAINTIES	23
3	STOCHASTIC SIGNAL STRUCTURE PARAMETERS	35
	3.1 INTRODUCTION	35
	3.2 THE SCATTERING FUNCTION	36
	3.3 THE DNA SCINTILLATION MODEL	42
	3.4 PARAMETER DEPENDENCE	47
4	TESTS OF THE SCINTILLATION MODEL	60
	4.1 INTRODUCTION	60
	4.2 THE DATA	60
	4.3 INITIAL FITS	74
	4.4 FITTING ASSOCIATED MODES	76
5	CONCLUSIONS	80
6	LIST OF REFERENCES	84

LIST OF ILLUSTRATIONS

Figure		Page
1	Synthesized vertical incidence ionogram (solid line) and corresponding electron density profile (dotted line).	8
2	Synthesized oblique ionogram for the Narssarssuaq to Thule link (ground range $D = 1918$ km) corresponding to the electron density profile of Figure 1.	9
3	High and low ray paths for 10 MHz rays over the Narssarssuaq to Thule link ($D = 1918$ km, 500 km between tick marks).	12
4	Comparison of oblique to vertical ionogram conversion using geometry only (dotted curve) with the true vertical incidence ionogram (solid curve).	14
5	Ground range as a function of launch elevation plotted parametrically with carrier frequency for a quasi-parabolic layer with parameters $f_c = 4.5$ MHz, $h_m = 300$ km, $y_m = 50$ km.	19
6	Oblique ionogram dependence on quasi-parabolic layer parameters.	21
7	Example of an HF Channel Probe oblique ionogram measurement.	22
8	Result of a nonlinear regression fit to a quasi-parabolic layer for the ionogram of Figure 7.	24
9	Comparison of ionogram fits for no delay shift $\Delta\tau = 0$ (a) and $\Delta\tau$ fitted (b). Day 277 17:31 GMT.	26
10	Comparison of ionogram fits for no delay shift $\Delta\tau = 0$ (a) and $\Delta\tau$ fitted (b). Day 277 17:46 GMT.	29
11	Comparison of ionogram fits for no delay shift $\Delta\tau = 0$ (a) and $\Delta\tau$ fitted (b). Day 79 18:01 GMT.	30
12	Comparison of ionogram fits for no delay shift $\Delta\tau = 0$ (a) and $\Delta\tau$ fitted (b). Day 79 18:01 GMT.	31

LIST OF ILLUSTRATIONS (continued)

Figure		Page
13	Comparison of ionogram fits for no delay shift $\Delta\tau = 0$ (a) and $\Delta\tau$ fitted (b). Day 79 18:16 GMT.	32
14	Comparison of ionogram fits for no delay shift $\Delta\tau = 0$ (a) and $\Delta\tau$ fitted (b). Day 79 18:31 GMT.	33
15	Example of an HF Channel Probe scattering function measurement corresponding to the ionogram of Figure 10.	41
16	Delay and doppler spread variation with spectral index for the low ray of Figure 3.	49
17	Delay and doppler spread variation with spectral index for the high ray of Figure 3.	50
18	Delay and doppler spread variation with L_{\perp} for the low ray of Figure 3.	51
19	Delay and doppler spread variation with L_{\perp} for the high ray of Figure 3.	52
20	Delay and doppler spread variation with L_{\parallel} for the low ray of Figure 3.	53
21	Delay and doppler spread variation with L_{\parallel} for the high ray of Figure 3.	54
22	Delay and doppler spread variation with ϵ for the low ray of Figure 3.	55
23	Delay and doppler spread variation with ϵ for the high ray of Figure 3.	56
24	Delay and doppler spread variation with ξ for the low ray of Figure 3.	57
25	Delay and doppler spread variation with ξ for the high ray of Figure 3.	58
26	HF Channel Probe scattering function measurement, Oct. 3, 1984, 13:47 GMT (a) and corresponding oblique ionogram (b) including best fit parameters for a quasi-parabolic layer.	62

LIST OF ILLUSTRATIONS (continued)

Figure		Page
27	Fit to two bivariate gaussians of the scattering function measurement of Figure 26.	63
28	HF Channel Probe scattering function measurement, Oct. 3, 1984, 15:18 GMT (a) and corresponding oblique ionogram (b) including best fit parameters for a quasi-parabolic layer.	64
29	Fit to two bivariate gaussians of the scattering function measurement of Figure 28.	65
30	HF Channel Probe scattering function measurement, Oct. 3, 1984, 17:47 GMT (a) and corresponding oblique ionogram (b) including best fit parameters for a quasi-parabolic layer.	66
31	Fit to two bivariate gaussians of the scattering function measurement of Figure 30.	67
32	HF Channel Probe scattering function measurement, Mar. 20, 1985, 14:32 GMT (a) and corresponding oblique ionogram (b) including best fit parameters for a quasi-parabolic layer.	68
33	Fit to two bivariate gaussians of the scattering function measurement of Figure 32.	69
34	HF Channel Probe scattering function measurement, Mar. 20, 1985, 18:19 GMT (a) and corresponding oblique ionogram (b) including best fit parameters for a quasi-parabolic layer.	70
35	Fit to two bivariate gaussians of the scattering function measurement of Figure 34.	71
36	HF Channel Probe scattering function measurement, Mar. 20, 1985, 18:32 GMT (a) and corresponding oblique ionogram (b) including best fit parameters for a quasi-parabolic layer.	72
37	Fit to two bivariate gaussians of the scattering function measurement of Figure 36.	73
38	Doppler spread discrepancy versus delay spread discrepancy for the high ray when fit parameters for the low ray are used (circles).	75

LIST OF TABLES

Table		Page
1	Quasi-parabolic fits for forced absolute delay shifts $\Delta\tau$ of the measured data.	25
2	Comparison of ionogram fits for $\Delta\tau = 0$ and $\Delta\tau$ varied.	28
3	Bivariate gaussian fit parameters for the scattering function of Figure 26, Day 277, 13:47 GMT.	63
4	Bivariate gaussian fit parameters for the scattering function of Figure 28, Day 277, 15:18 GMT.	65
5	Bivariate gaussian fit parameters for the scattering function of Figure 30, Day 277, 17:47 GMT.	67
6	Bivariate gaussian fit parameters for the scattering function of Figure 32, Day 79, 14:32 GMT.	69
7	Bivariate gaussian fit parameters for the scattering function of Figure 34, Day 79, 18:19 GMT.	71
8	Bivariate gaussian fit parameters for the scattering function of Figure 36, Day 79, 18:32 GMT.	73
9	Result of adjusting the spectral index and plasma velocity parameters to fit the low ray modes exactly and subsequent application of these parameters to the high ray modes.	75
10	Results of a four parameter simultaneous fit of the low and high ray modes.	78

SECTION 1 INTRODUCTION

In recent years a formulation for the calculation of stochastic effects on electromagnetic waves due to structured ionization has been developed under the sponsorship of the Defense Nuclear Agency (DNA) [Rino, 1982; Wittwer, 1979, 1982] for trans-ionospheric links at radio frequencies. In this regime, the frequency of the wave is always substantially above the plasma frequency of the ionosphere so that the wave propagates essentially along the line of sight path. Approximations which make use of the large carrier to plasma frequency ratio are valid, and it is possible to obtain accurate expressions for such stochastic quantities as the coherence bandwidth and coherence time (or their Fourier conjugates, delay width and doppler spread) in terms of a fairly small number of physical parameters.

At high frequencies (HF) the situation is more complicated. In this case one is interested in signals which are reflected from the ionization. This complicates the problem in that the path followed by the wave is no longer a straight line, but is instead curved as the wave progresses through regions of changing electron density. This bending of the path may be more or less severe depending on, for instance, the launch elevation angle of the wave or the steepness of the electron density gradients encountered by the wave. Since the wave is reflected, there may be some region in which the plasma frequency approaches the carrier frequency. The high frequency approximations which allowed a tractable theory in the trans-ionospheric case may thus become invalid over some region along the path. For highly oblique paths in stratified ionization, however, the

wave carrier frequency remains substantially above the plasma frequency even at the reflection point, and the high frequency approximations may still be valid.

We wish to explore the extent to which the trans-ionospheric theory can be applied to such internally reflected paths at HF. This means determining whether the theory, which we will refer to as the DNA scintillation model, is capable of predicting the appropriate level of scintillations for a physically reasonable set of parameters. Data is now available to make such a test.

Measurements of signal strength as a function of frequency and delay were made under the sponsorship of DNA by SRI International in an experiment called the HF Channel Probe. The measurements we will consider were made over a one hop path in the polar region. The link, located in Greenland, consisted of a transmitter at Narssarssuaq and two receivers at Thule, 1918 km to the north. Details on the experimental setup and measurements are contained in Basler et al., [1985]. Their measurements yield information on the degree of spreading in delay and doppler frequency suffered by signals at HF due to naturally occurring ionization structure in the polar region. These delay spreads and doppler spreads can be compared to the predictions of the DNA scintillation model for various values of the model parameters as a test of the applicability of the formulation at HF. To confirm the model would require independent measurements of the model parameters taken simultaneously with the measurements of delay spread and doppler spread. Since this data does not exist, we will not be able to completely validate the model, but enough is known about the model parameters that any gross failure of the model should be apparent.

The DNA scintillation model is based on integrations taken along the mean ray path of quantities involving the electron concentration.

Thus one must know the electron density profile along the path followed by the ray. In conjunction with their measurements, the HF Channel Probe experimentalists made oblique soundings over the link. From these oblique ionograms the required electron density profiles may be inferred. After first reviewing the nature of oblique ionograms and previous methods for determining electron density profiles from them (ionogram scaling), we present in Section 2 our procedure for fitting these ionograms using a particular functional form for the ionosphere, the quasi-parabolic layer.

Given the ionospheric profile, ray trajectories over the link can be numerically constructed and the scintillation model calculations performed. We have incorporated the DNA scintillation model calculations into the Jones-Stephenson ray tracing code for this purpose [Jones and Stephenson, 1975]. In Section 3 we will briefly discuss the relevant parts of the DNA scintillation model and explore the model dependence on its parameters. From this we will gain insight into the relative sensitivity of the model parameters, and this information will be used to guide us to an appropriate starting point for testing the model against the HF Channel Probe measurements. In particular, we will find that the model is substantially more sensitive to one of the parameters, the spectral index, than to the others (although two other model parameters will be found to be sufficiently sensitive to be important).

In Section 4 we will present our analysis of the HF Channel Probe data and test the DNA scintillation model. After first selecting several data sets which span a variety of propagation conditions, we will extract delay and doppler spreads from the measurements. The results of the parameter sensitivity investigation performed in Section 3 will motivate an initial test of the model in which the spectral index is chosen as the primary adjustable parameter. The result of this initial test will lead to speculation about which of the remaining parameters should be made variable. A quite successful four parameter fit to the data will finally be performed.

The results of our analysis will be summarized in Section 5. We will conclude that the DNA scintillation model is capable of describing the appropriate level of stochastic effects observed on highly oblique internal paths at HF for reasonable values of the model parameters. This conclusion is based on our result that good fits to the HF Channel Probe data are obtained for model parameters that are consistent with expected values of these parameters, and in some cases with independent (although not simultaneous) measurements of these parameters.

SECTION 2 IONOGRAM SCALING

2.1 INTRODUCTION.

The DNA scintillation model for the calculation of stochastic signal structure parameters requires that integrations be taken along the mean ray path of quantities which involve the local electron density. For this reason we need to know the electron density profile along the path followed by the ray. This information may be gleaned to some degree of approximation from the oblique ionograms taken by the HF Channel Probe.

The process of determining electron density profiles from ionospheric soundings is known as ionogram scaling. In this section we will describe vertical and oblique ionograms and explain their appearance. Methods of scaling oblique ionograms will be briefly discussed followed by a presentation of our approach to this problem. Finally, we will discuss a method for handling absolute delay uncertainties associated with the HF Channel Probe oblique soundings.

2.2 PROPERTIES OF VERTICAL AND OBLIQUE IONOGRAMS.

An electromagnetic wave at a single frequency propagates at the phase velocity $v_\phi = c/\mu$ where c is the speed of light in vacuum and μ is the index of refraction of the medium. Ignoring collisions and any external magnetic fields, the index of refraction of the ionosphere is real and is given by $\mu = (1 - f_p^2/f^2)^{1/2}$. Here f is the frequency of the wave and f_p is the plasma frequency, $f_p^2 = (c^2 r_e / \pi) N_e$, where r_e is the classical

electron radius $r_e = 2.82 \times 10^{-15}$ m, and N_e is the electron number density. A wave at a single frequency carries no information, and in general signals must be built up as a superposition of waves at a number of frequencies. While each frequency component of the signal propagates at its phase velocity, the signal itself will propagate at the group velocity $v_g = d\omega/dk$ ($\omega=2\pi f$, $k=2\pi/\lambda$ where λ is the wavelength of the frequency component). We will be primarily concerned with signals which have a predominant frequency component known as the carrier frequency. When no external magnetic fields are present, the group velocity in this case is $v_g = c\mu$, with μ evaluated at the carrier frequency.

An ionospheric sounding is a measurement of the time of travel from transmitter to receiver of a signal at a given carrier frequency. This transit time, or delay, is given by

$$\tau = \int \frac{ds}{v_g} = \frac{1}{c} \int ds \left[1 - \frac{f_p^2}{f^2} \right]^{-1/2}, \quad (1)$$

where the integral is over the path followed by the signal (the ray path). An ionogram is a plot of these delays as a function of carrier frequency. In the case that the waves are propagated vertically into the ionosphere and return to the transmitter location, it is convenient to define the virtual height, $h' = c\tau/2$. The virtual height is the height implied by the measured delay if the signal had propagated at the speed of light, and is larger than the true height h_t of the signal reflection point.

Consider a signal propagated vertically from the earth incident upon a single ionospheric layer with a unique maximum in electron density. As a signal propagates into the layer, the local plasma frequency grows as the local electron density gets larger, causing the index of refraction to get smaller. The group velocity is reduced and the delay is correspondingly increased. The wave is reflected at the point where the

electron density is such that the plasma frequency equals the carrier frequency of the signal. If the carrier frequency is larger than the plasma frequency of the layer maximum, the wave will penetrate the layer.

A synthesized vertical incidence ionogram is shown in Figure 1 (solid curve) as a plot of virtual height as a function of carrier frequency. The electron density profile used is also shown (dotted curve) plotted as a function of plasma frequency. The true height of reflection at a given carrier frequency is the height of the equivalent plasma frequency on the bottom side of the layer. One can see that the difference between virtual height and true height becomes arbitrarily large near the layer maximum.

In the case of a monotonic electron density profile, Eq. (1) can be inverted to yield the electron density profile, given the virtual height of reflection [Budden, sec. 10.12],

$$h_t(f_p) = \left(\frac{2}{\pi}\right) \int_0^{\pi/2} h'(f_p \sin \alpha) d\alpha \quad . \quad (2)$$

For more complicated profiles or multiple layers, the inversion of Eq. (1) can only be done approximately. In these cases it may be more convenient to assume some functional form for the electron density profile and to adjust the parameters of that function until the measured virtual heights are obtained. Procedures for scaling vertical ionograms are discussed in a special issue of Radio Science (Vol. 2, No. 10, October 1967).

We now turn to the case of oblique propagation, in particular to the bistatic configuration where the receiver is at some distance D (ground range) from the transmitter. Figure 2 shows a synthesized ionogram corresponding to the vertical ionogram of Figure 1 for the

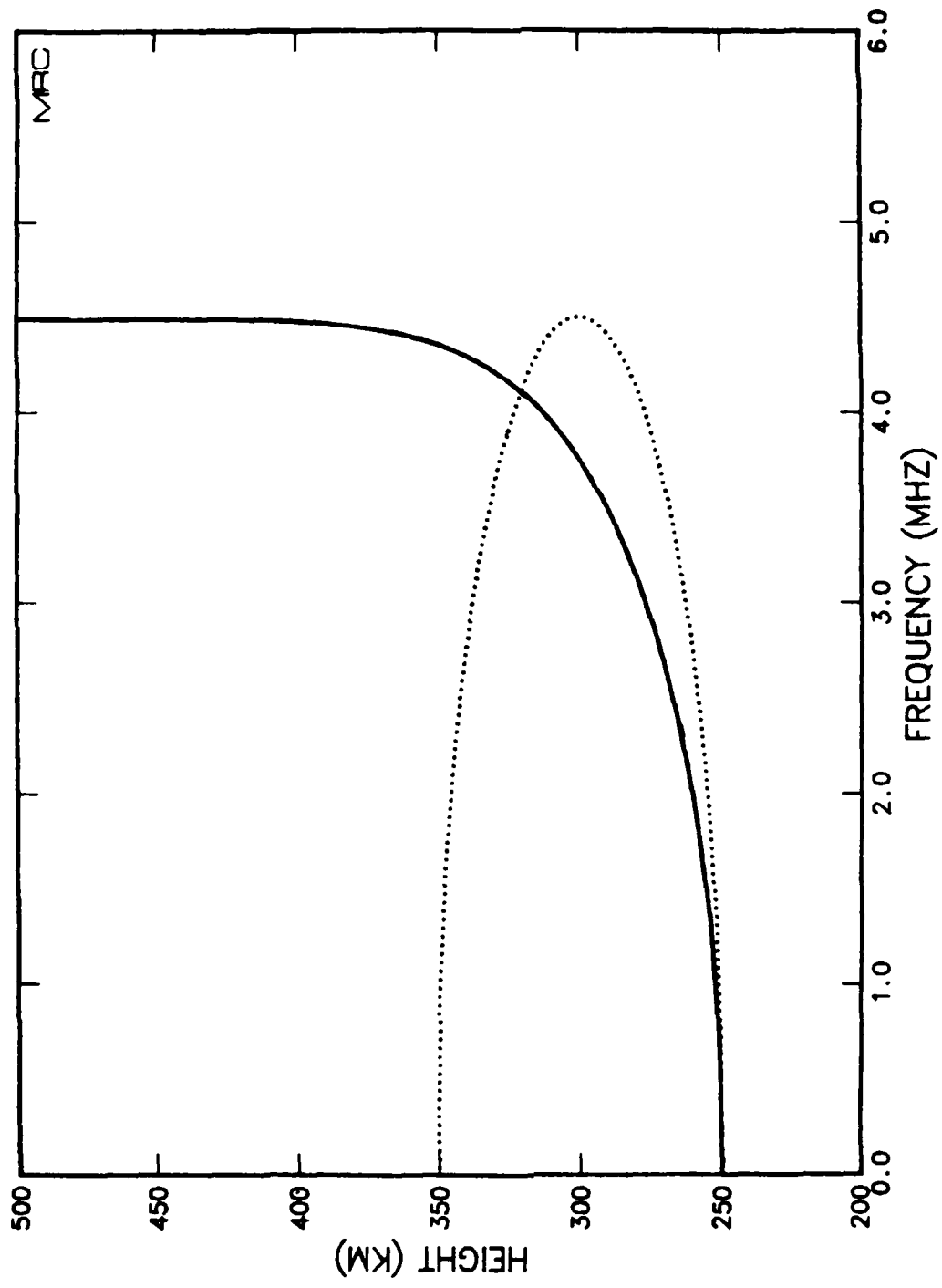


Figure 1. Synthesized vertical incidence ionogram (solid line) and corresponding electron density profile (dotted line).

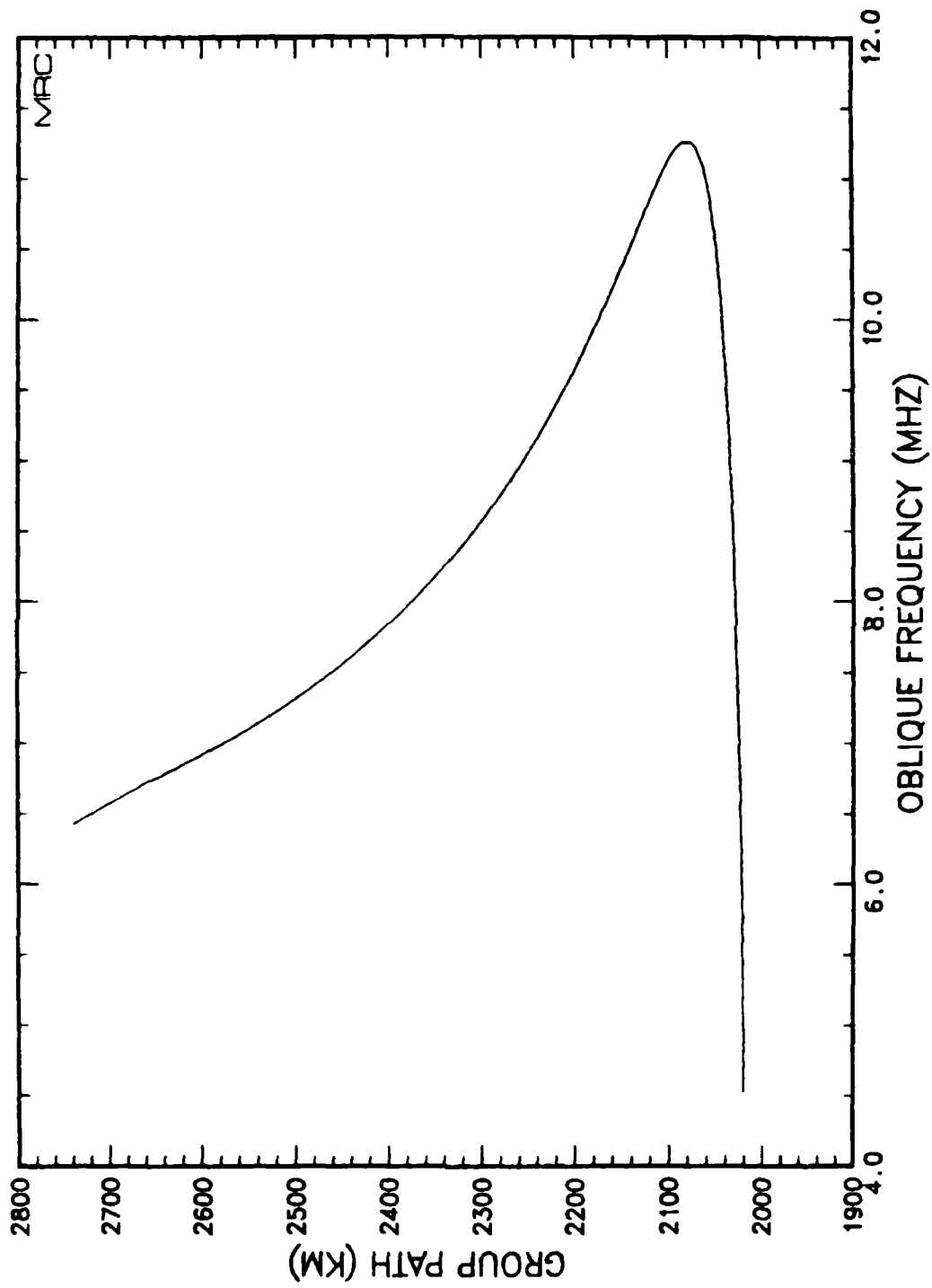


Figure 2. Synthesized oblique ionogram for the Narsarsuaq to Thule link (ground range D = 1918 km) corresponding to the electron density profile of Figure 1.

Narssarssuaq to Thule link of the HF Channel Probe measurements ($D = 1918$ km). The group path is defined as $P' = c\tau$ where τ is the total time delay for signal propagation from transmitter to receiver. The horizontal axis is the signal carrier frequency and has been labeled oblique frequency to distinguish it from the carrier frequency of the equivalent vertical ionogram.

There is a one-to-one mapping of vertical ionograms to oblique ionograms. In the simplest case of a flat earth and plane stratified ionosphere, three theorems suffice to define this mapping [Davies, sec. 4.2]. The first is a direct consequence of Snell's Law and is known as the Secant Law,

$$f_{ob} = f_v \sec \phi \quad . \quad (3)$$

Here ϕ is the complement of the launch elevation angle. This law states that if f_v is the carrier frequency of a signal reflected at some true height for vertical incidence, then a higher frequency f_{ob} will be reflected at that same true height for oblique incidence. The second is Breit and Tuve's Theorem, which states that the group path P' for ground-sky-ground transmission is equal to the length of the triangular path defined by the launch and arrival elevation angles (with the ground range D as the base of the triangle). The third is Martyn's Equivalent Path Theorem which states that the height of this triangle is equal to the virtual height h' of a vertically incident signal at the equivalent vertical frequency f_v given by the Secant Law. These relationships yield the mapping,

$$f_v = f_{ob} \left[1 - \left(\frac{D}{P'} \right)^2 \right]^{1/2} \quad (4a)$$

plane earth and
ionosphere .

$$h' = \left(\frac{1}{2} \right) [P'^2 - D^2]^{1/2} \quad (4b)$$

These expressions must be modified for a spherical earth and ionosphere (which is the case for Fig. 2), but Eq's (4) suffice to explain the gross features of oblique ionograms.

The most noticeable feature in comparing the oblique ionogram of Figure 2 with its vertical incidence counterpart, Figure 1, is that over a large frequency range there are two received signals for a given carrier frequency. This is a general property of single layers with a unique maximum electron density. The signal with the longer delay is called the high ray, the other the low ray. These rays coalesce at a frequency called the junction frequency. Figure 3 shows the ray paths for the high and low rays at 10 MHz. The ionospheric layer is also shown, with the dashed line at the layer maximum. The high ray is seen to ride the crest of the layer. A slight increase in launch elevation angle would cause that ray to penetrate the ionosphere.

2.3 METHODS OF SCALING OBLIQUE IONOGRAMS.

Methods for scaling oblique ionograms fall basically into two categories, those which involve transforming the oblique ionogram to its vertical incidence equivalent and scaling that, and those which scale directly from the oblique trace. Each of these categories can be further subdivided as to whether a true height analysis is performed (e.g. Eq. (2)) or whether some functional form is used in a fit of the ionosphere.

The transformation of an oblique ionogram to its vertical incidence equivalent for a spherical earth and spherically stratified ionosphere unfortunately depends not only on geometrical considerations, but also on the actual refraction experienced by the ray, hence on the electron density profile itself. One may ignore these refractive effects and carry out the transformation using geometrical considerations only by modifying Eq. (4b) to its spherical geometry counterpart (R is the

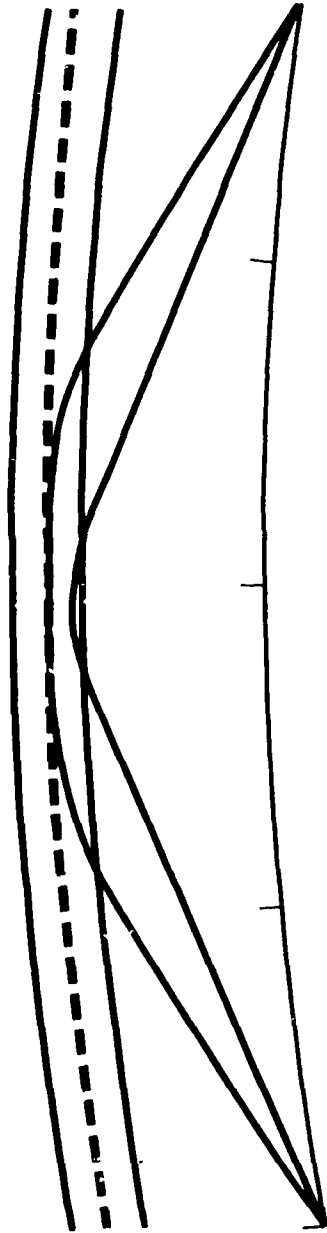


Figure 3. High and low ray paths for 10 MHz rays over the Narssarsuaq to Thule link ($D = 1918$ km, 500 km between tick marks). The ionospheric layer is that of Figure 1 and is shown with solid curves at its boundaries and a dashed curve at the layer maximum.

radius of the earth),

$$\left(\frac{P'}{2}\right)^2 = 2R(R+h') \left[1 - \cos\left(\frac{D}{2R}\right)\right] + h'^2 \quad . \quad (5)$$

Figure 4 compares the vertical ionogram of Figure 1 with the result of transforming the oblique ionogram of Figure 2 using Eq. (5) and Eq. (3) with ϕ taken as the apex half angle of the triangular path,

$$\sin \phi = \left(\frac{2R}{P'}\right) \sin \left(\frac{D}{2R}\right) \quad . \quad (6)$$

There is a significant discrepancy in the transformed ionogram as one approaches the critical frequency of the layer. Refractive effects can be approximately taken into account by modifying Eq. (4a) to [Smith, (1939)],

$$f_{ob} = f_v \kappa \sec \phi \quad , \quad (7)$$

where the correction factor κ is largely due to the difference in angle of incidence between different ionospheric heights but is also a function of the electron density profile. The factor κ typically ranges from 1 to about 1.2 . Analytic expressions for κ can be obtained for specific functional forms for the electron density profile [Basler and Scott, (1973)]. The two curves of Figure 4 can be brought into substantial agreement with a correction factor of about $\kappa=1.06$. Thus it is possible to transform an oblique ionogram to an equivalent vertical incidence ionogram to a fair degree of accuracy. Once this is done one may apply a true height analysis or some fitting procedure to infer an associated electron density profile.

As we remarked above, it is also possible to carry out a true height analysis directly from the oblique trace [Reilly, (1985)]. This

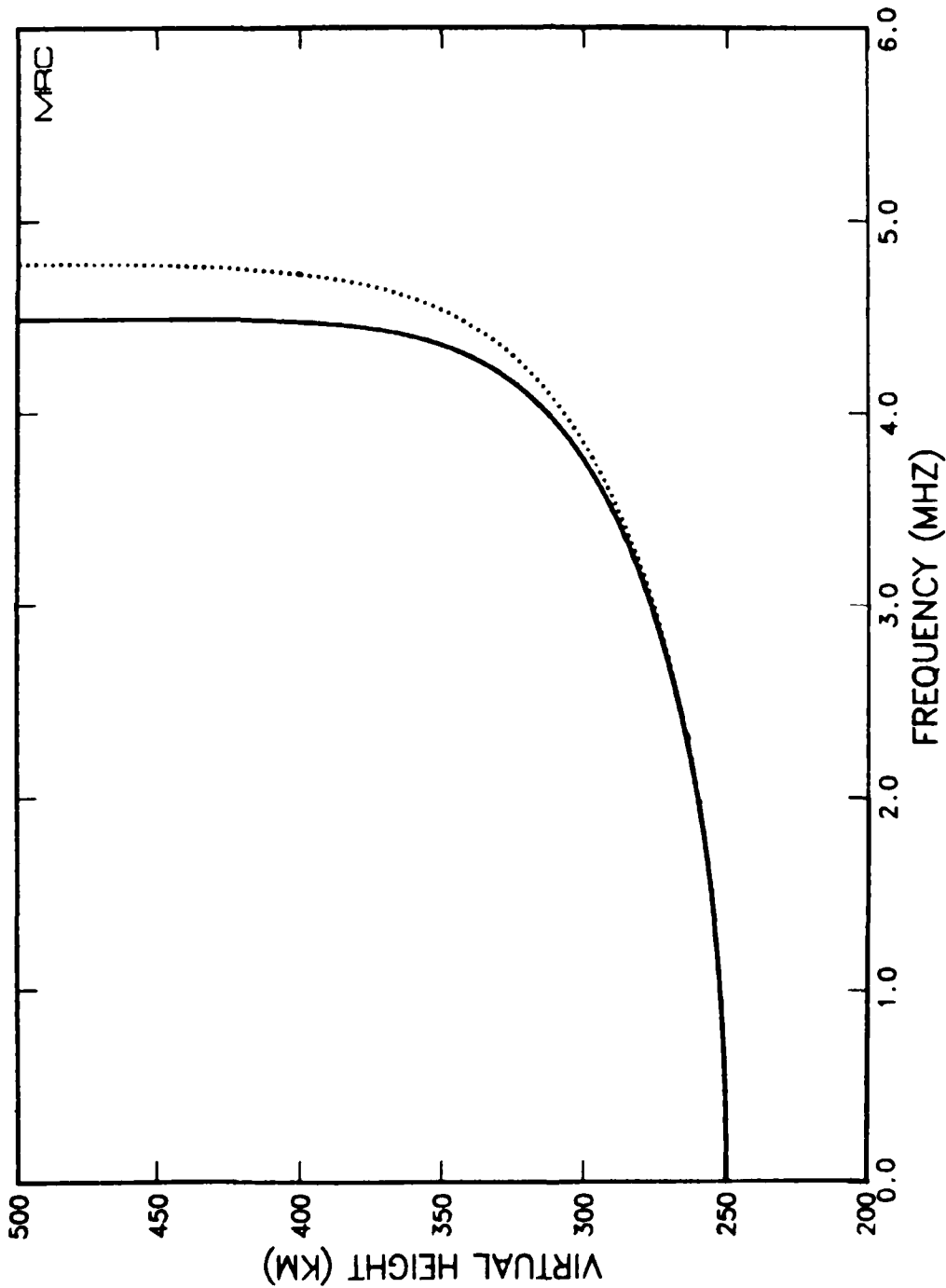


Figure 4. Comparison of oblique to vertical ionogram conversion using geometry only (dotted curve) with the true vertical incidence ionogram (solid curve).

procedure basically involves numerically inverting an expression for oblique paths analogous to Eq. (1), building up the profile from the bottom. To perform such a true height analysis, whether directly from the oblique trace or from the equivalent vertical trace, requires that the delays are known fairly precisely. Ionograms often exhibit substantial spreading in delay, so some method of obtaining an appropriate value for delay at each frequency (i.e., fitting) must be administered.

We have found that the most convenient method for scaling the HF Channel Probe soundings is to parameterize the ionosphere and apply a fitting procedure directly to the oblique ionogram data. Because of the large spread in delay typically observed in these measurements, fitting must necessarily be done at some stage in the analysis anyway. By choosing a convenient functional form for the ionospheric profile and adjusting the parameters to obtain a best fit to the measured oblique ionogram, we avoid the approximate and unnecessary step of transforming to equivalent vertical incidence.

2.4 FITTING THE OBLIQUE IONOGRAM TO A QUASI-PARABOLIC LAYER.

The ionosphere typically exhibits two layers which are more or less distinct. The lower layer, or E-layer, has its maximum electron density at a height of about 110 km. The maximum electron density of the higher F-layer is generally much larger than that of the E-layer and resides in the range of 200 to 400 km. During daylight hours the F-layer sometimes shows a smaller enhancement below the maximum electron density, known as the F_1 -layer. In this case the main maximum is denoted the F_2 -layer. To properly fit the ionosphere then, two or three parametric layers should be used. We will be concerned with HF Channel Probe scattering function measurements associated with reflection from the F-layer. These measurements were usually made at carrier frequencies reasonably close to the junction frequency for the F-layer, and in this region the signals are

only minimally affected by any underlying E-layer ionization. Furthermore, any splitting of the F-layer is sufficiently indistinct in this data so as to warrant only a single layer fit. Thus for the purpose of reproducing an ionosphere for analyzing the scattering function measurements, it is adequate to fit the oblique ionogram data to a single layer accurate in the nose region of the trace.

Fitting the oblique ionogram data requires repetitive calculation of ray paths and the corresponding delays (or group paths). For this reason it is convenient to choose a functional form for the layer for which analytic expressions for group path and ground range exist. The quasi-parabolic layer [Croft and Hoogasian, (1968)] provides such expressions for a spherical earth and spherically stratified ionosphere. Written in terms of plasma frequency, the functional form of the layer is

$$f_p^2 = \begin{cases} f_c^2 \left\{ 1 - \left[\frac{r-r_m}{y_m} \right]^2 \left(\frac{r_b}{r} \right)^2 \right\} & , \quad r_b < r < r_m \left[\frac{r_b}{r_b - y_m} \right] \\ 0 & , \quad \text{elsewhere} \end{cases} \quad (8)$$

where r is the distance from the center of the earth and the parameters are

$$\begin{aligned} f_c &= \text{critical frequency of the layer} \\ r_m &= \text{earth centered radius of the maximum} \\ y_m &= \text{semi-thickness of the layer} \end{aligned} \quad (9)$$

and $r_b = r_m - y_m$. We introduce the substitutions

$$A = 1 - \left(\frac{f_c}{f} \right)^2 + \left(\frac{f_c r_b}{f y_m} \right)^2 \quad (10a)$$

$$B = -2r_m \left(\frac{f_c r_b}{f y_m} \right)^2 \quad (10b)$$

$$C = \left(\frac{f_c r_b}{f y_m} \right)^2 - r_0^2 \cos^2 \beta_0 \quad (10c)$$

$$\cos \gamma = \left(\frac{r_0}{r_b} \right) \cos \beta_0 \quad (10d)$$

where r_0 is the radius of the earth, β_0 is the launch elevation angle, and γ is the corresponding angle at the bottom of the ionosphere. The expression for ground range is then

$$D = 2r_0(\gamma - \beta_0) - \frac{(r_0^2 \cos \beta_0)}{\sqrt{C}} \ln \left\{ \frac{[B^2 - 4AC]}{4C \left[\sin \gamma + \frac{\sqrt{C}}{r_b} + \frac{B}{(2\sqrt{C})} \right]^2} \right\} \quad (11)$$

and the group path is given by

$$P' = 2r_b \sin \gamma - 2r_0 \sin \beta_0 + \frac{2}{A} \left\{ -r_b \sin \gamma - \frac{B}{4\sqrt{A}} \ln \frac{B^2 - 4AC}{[2Ar_b + B + 2r_b \sqrt{A} \sin \gamma]^2} \right\}. \quad (12)$$

For a given carrier frequency and set of layer parameters it is possible, using Eq. (11), to find the launch elevation angles corresponding to the high and low rays which give a desired ground range D . Once these angles are known, Eq. (12) yields the corresponding delays. Eq. (11) is transcendental in β_0 , so it is necessary to apply a searching method to find these launch elevation angles for fixed ground range. It is therefore important to know the largest launch elevation angle β_{\max} for a given carrier frequency beyond which rays will penetrate the layer. This angle can be obtained by solving the equation for ray apogee height,

$$Ar_t^2 + Br_t + C = 0 \quad , \quad (13)$$

for β_0 using the expression for the maximum apogee height,

$$r_{t,\max} = \frac{-B}{2A} \quad . \quad (14)$$

One approach for obtaining a synthesized oblique ionogram from a quasi-parabolic layer of given layer parameters is to first find the junction frequency f_J and the corresponding launch elevation angle β_J . High and low ray values at lower frequencies can then be searched for at respectively higher and lower launch elevations, bounded by β_{\max} above and zero below. Figure 5 shows a plot of ground range as a function of launch elevation angle for a quasi-parabolic layer, plotted parametrically with carrier frequency. The layer parameters in this case are $f_c = 4.5$ MHz, $h_m = 300$ km, $y_m = 50$ km (h_m is the height of the layer maximum above the earth's surface, $h_m = r_m - r_0$, with $r_0 = 6359$ km, the approximate value of the earth's radius at Greenland). For a fixed ground range D_0 (e.g. 1918 km for the Narssarssuaq to Thule link) there will be one curve whose minimum value is at precisely that ground range. The corresponding frequency and elevation are the desired f_J and β_J . Writing

$$F(f, \beta) = D(f, \beta) - D_0 \quad (15a)$$

$$G(f, \beta) = \partial D / \partial \beta \Big|_f \quad , \quad (15b)$$

the conditions for obtaining f_J and β_J are

$$F(f_J, \beta_J) = 0 = G(f_J, \beta_J) \quad . \quad (16)$$

Newton's method applied to two functions of two variables provides a convenient way of numerically solving this problem, that is, solving iteratively the set of equations,

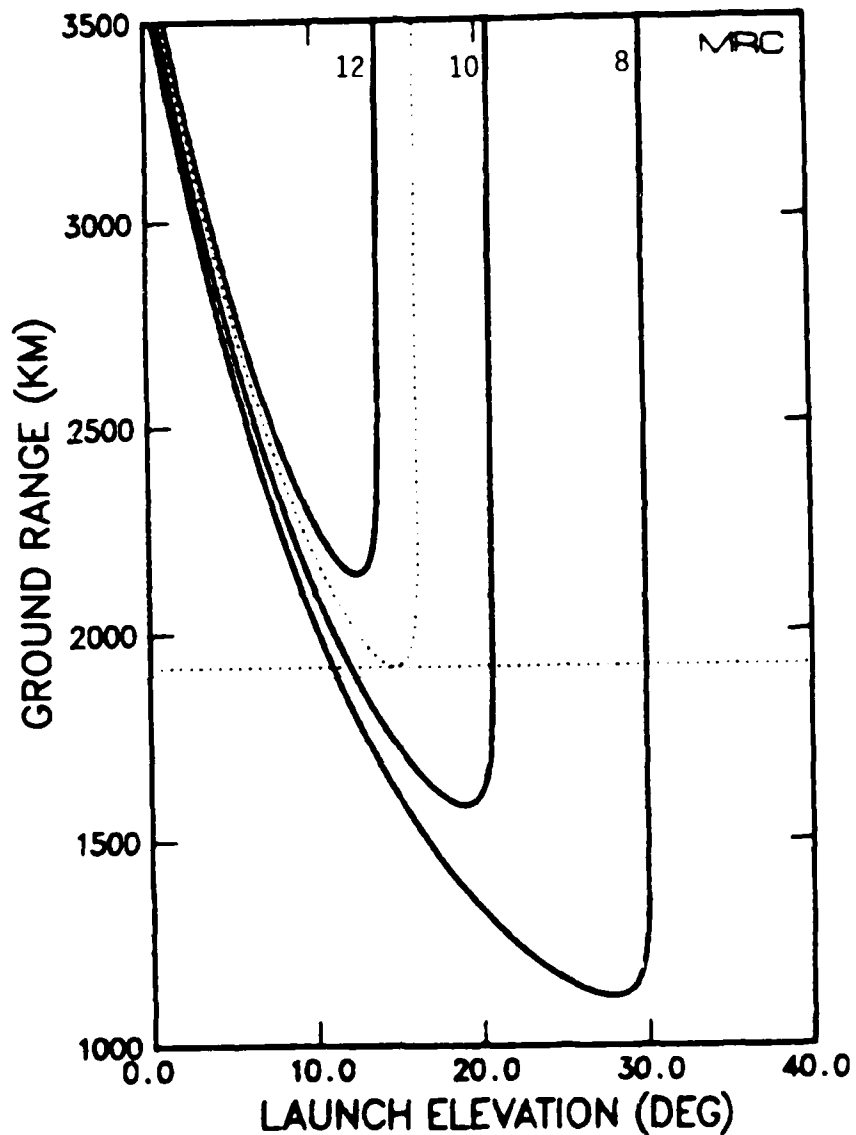


Figure 5. Ground range as a function of launch elevation plotted parametrically with carrier frequency for a quasi-parabolic layer with parameters $f_c = 4.5$ MHz, $h_m = 300$ km, $y_m = 50$ km. The horizontal dotted line is at $D = 1918$ km and just touches the curve $f_j = 11.263$ MHz at $\beta_j = 14.83$ deg.

$$f^{\text{new}} = f^{\text{old}} + \frac{[F_{\beta}G - F G_{\beta}]}{[F_f G_{\beta} - F_{\beta} G_f]} l_{\text{old}} \quad (17a)$$

$$\beta^{\text{new}} = \beta^{\text{old}} + \frac{[F G_f - F_f G]}{[F_f G_{\beta} - F_{\beta} G_f]} l_{\text{old}} \quad (17b)$$

where the subscripts refer to partial differentiation.

Having found the junction values, a search can be made at lower frequencies for the launch angles of the high and low rays by stepping away from β_j , cutting the step size down each time the calculated ground range exceeds D_0 , until a desired accuracy in D_0 is obtained. Eq. (12) then yields the group path for these frequencies and angles. Figure 6 shows synthesized oblique ionograms for quasi-parabolic layers, showing the variation of the trace as each of the layer parameters are increased from the base values $f_c = 4.5$ MHz, $h_m = 300$ km, $y_m = 50$ km (solid curve).

The HF Channel Probe oblique ionogram data taken by SRI International consist of power measurements at 128 delays for each of 576 carrier frequencies. One such measurement is displayed in Figure 7. This sounding was made on March 20, 1985 (day 79 refers to the day number of year 1985) at 18:31 GMT, corresponding to a local time of approximately 16:00. Only data within about 10 dB of the peak measured power is shown. A fairly well defined F-layer is apparent as well as some evidence for an underlying E-layer. The data in the upper left corner of the plot is the two hop echo of the F-layer. The F-layer trace exhibits a slight nose extension. This is a scatter effect frequently observed in high latitudes.

We fit the measured ionogram data to a quasi-parabolic layer utilizing a nonlinear regression fitting routine. This routine synthesizes an oblique ionogram corresponding to a set of starting layer param-

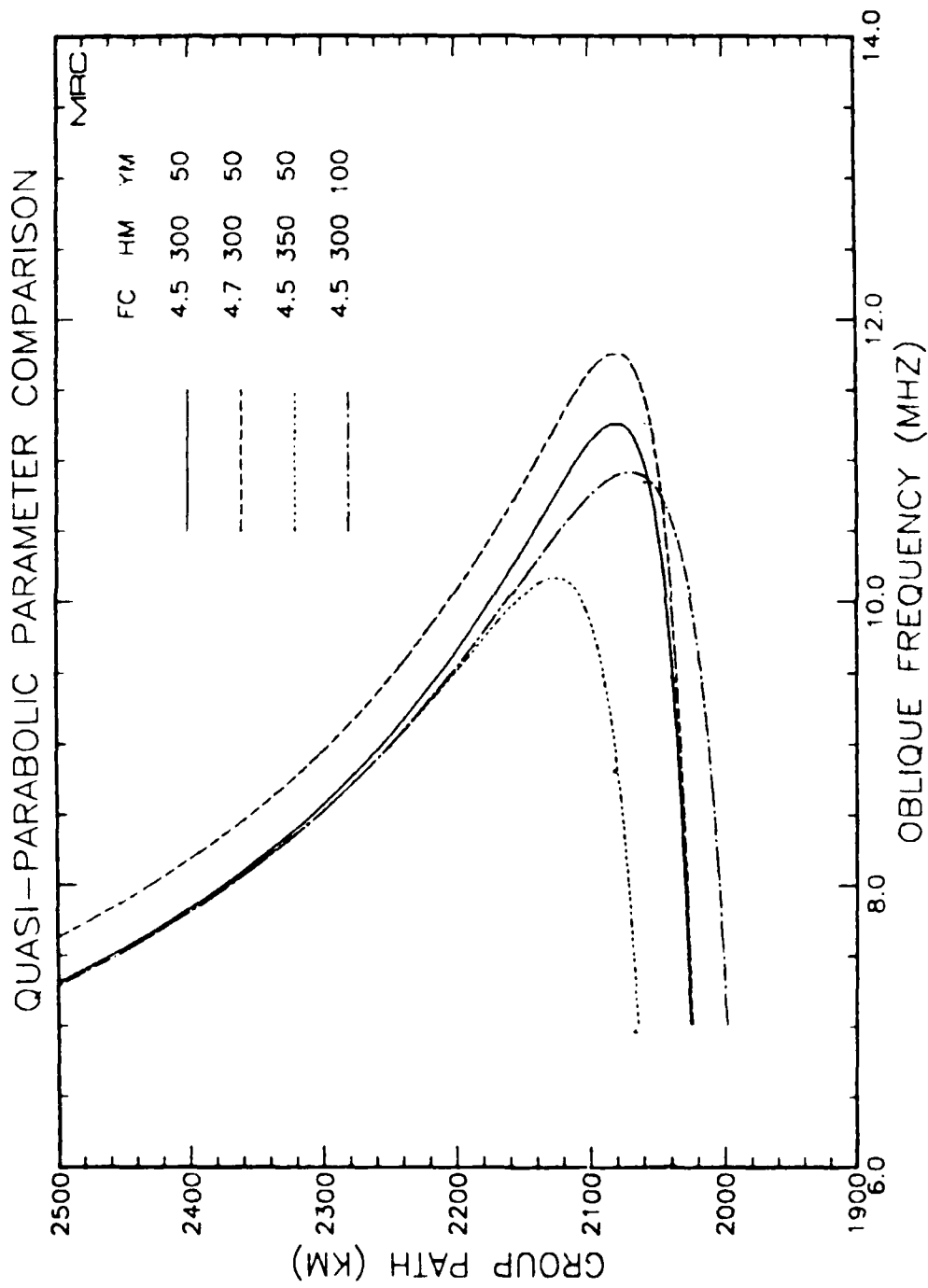


Figure 6. Oblique ionogram dependence on quasi-parabolic layer parameters.

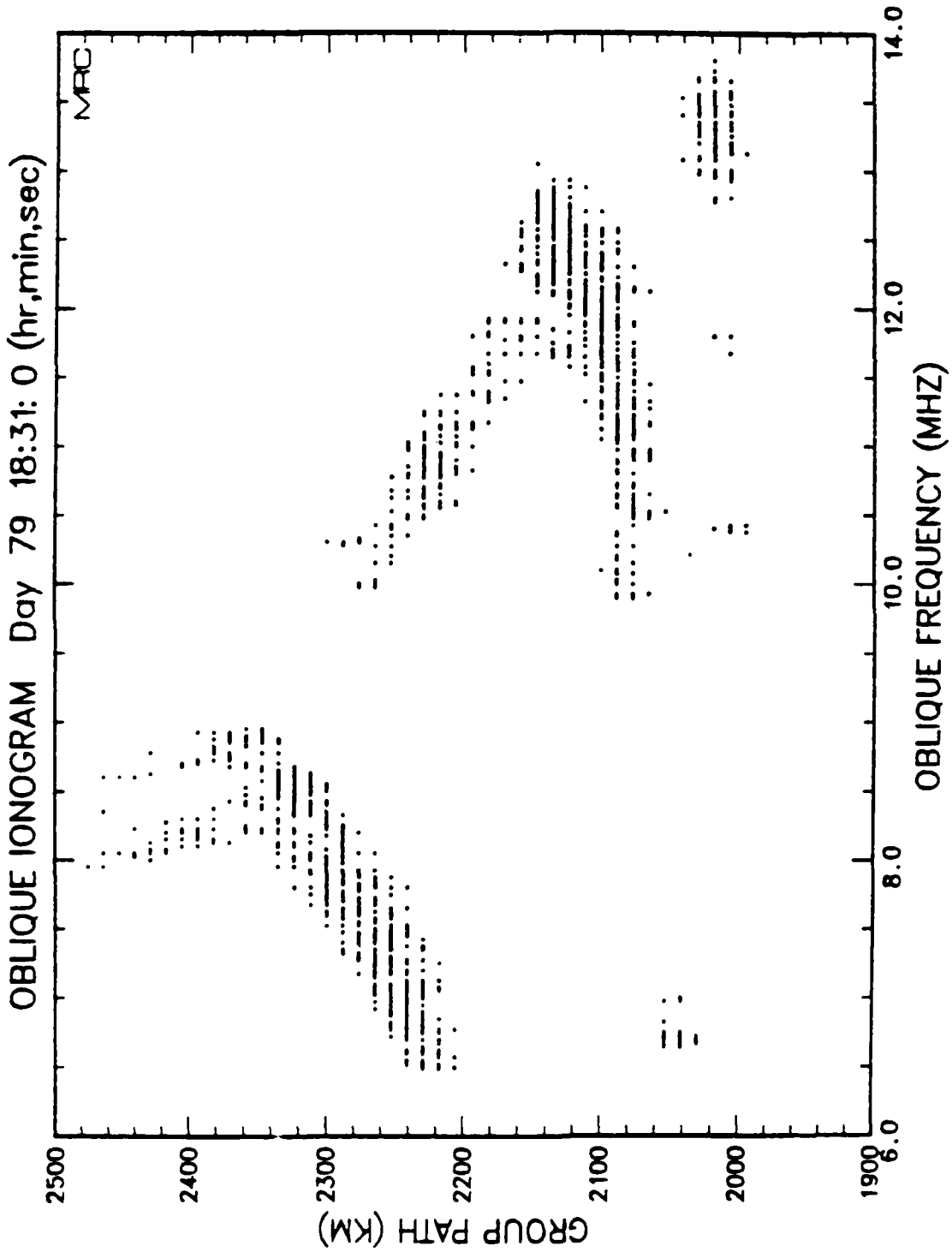


Figure 7. Example of an HF Channel Probe oblique ionogram measurement.

eters, and a power weighted chi square to the delay data is calculated (the weighting is done in dB). The layer parameters are then changed slightly and the direction toward decreasing chi square in parameter space is determined. After stepping the parameters in this direction, the process is repeated until chi square no longer decreases.

The result of one such nonlinear regression fit to the data of Figure 7 is shown in Figure 8. Signals corresponding to the two hop mode were ignored in the fit by using only data between 9.5 and 13 MHz. Similarly, the E-layer data was windowed out by using only data with a group path greater than 2050 km. The data in this fit has power greater than -30 dB with a peak power near -20 dB (relative to some standard). The fit minimizes

$$\chi^2 = \sum \text{Weight}_i \left(\frac{p_i^{\text{measured}} - p_i^{\text{QP}}}{\text{Error}} \right)^2 \quad (18)$$

where $\text{Weight}_i = \text{Power}_i - \text{Threshold}$, $\text{Threshold} = -30$ dB, and the error associated with each delay was arbitrarily set to 10 km (0.033 msec). Since all data points are given the same error, any other constant error would yield the same fit. Contributions to χ^2 for data beyond the junction frequency of the quasi-parabolic layer were calculated using the group path of the junction frequency for p_i^{QP} . Thus the fit is not overly affected by nose extensions.

2.5 HANDLING ABSOLUTE DELAY UNCERTAINTIES.

We will be examining data from the first two HF Channel Probe campaigns, in particular data taken on October 3, 1984 (Day 277, fall campaign) and March 20, 1985 (Day 79, spring campaign). All data from these two campaigns are subject to an approximate 200 usec uncertainty in absolute time delay measurements due to timing system drifts in the

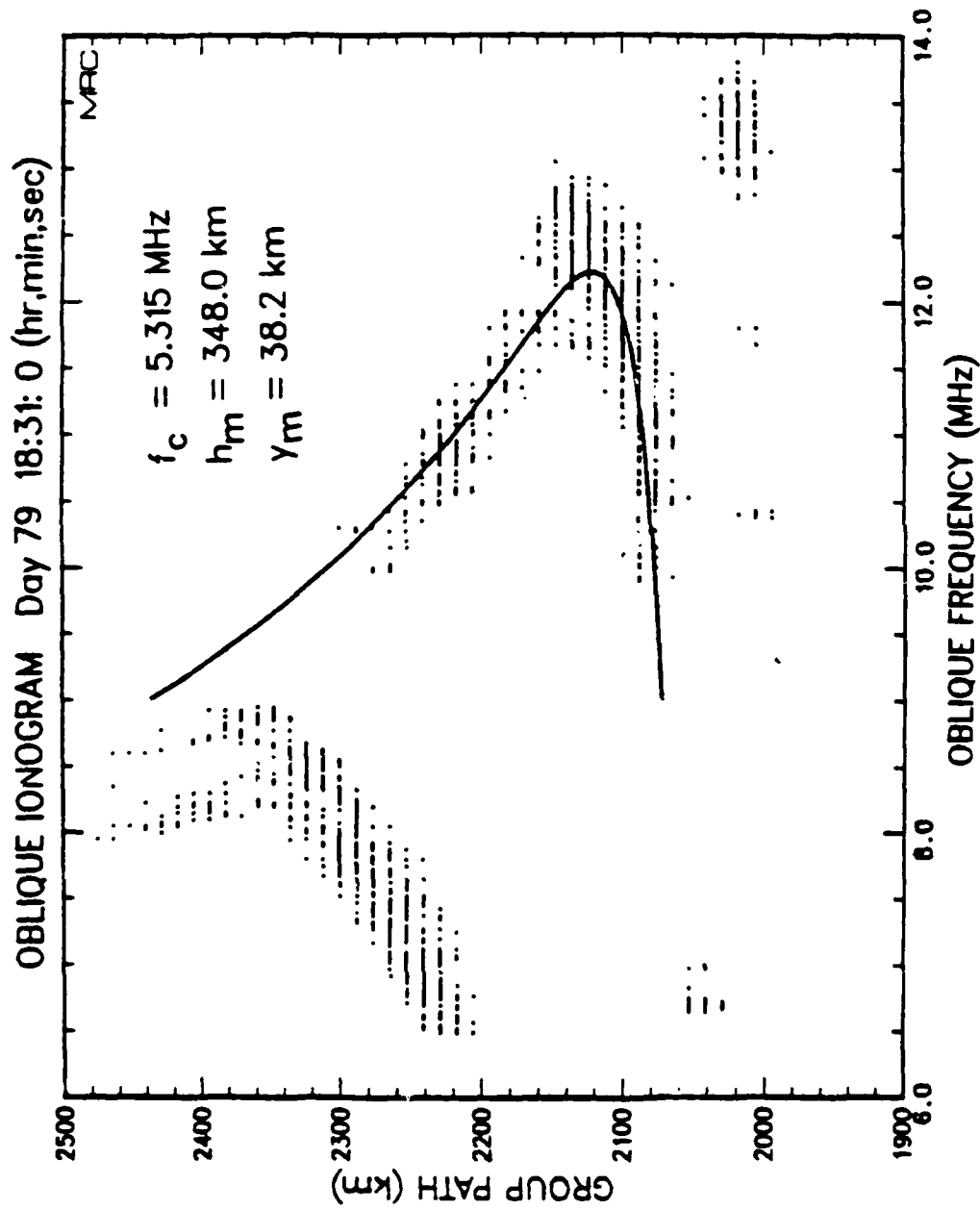


Figure 8. Result of a nonlinear regression fit to a quasi-parabolic layer for the ionogram of Figure 7.

experimental apparatus as well as uncertainties associated with the Transit satellite system used to update the system's internal clocks [Basler, Roy P., private communication]. This corresponds to a 60 km uncertainty in group path. Quasi-parabolic fits to the ionosphere can vary substantially over this range. As an example we show in Table 1 the results for quasi-parabolic fits of the ionogram shown in Figure 9a over the range $\Delta\tau = \pm 200$ μsec .

Table 1. Quasi-parabolic fits for forced absolute delay shifts $\Delta\tau$ of the measured data. The data and $\Delta\tau = 0$ fit are shown in Fig. 9a. The last column, column, χ^2/N_{data} is a measure of the goodness of the fit (see Eq. (18)). N_{data} is the number of data points used in the fit.

$\Delta\tau$ (μsec)	f_c (MHz)	h_m (km)	y_m (km)	χ^2/N_{data}
- 200	3.98	207.6	28.7	11.95
0	4.47	278.5	22.5	9.82
+ 200	5.03	356.8	21.8	20.35

Such differences produce substantial changes in ray path, and as we shall see in Section 3, quantities calculated in the DNA scintillation model can scale quite strongly with path length and electron density. An estimate of absolute delay can often be made by using the E-layer trace by assuming that the bottom of the trace lies at a height of, say, 100 km. However the E-layer trace is not always visible in the ionogram data. We note from Table 1, though, that the fit obtained in the $\Delta\tau = 0$ case was significantly better than for the other two cases, as is evidenced by the χ^2 of the fit. Thus there is reason to believe that the delay shift is relatively small in this example.

It is possible to include absolute delay shift as a parameter in the fitting process. Figure 9b shows the fit obtained for the preceding

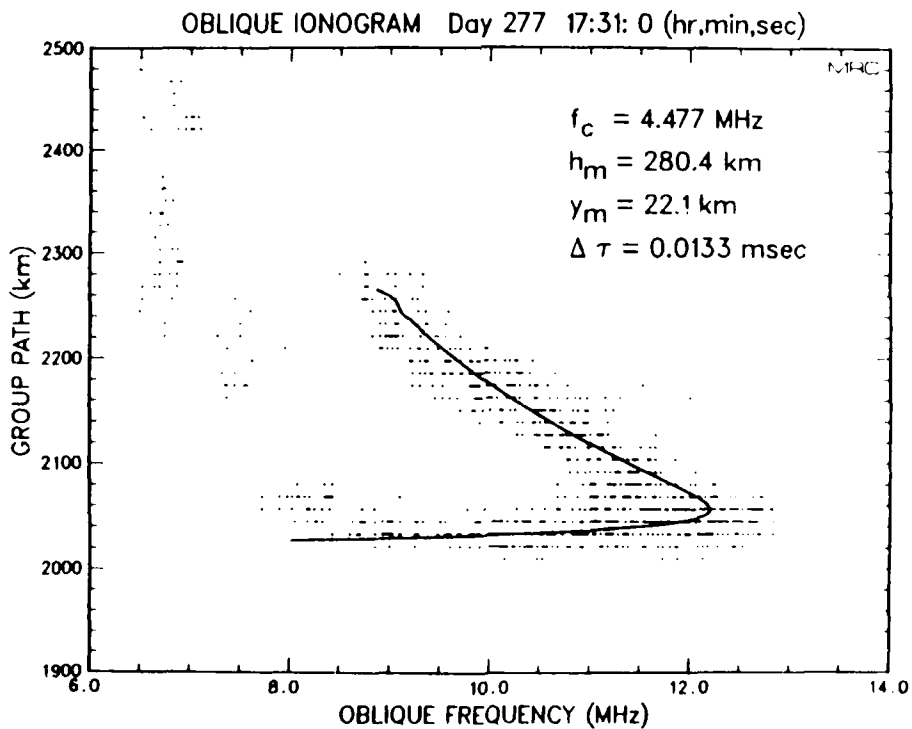
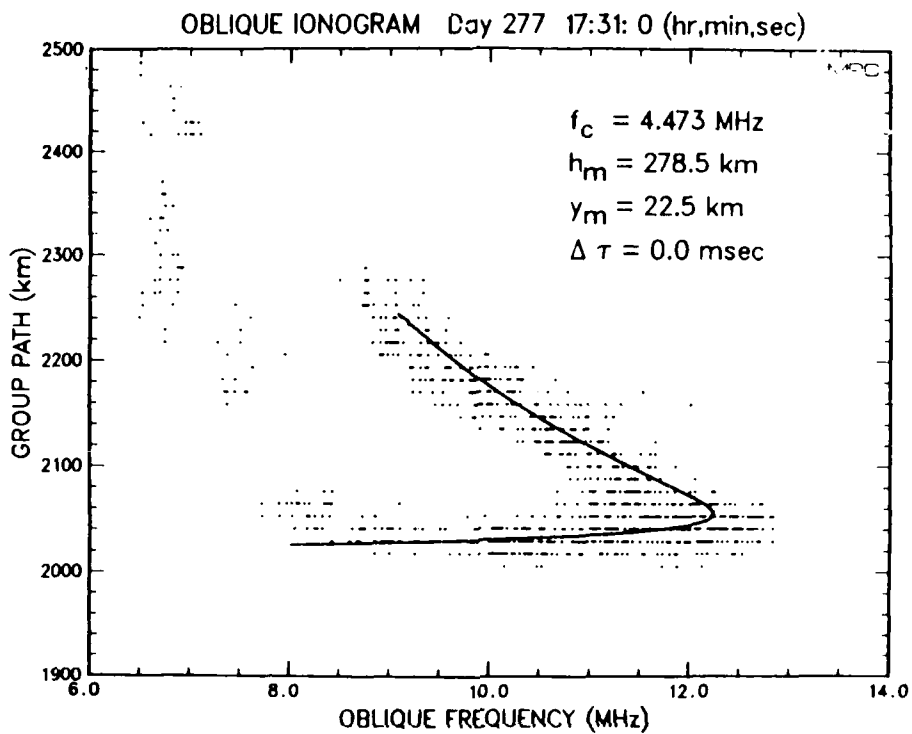


Figure 9. Comparison of ionogram fits for no delay shift $\Delta \tau = 0$ (a) and $\Delta \tau$ fitted (b).

example when this was done. Note that positive $\Delta\tau$ corresponds to additional delay added to the delay data and is not equivalent to applying an opposite shift to the layer height parameter. The delay shift of $\Delta\tau = 13.3 \mu\text{sec}$ (4 km in group path) is indeed small, but enough to improve the fit by five percent to a chi square of $\chi^2/N_{\text{data}} = 9.35$.

Table 2 summarizes results from this kind of analysis for two sequences of ionograms. The corresponding fits are shown in Figures 9 through 14. In all cases the fits were improved by including the delay shift (as is evidenced by comparison of the resultant chi squares), although the improvement is small in some cases. An independent check on the success of this fitting procedure in obtaining appropriate delay shifts is to check the resulting position of the E-layer trace. The first sequence (Day 277) was chosen as an example where no E-layer trace appears in the thresholded data (recall that a threshold of -30 dB was used for fitting purposes). Indeed, examination of the unthresholded ionograms (not shown) shows only faint E-layer traces. These traces are nearly correctly positioned in the 17:31 and 17:46 GMT cases (assuming that the bottom of the E-layer is at 100 km), but the 18:01 GMT E-layer trace is slightly higher than the previous two cases. The delay shifts obtained in the $\Delta\tau$ fit of this sequence are sufficient to produce consistency in these E-layer traces, even though no E-layer information was used in the fitting procedure. In the second sequence (Day 79), some evidence for the E-layer appears near the bottom of the plots. A virtual height of 100 km corresponds via Eq. (5) to a group path of 1942 km, and while the bottom of the E-layer trace is not really discernible in these plots because of thresholding, comparison with the $\Delta\tau = 0$ cases shows that a large improvement in the positioning of the E-layer has been made by fitting the delay shift (even in the Day 79 18:01 case, which showed the least improvement in χ^2).

Table 2. Comparison of ionogram fits for $\Delta\tau = 0$ and $\Delta\tau$ varied.

Condition	Day/time	f_c (MHz)	h_m (km)	y_m (km)	$\Delta\tau$ (μ sec)	χ^2/N_{data}
$\Delta\tau=0$	277 17:31	4.47	278.5	22.5	0	9.82
	17:46	4.72	306.7	22.1	0	9.61
	18:01	4.79	329.4	21.8	0	10.90
Best Fit	17:31	4.48	280.4	22.1	13.3	9.35
	17:46	4.71	305.3	21.3	16.4	9.36
	18:01	4.74	313.7	21.9	-44.4	10.12
$\Delta\tau=0$	079 18:01	5.29	360.2	45.3	0	8.92
	18:16	5.34	345.3	33.8	0	9.25
	18:31	5.32	348.0	38.2	0	8.11
Best Fit	18:01	5.10	333.4	49.1	-80.2	8.83
	18:16	5.10	311.7	37.0	-87.1	7.18
	18:31	5.08	317.7	37.6	-88.6	7.12

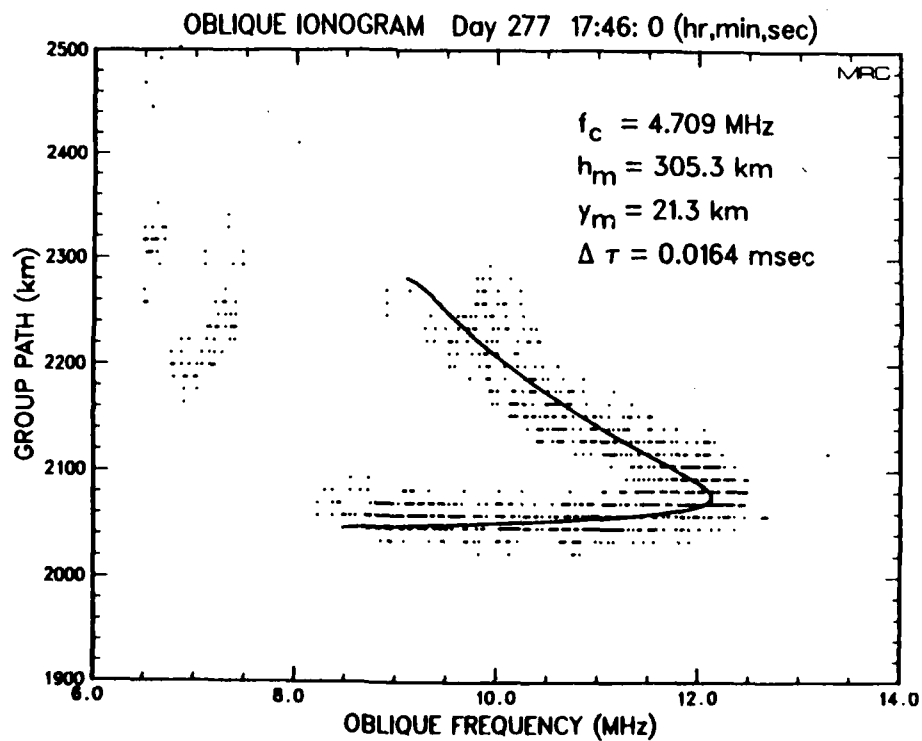
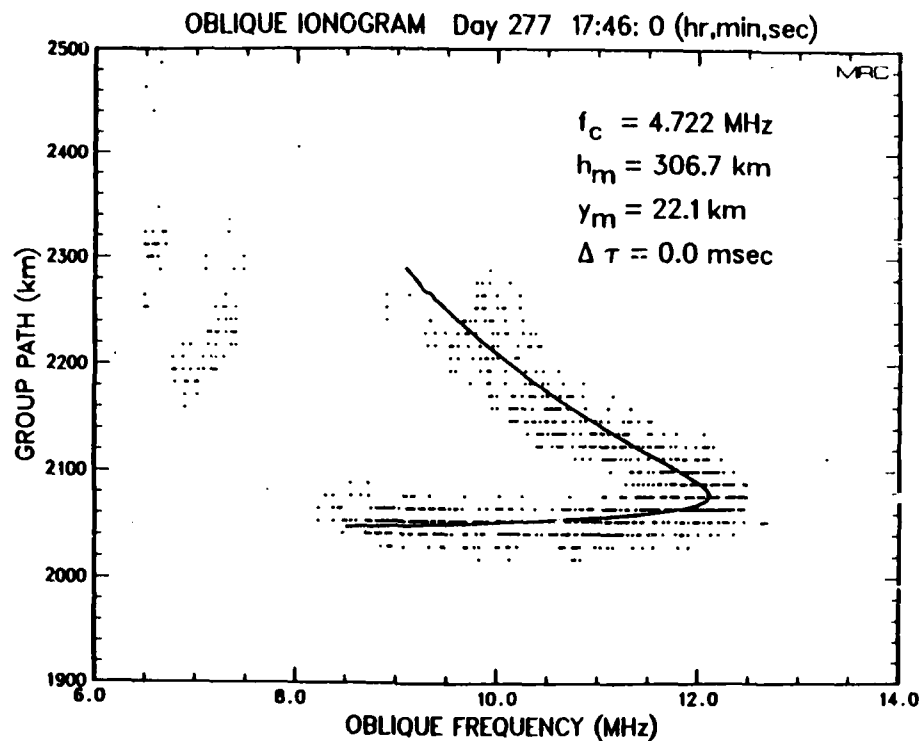


Figure 10. Comparison of ionogram fits for no delay shift $\Delta \tau = 0$ (a) and $\Delta \tau$ fitted (b).

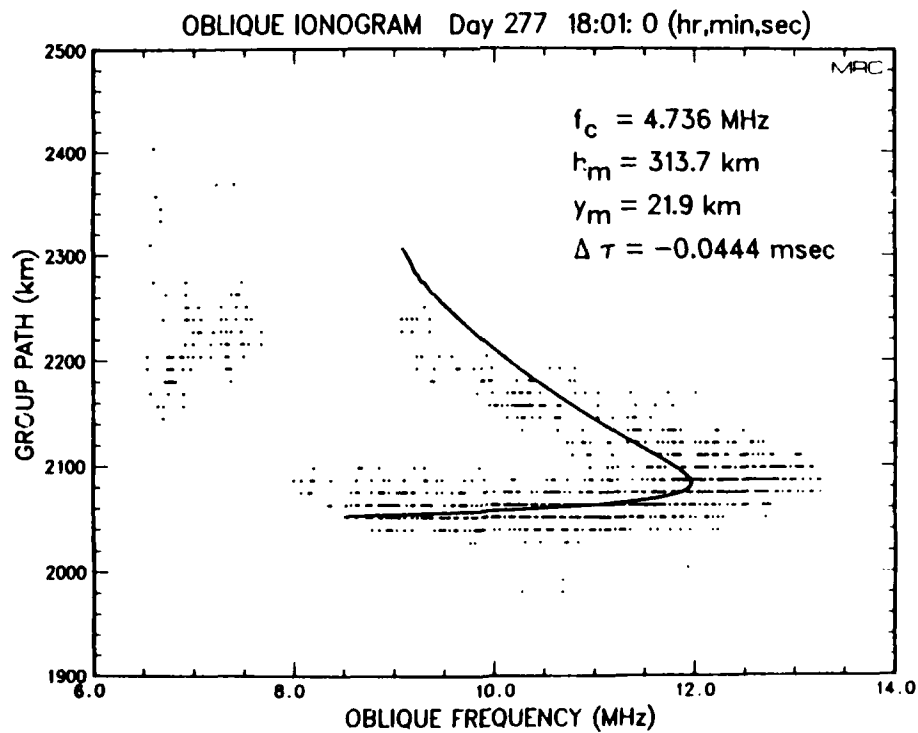
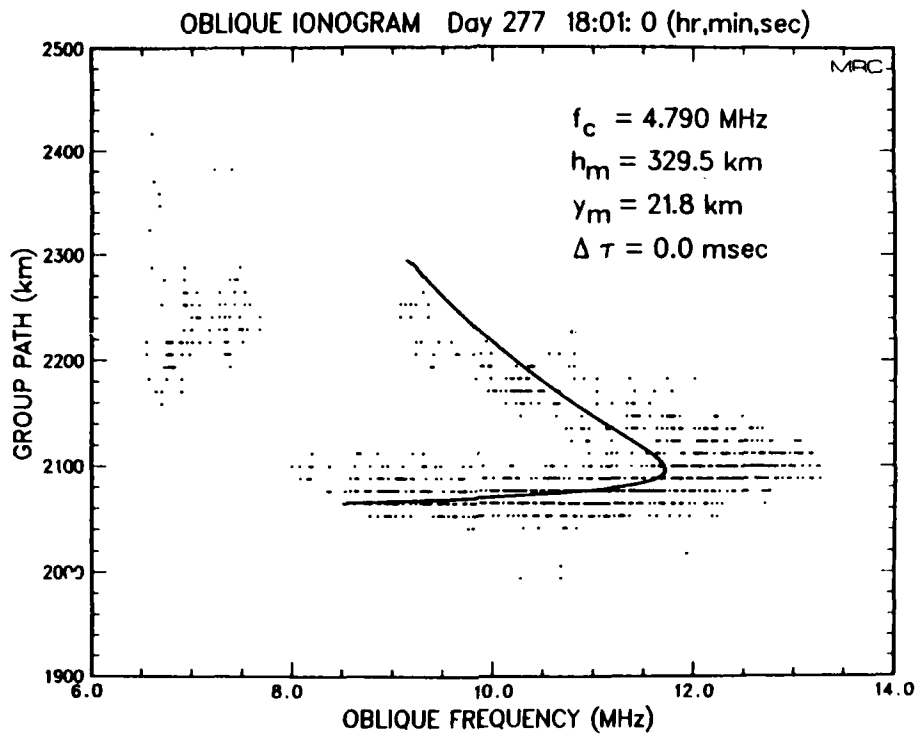


Figure 11. Comparison of ionogram fits for no delay shift $\Delta \tau = 0$ (a) and $\Delta \tau$ fitted (b).

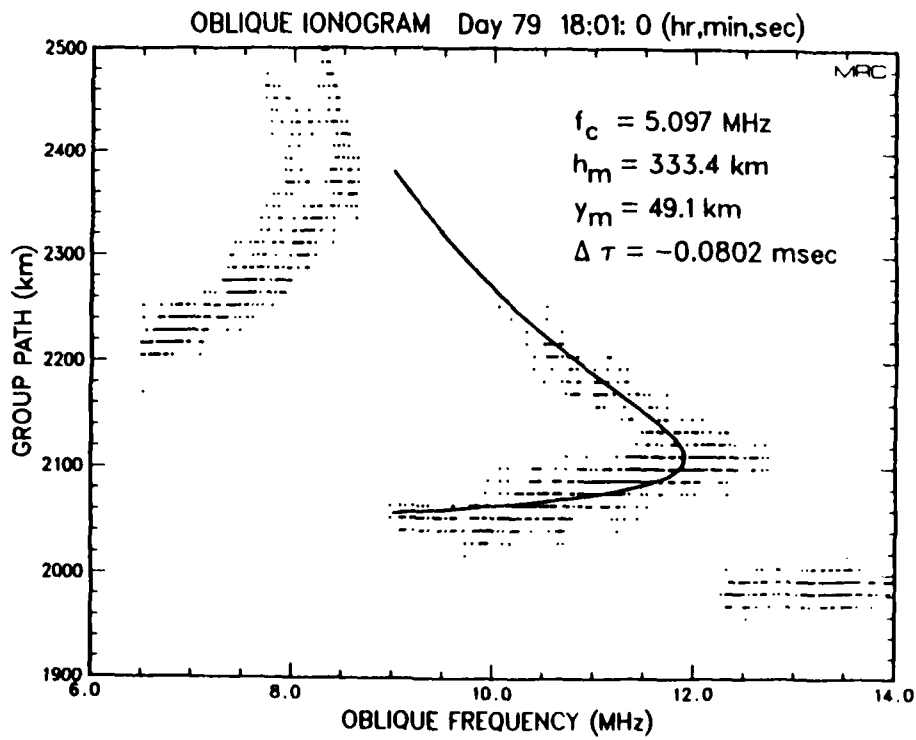
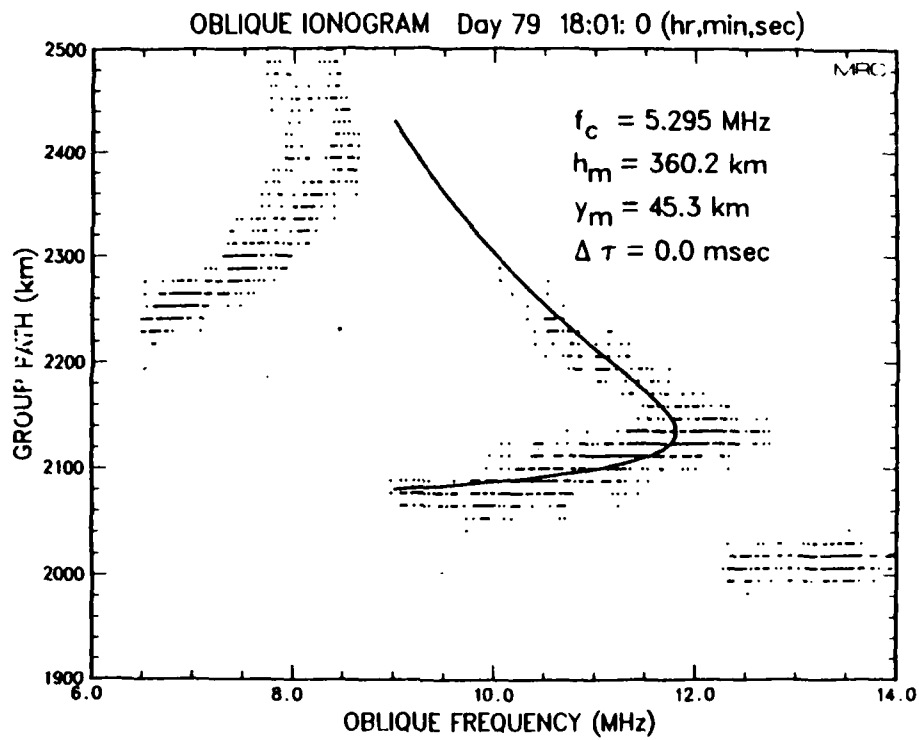


Figure 12. Comparison of ionogram fits for no delay shift $\Delta \tau = 0$ (a) and $\Delta \tau$ fitted (b).

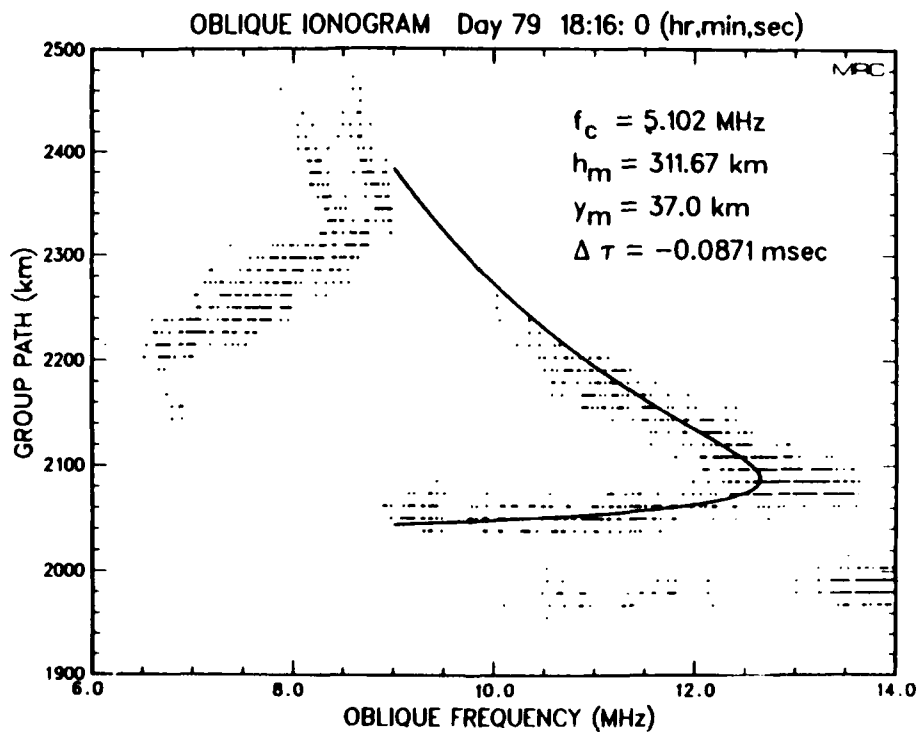
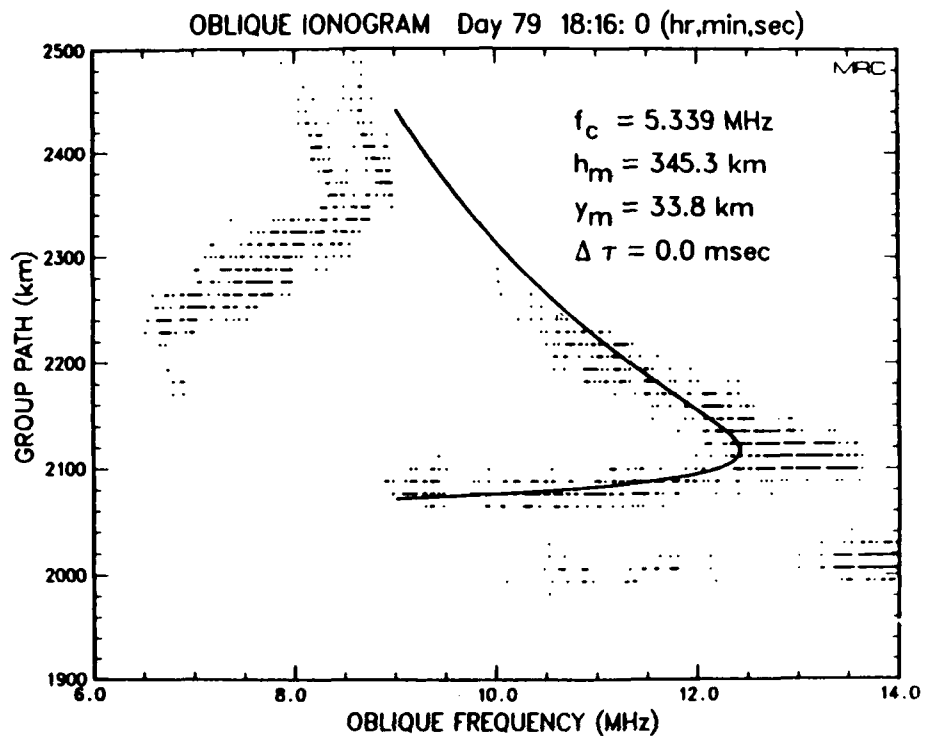


Figure 13. Comparison of ionogram fits for no delay shift $\Delta \tau = 0$ (a) and $\Delta \tau$ fitted (b).

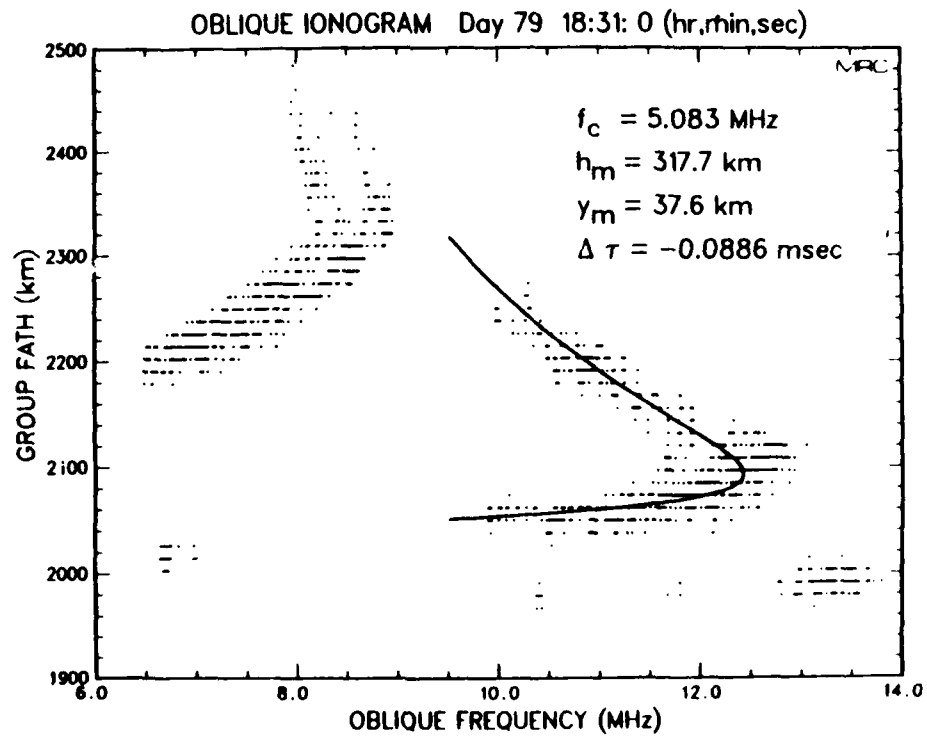
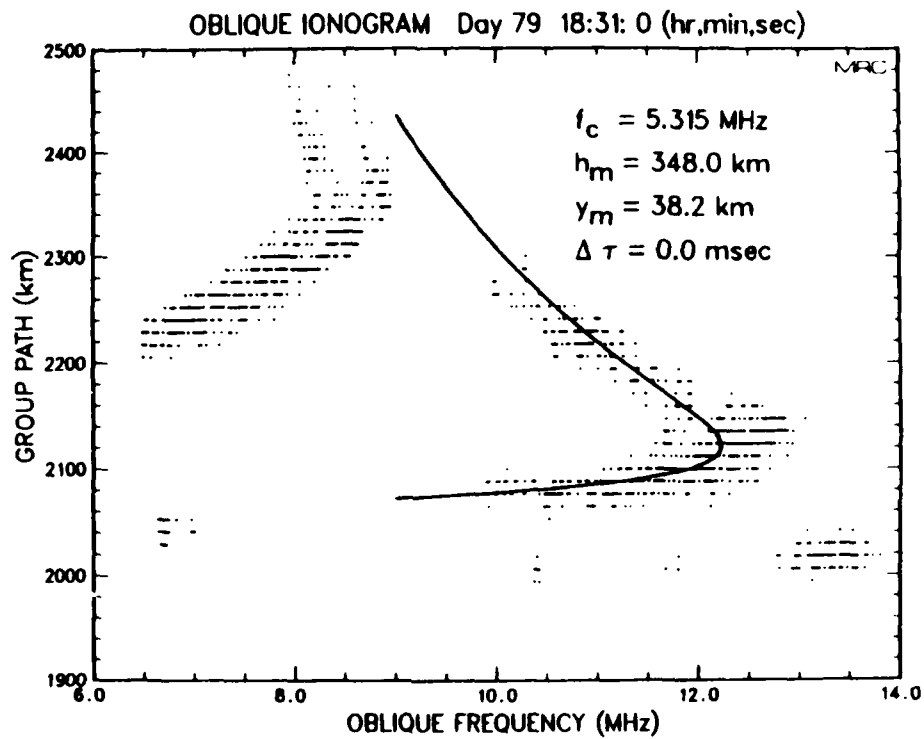


Figure 14. Comparison of ionogram fits for no delay shift $\Delta \tau = 0$ (a) and $\Delta \tau$ fitted (b).

Of the six cases examined in the two sequences above, three will be used in our analysis presented in Section 4 (Day 277 17:46, Day 79 18:16, Day 79 18:31). Three other cases not shown here will also be analyzed in Section 4 (see Figures 26, 28, and 32). The appearance of E-layer traces in the first two of these cases leaves little doubt that even though large delay shifts are obtained, they are appropriate. The last case shows only a hint of an E-layer trace in the full unthresholded ionogram (not shown), but the resultant delay shift seems to be consistent with positioning the bottom of this faint trace at 1942 km group path. However, we note that delay and doppler spread data associated with this trace is most poorly fit in the analysis of Section 4, and thus the layer parameters may be suspect. Even so, we conclude overall that the best fit ionospheric layer obtained by incorporating $\Delta\tau$ as a fit parameter is probably the appropriately positioned ionospheric layer.

SECTION 3

STOCHASTIC SIGNAL STRUCTURE PARAMETERS

3.1 INTRODUCTION.

The high latitude ionosphere is characterized by structured ionization aligned along the earth's magnetic field. These structures, or striations, are thought to be the result of structured electron precipitations which produce large scale irregularities that are subsequently convected through the auroral zone and polar caps. Smaller scale structures are produced as plasma instabilities (e.g. $E \times B$ or gradient drift instabilities) break up the large scale structure during transport [Kelley et al., 1982]. Rapid expansion along the field lines accounts for the quasi-cylindrical shape of the striations. Structure scale sizes parallel to the field may be more than ten times as large as the perpendicular scale sizes. It is the structure perpendicular to the field which dominates in producing scintillations of radio signals. These amplitude and phase fluctuations are the result of distortions imposed on the wave front as it propagates through these irregularities.

The DNA scintillation model was formulated as a relatively simple parametric description of the statistical effects of scatter from such structure. In this section we review the stochastic signal structure parameters relevant to the HF Channel Probe data and their calculation as formulated by Wittwer [Wittwer, 1979,1982]. The dependence of the model on its parameters will be mapped out, providing information on the sensitivity of the stochastic parameters to the model parameters. This will give insight into which parameters may be safely fixed and which should be varied when we fit the HF Channel Probe data in Section 4.

3.2 THE SCATTERING FUNCTION.

The distortions imposed on the wave front by structured ionization may be viewed in the ray optics approximation as micromultipath. Energy reaching the receiver in a particular mode (e.g. F-layer high ray or low ray) includes contributions from many paths, each the result of a slightly different sequence of scatterings from the structure. Signal components traveling over different paths will in general have different propagation times, and thus the received signal will be spread in time of arrival or delay. Temporal variation of the channel structure results in a corresponding frequency (doppler) broadening of the signal. Because the irregularity structure of the ionosphere must be described statistically, a statistical treatment of the delay and doppler spreading is required. The DNA scintillation model provides such a description. The HF Channel probe has measured the received power spectrum in delay and doppler for transmitted pseudo random noise. This spectrum, known as the scattering function, provides a direct measure of the spreading in delay and doppler due to the channel, as we will see below.

The response of a channel to a transmitted signal $E_0(t)$ may be modeled linearly [Bello, (1963)],

$$E(t) = \int_{-\infty}^{\infty} d\tau h(\tau;t)E_0(t-\tau) \quad . \quad (19)$$

The function $h(\tau;t)$ describes the response of the channel at time t to a signal transmitted at the earlier time $t-\tau$. If the transmitted signal were an impulse, $E_0(t) = \delta(t)$, then $h(\tau;t)$ would itself be the received field. Hence it is called the time-variant impulse response function. It depends on time because of the temporal variation of the channel. The dependence on delay is a reflection of multipath. The Fourier transform of the impulse response function, the time-variant channel transfer function, describes the carrier frequency response of the channel,

$$H(f;t) = \int_{-\infty}^{\infty} d\tau h(\tau;t) e^{-i2\pi f\tau} \quad . \quad (20)$$

It represents the response of the channel to a single frequency sinusoid.

To obtain a statistical description of the channel response we consider correlations of these channel system functions. Consider the two frequency - two time channel correlation function,

$$\begin{aligned} \Gamma(f_1, f_2; t_1, t_2) &= \langle H^*(f_1; t_1) H(f_2; t_2) \rangle \\ &= \int_{-\infty}^{\infty} d\tau \int_{-\infty}^{\infty} d\xi \langle h^*(\tau; t_1) h(\xi; t_2) \rangle e^{i2\pi(f_1\tau - f_2\xi)} \quad . \quad (21) \end{aligned}$$

Two useful approximations can be made. The first is that signals arriving with different delays (different paths) are uncorrelated. This uncorrelated scatter (US) approximation takes the form

$$\langle h^*(\tau; t_1) h(\xi; t_2) \rangle = \phi_h(\tau; t_1, t_2) \delta(\tau - \xi) \quad . \quad (22)$$

As a result, the two-frequency - two-time correlation function becomes a function only of the frequency separation $\Delta f = f_1 - f_2$,

$$\begin{aligned} \Gamma(f_1, f_2; t_1, t_2) &= \Gamma(\Delta f; t_1, t_2) \\ &= \int_{-\infty}^{\infty} d\tau \phi_h(\tau; t_1, t_2) e^{i2\pi\Delta f\tau} \quad . \quad (23) \end{aligned}$$

The second approximation is to assume that the statistics of the channel do not change with time so that the correlation functions depend only on time separation,

$$\phi_h(\tau; t_1, t_2) = \phi_h(\tau, \Delta t) \quad , \quad (24)$$

where $\Delta t = t_1 - t_2$. If this approximation is valid the channel is said to be wide sense stationary (WSS). Wide sense stationarity allows the time dependence of the correlation functions to be Fourier analyzed in a single doppler frequency domain f_d . We define the scattering function $S(\tau, f_d)$ by

$$\phi_h(\tau, \Delta t) = \int_{-\infty}^{\infty} df_d S(\tau, f_d) e^{i2\pi f_d \Delta t} \quad , \quad (25)$$

and thereby obtain under the assumption of wide sense stationary - uncorrelated scatter (WSSUS) the double Fourier transform relationship,

$$\Gamma(\Delta f; \Delta t) = \int_{-\infty}^{\infty} d\tau \int_{-\infty}^{\infty} df_d S(\tau, f_d) e^{i2\pi \Delta f \tau} e^{i2\pi f_d \Delta t} \quad . \quad (26)$$

Since $\Gamma(\Delta f; \Delta t)$ is a correlation function in both of its arguments, $S(\tau, f_d)$ is properly interpreted as a power spectrum in both arguments. To see this we consider the autocorrelation of the received field at two different times,

$$\begin{aligned} \langle E^*(t) E(t-\Delta t) \rangle &= \int_{-\infty}^{\infty} d\tau \int_{-\infty}^{\infty} d\xi \langle h^*(\tau; t) h(\xi; t-\Delta t) \rangle \langle E_0^*(t-\tau) E_0(t-\Delta t-\xi) \rangle \\ &= \int_{-\infty}^{\infty} d\tau \int_{-\infty}^{\infty} d\xi \phi_h(\tau; \Delta t) \delta(\tau-\xi) \langle E_0^*(t-\tau) E_0(t-\Delta t-\xi) \rangle \quad (27) \\ &= \int_{-\infty}^{\infty} d\tau \phi_h(\tau, \Delta t) \langle E_0^*(t-\tau) E_0(t-\Delta t-\tau) \rangle \end{aligned}$$

where in the first line we have assumed that the statistics of the channel are independent of the transmitted signal and in the second line that the WSSUS assumption holds. In terms of the scattering function, this is

$$\langle E^*(t) E(t-\Delta t) \rangle = \int_{-\infty}^{\infty} d\tau \int_{-\infty}^{\infty} df_d S(\tau, f_d) e^{i2\pi f_d \Delta t} \langle E_0^*(t-\tau) E_0(t-\Delta t-\tau) \rangle. \quad (28)$$

Setting $\Delta t = 0$ yields the expression for the received signal strength in terms of the transmitted signal strength,

$$\langle |E(t)|^2 \rangle = \int_{-\infty}^{\infty} d\tau \int_{-\infty}^{\infty} df_d S(\tau, f_d) \langle |E_0(t-\tau)|^2 \rangle. \quad (29)$$

The scattering function is thus the delay-doppler power spectrum of the received signal due to the channel.

In practice, the scattering function may be measured by transmitting a wideband signal and cross correlating the received signal with a delayed version of the transmitted signal. For transmitted random noise this yields the impulse response function (up to an amplitude factor that can be included in the definition of $h(\tau;t)$),

$$\begin{aligned} \langle E^*(t) E_0(t-\tau) \rangle &= \int_{-\infty}^{\infty} d\xi h^*(\xi;t) \langle E_0^*(t-\xi) E_0(t-\tau) \rangle \\ &= \int_{-\infty}^{\infty} d\xi h^*(\xi;t) \delta(\tau-\xi) \\ &= h^*(\tau;t). \end{aligned} \quad (30)$$

Correlating this result at separated times yields $\phi_h(\tau, \Delta t)$ if WSSUS is assumed. Finally, Fourier transforming ϕ_h over Δt to the doppler domain gives the scattering function $S(\tau, f_d)$.

A sample scattering function measurement from the HF Channel Probe is shown in Figure 15. The peak power in this plot has been normalized to unity. The delay origin is at 6.7 msec and has been adjusted to allow for a 200 μ sec delay introduced by the experimental apparatus. Two distinct modes are apparent. Comparison with the ionogram of Figure 10, taken one minute earlier, shows that these modes correspond to the low and high rays of the F-layer. Each mode exhibits a substantial spread in both delay and doppler, characterized by standard deviations which we denote respectively σ_τ and σ_d . The doppler spread, ν_d , is conventionally defined as the 1/e point of the scattering function (i.e., for a gaussian $\nu_d = \sqrt{2}\sigma_d$). Because of the Fourier transform relationship between the scattering function and the two frequency - two time channel correlation function, Eq. (26), these widths imply corresponding coherence widths in the conjugate variables, i.e. for gaussian scattering functions,

$$f_0 = 1/(2\pi\sigma_\tau) \quad \tau_0 = 1/(\pi\nu_d) \quad . \quad (31)$$

The coherence bandwidth f_0 represents the frequency spread over which signals will remain correlated. Similarly, the decorrelation time τ_0 is a measure of the time over which signals will remain correlated. Both of these quantities are of fundamental importance in the design and performance assessment of HF communication systems. Broad delay and doppler spreads translate to narrow coherence bandwidths and short decorrelation times. This situation is likely to occur under nuclear conditions, and in order to design systems which will be free of intersymbol interference in such cases one must be able to estimate these signal structure parameters given information about the environment. The DNA scintillation model was formulated to provide such a characterization for transionospheric satellite communication links. The HF Channel Probe scattering function measurements afford us the opportunity to test the applicability of this formulation on internally reflected paths at HF over a variety of conditions.

DNA Polar Measurements : Scattering Function

Day : Hour : Min : Sec = 277 : 17 : 47 : 03

Carrier frequency = 11.150 MHz

Delay 0 = 6.70 msec

Receiver 1

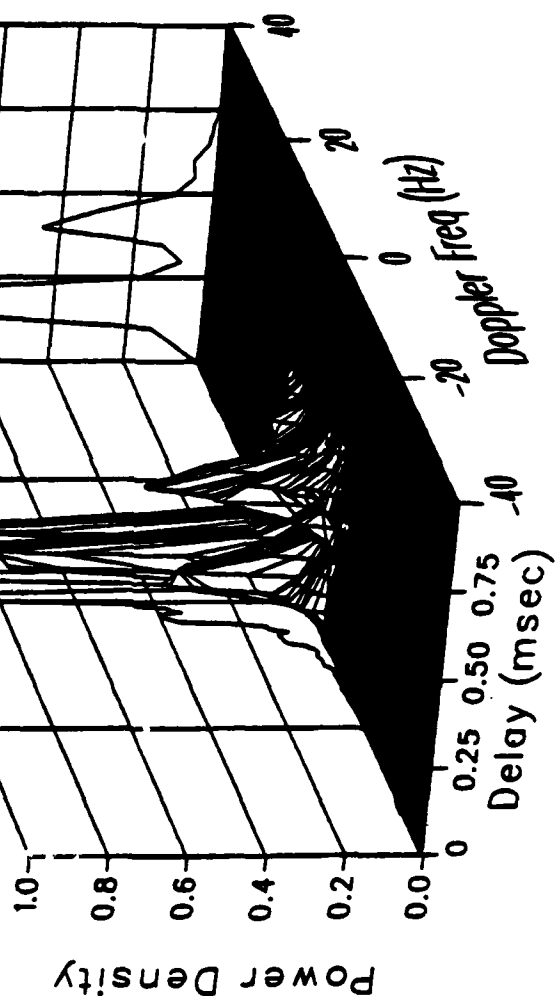


Figure 15. Example of an HF Channel Probe scattering function measurement corresponding to the ionogram of Figure 10.

3.3 THE DNA SCINTILLATION MODEL.

In order to obtain a statistical description of signal propagation effects, one must have a statistical description of the environment affecting the propagation. It is therefore necessary to consider the correlation function of electron density variations in the ionosphere,

$$\Gamma_{\Delta N}(\vec{\rho}) = \langle \Delta N_e(\vec{r}) \Delta N_e(\vec{r} + \vec{\rho}) \rangle \quad (32)$$

where $\Delta N_e(\vec{r}) = N_e(\vec{r}) - \langle N_e(\vec{r}) \rangle$. The three-dimensional Fourier transform of this correlation function,

$$\Phi_N(\vec{k}) = \int d^3\rho e^{i\vec{k} \cdot \vec{\rho}} \Gamma_{\Delta N}(\vec{\rho}) \quad (33)$$

is a spectral density function that is readily related to the three-dimensional power spectral density (PSD) of index of refraction fluctuations. The connection is made by considering the approximation

$$\mu = [1 - f_p^2/f^2]^{1/2} \approx 1 - (1/2)(f_p^2/f^2) \quad (34)$$

with $f_p^2 = (c^2 r_e / \pi) N_e$ (r_e is the classical electron radius, $r_e = 2.82 \times 10^{-15} \text{m}$). A deviation in electron density ΔN_e produces a corresponding deviation in the index of refraction,

$$\Delta\mu = - [(\lambda^2 r_e) / (2\pi)] \Delta N_e \quad (35)$$

Thus the PSD for index of refraction fluctuations is related to that of the electron density variations by,

$$\text{PSD}(\vec{k}) = [(\lambda^2 r_e)/(2\pi)]^2 \Phi_N(\vec{k}) \quad . \quad (36)$$

The DNA scintillation model is based on a power law representation of this PSD, which for axisymmetric striations may be written as

$$\text{PSD}(\vec{k}_\perp, k_\parallel) = \frac{8\pi^{3/2} \langle \Delta\mu^2 \rangle L_\perp^2 L_\parallel \Gamma(n)/\Gamma(n-3/2)}{(1 + L_\perp^2 k_\perp^2 + L_\parallel^2 k_\parallel^2)^n} \quad . \quad (37)$$

In this expression, \vec{k}_\perp is the spatial wave vector perpendicular to the earth's magnetic field, k_\parallel is the spatial wave number parallel to the magnetic field, L_\perp and L_\parallel are the structure outer scale sizes relative to the magnetic field, $\langle \Delta\mu^2 \rangle$ is the index of refraction variance, and n is the power law index. The corresponding one-dimensional, or in situ PSD varies as $1/(k^{2n-2})$ for large k , so the spectral index (SI) is defined to be $\text{SI} = 2n-2$. The normalization of Eq. (37) requires $n > 1.5$, and Wittwer's formulation [Wittwer, 1979, 1982] is valid in the range $1.5 < n < 4$.

The value of the spectral index depends both on the striation profile and on the distribution of striation sizes [Wortman and Kilb] While a value of $\text{SI} = 2$ has been advocated for a number of years on the basis of several in situ measurements (see references cited in Wittwer, 1979), more recent DNA HILAT measurements have yielded values (averaged over more than a year in the region of the HF Channel Probe experiment) of $\text{SI} = 1.5$ (day), 1.63 (night) with a significant probability of occurrence throughout the range 0.5 to 2.5 [Basler et al., 1985].

While Wittwer's formulation of the DNA scintillation model allows the calculation of a number of stochastic signal structure parameters (Rayleigh phase variance, mean square log amplitude fluctuation, S_4 scintillation index, parallel decorrelation time, angle of arrival vari-

ance), we will concentrate on the two relevant to the HF Channel Probe scattering function measurements the delay spread σ_τ and the decorrelation time perpendicular to the ray path, which we label τ_0 (actually $\tau_0 = \min(\tau_\perp, \tau_\parallel)$, but for the paths we consider the perpendicular decorrelation time is always smaller than the parallel decorrelation time). Again, the doppler spread is related to the decorrelation time by $\nu_d = 1/(\pi\tau_0)$.

A differential phase variance can be obtained from Eq. (27) by considering correlations of the phase shift imparted in traversing segments of the scattering region larger than the correlation distance of the index of refraction fluctuations [Wittwer, 1979]. This then assumes that the ray remains in the scattering region for distances longer than this correlation length in the ray direction. Over the Narssarsuaq to Thule path, the magnetic dip is near 80 deg. and the angle between the ray path and the magnetic field lines typically will not be less than 60 deg. in the refracting region. Thus we are far from being parallel to the magnetic field lines where such an assumption might not be valid. Letting ds represent the differential geometric ray pathlength, the differential phase variance is

$$\frac{d\sigma_\phi^2}{ds} = \frac{8\pi^{5/2}\Gamma(n-1)}{\Gamma(n-3/2)} \frac{r_e^2}{k^2} \xi \langle N_e \rangle^2 \frac{L_\perp}{(\cos^2\psi + a_0^2 \sin^2\psi)^{1/2}}, \quad (38)$$

where $a_0 = L_\parallel/L_\perp$ and ψ is the angle between the ray direction and the magnetic field lines. We have assumed that the index of refraction variance is related to the electron density variance by $\langle \Delta\mu^2 \rangle = (2\pi r_e/k^2)^2 \langle \Delta N_e^2 \rangle$. This approximation assumes that the carrier frequency of the signal is always sufficiently larger than the local plasma frequency so that the approximation $\mu = (1 - f_p^2/f^2)^{1/2} \approx 1 - (1/2)(f_p^2/f^2)$ is valid. This will be true even near the reflection point for the highly oblique paths we are

considering. We have also assumed that the electron density variance is proportional to the square of the average electron density,

$$\langle \Delta N_e^2 \rangle = \xi \langle N_e \rangle^2 \quad (39)$$

The total phase variance σ_ϕ^2 is the integral over the ray path (ie., from 0 to s_t) of Eq. (38).

Wittwer's expression for delay spread [Wittwer, 1982] in the axisymmetric striation case we are considering becomes,

$$\sigma_\tau^2 = \frac{\sigma_{\phi R}^2}{k^2 c^2} + \frac{H_m}{k^4 c^2} \int_0^{s_t} \frac{ds}{s^2} \int_0^s \frac{ds'}{s'^2} [I_U^2(s') + I_V^2(s')] \quad (40)$$

where,

$$I_U(s') = \frac{2B_n}{L_\perp^2} \int_0^{s'} ds \frac{d\sigma_\phi^2}{ds} s^2 \quad (41)$$

$$I_V(s') = \frac{2B_n}{L_\perp^2} \int_0^{s'} ds \frac{d\sigma_\phi^2}{ds} \frac{s^2}{(\cos^2 \psi + a_0^2 \sin^2 \psi)} \quad (42)$$

$$H_m = (B_n \sigma_\phi^2)^{4/m} - 2 \quad (43)$$

$$m = \begin{cases} 2n-2 & n < 2 \\ 2 & n > 2 \end{cases} \quad (44)$$

and $\sigma_{\phi R}^2$ is the Rayleigh phase variance defined by Wittwer. This term is always dominated by the second term for the paths we consider, as we shall see below, and the calculation of $\sigma_{\phi R}^2$ is sufficiently complicated that we

will not repeat it here, but refer the reader to the references [Wittwer, 1979, 1982]. The constant B_n is given by

$$B_n = \frac{\Gamma(n-1/2)}{c_n \pi^{1/2} \Gamma(n-1)} \left[\frac{1}{3} + h(\epsilon) \right] \frac{f(n)}{(n-1)}, \quad (45)$$

where

$$h(\epsilon) = \begin{cases} -\ln(\epsilon) & n = 2 \\ \frac{1}{|4-2n|} [1 - \epsilon^{|4-2n|}] & \text{otherwise} \end{cases}, \quad (46)$$

$$f(n) = \begin{cases} (n-1)^{-0.14} & n < 2 \\ (n-1)^{-0.30} & n \geq 2 \end{cases} \quad (47)$$

$$c_n = \frac{\epsilon^{n-1} K_{n-1}(\epsilon)}{2^{n-2} \Gamma(n-1)} \quad (48)$$

and ϵ is the ratio of inner to outer structure scale sizes. For ϵ small, the hyperbolic Bessel function may be expanded,

$$K_{n-1}(\epsilon) \approx (1/2) \Gamma(n-1) (\epsilon/2)^{-(n-1)}, \quad (49)$$

which yields $c_n \approx 1$.

The signal decorrelation time is estimated in the frozen plasma approximation (assuming fixed transmitter and receiver) as

$$\tau_0 = \frac{B(n, \sigma_\phi^2)}{B_n^{1/m}} \frac{L_\perp}{v_\perp} \left[\int_0^{st} ds \frac{d\sigma_\phi^2}{ds} \left\{ \frac{1 + \cos^2\psi + a_0^2 \sin^2\psi}{\cos^2\psi + a_0^2 \sin^2\psi} \right\}^{m/2} \right]^{-1/m} \quad (50)$$

where v_\perp is the velocity of plasma motion perpendicular to the ray path, and which we have taken to be constant and removed from the integral. The function $B(n, \sigma_\phi^2)$ helps insure the appropriate behavior for small phase variances, and is given by

$$B(n, \sigma_\phi^2) = \min[1, (-0.34 n^2 + 2.51 n - 2.00)(\sigma_\phi^2 B_n)^{1/m}] \quad (51)$$

The parameters required for the calculation of delay and doppler spreads in this formulation are then n (or equivalently the spectral index $SI = 2n-2$), L_\perp , L_\parallel , v_\perp , $\xi = \langle \Delta N_e^2 \rangle / \langle N_e \rangle^2$, and ϵ . Of these, v_\perp affects only the calculation of doppler spread (or τ_0), and enters this linearly.

3.4 PARAMETER DEPENDENCE.

As we have just seen, six parameters are required by the DNA scintillation model to calculate delay and doppler spreads. Testing the model against the HF Channel Probe data requires adjusting these parameters in a fit of the measured scattering functions. A single mode yields only two data points, a delay spread and a doppler spread, and hence only two parameters can be fit unless some relationship between the parameters of different modes is assumed. This possibility will be discussed further in Section 4, but for the present we will assume that each mode will be fit independently. Since v_\perp appears only in the doppler calculation, doppler spreads can always be fit by adjusting v_\perp after the delay spread has been fit. Thus of the remaining five parameters, four must be fixed and one varied in fitting the delay data. For this reason it is important to discern which of these five parameters is the most sensitive.

We have mapped out the parameter dependence of the DNA scintillation model for a nominal ionosphere, that corresponding to the oblique ionogram of Figure 2. This quasi-parabolic layer has a critical frequency of 4.5 MHz at 300 km, and a half width of 50 km. The ray paths for the 10 MHz rays used were shown in Figure 3. The high ray travels a significant distance at nearly the peak of the layer, and scintillations calculated over the high ray will be correspondingly larger for the same parameters than for the low ray. Figures 16 - 25 show the variation of delay spread and doppler spread with each of the parameters. Base values for the parameters were $SI = 2$, $L_{\perp} = 10$ km, $L_{\parallel} = 100$ km, $\xi = 0.2$, $\epsilon = 0.001$, and $v_{\perp} = 50$ m/sec.

Figures 16 and 17 show a very strong dependence on the spectral index in the vicinity of $SI = 2$. For example, the delay spread varies by an order of magnitude for the low ray and two orders of magnitude for the high ray for SI ranging from 1.5 to 2.5. The dependence on L_{\perp} , shown in Figures 18 and 19, is also fairly strong. However for $L_{\perp}/L_{\parallel} \approx 0.05 - 0.1$, an expected reasonable range, the variation is less than a factor of two for any of the quantities. Figures 20 and 21 show almost no dependence on L_{\parallel} once it is two or three times larger than L_{\perp} . Thus L_{\parallel} may be safely fixed at 100 km without affecting the fit of the HF Channel Probe data. The ratio of the inner to outer structure scale size, ϵ , is poorly known, but Figures 22 and 23 show the dependence on this parameter to be exceedingly small over many orders of magnitude. It enters into the calculation of the coefficient B_n logarithmically for $n=2$ (the case shown here) and as a low power otherwise, but in any case the dependence is weak. We will fix ϵ at 0.001.

The linear dependence of the delay spread and the square root dependence of the doppler spread on ξ , shown in Figures 24 and 25 is easily understood. From Eq. (38) we note that $d\sigma_{\phi}^2/ds$ scales as $\xi \langle N_e \rangle^2$. Examination of Eq. (10) then shows that the doppler spread will scale as

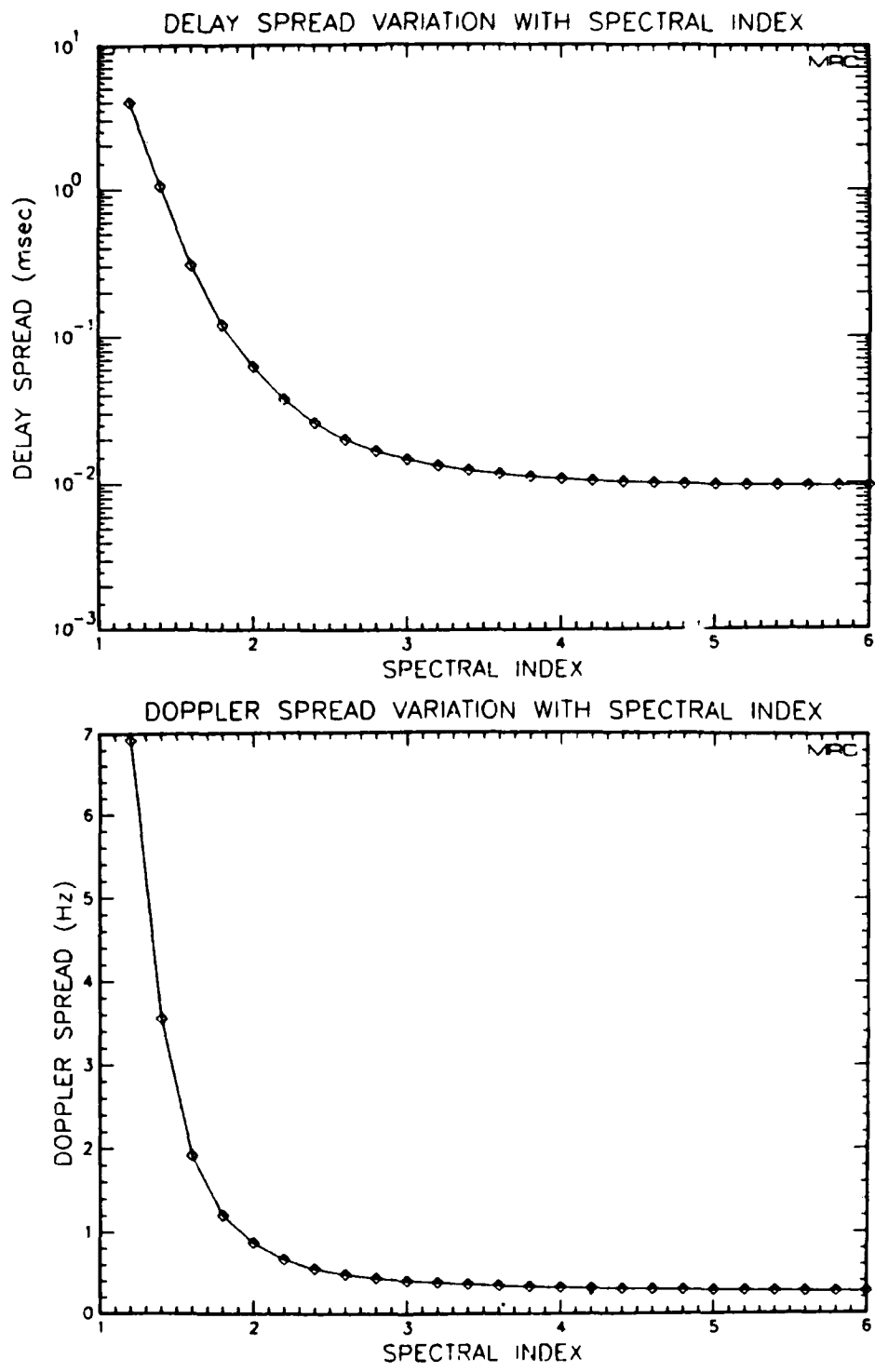


Figure 16. Delay and doppler spread variation with spectral index for the low ray of Figure 3. The remaining parameters are fixed at $L_{\perp} = 10$ km, $L_{\parallel} = 100$ km, $\xi = 0.2$, $\epsilon = 0.001$, $v_{\perp} = 50$ m/sec.

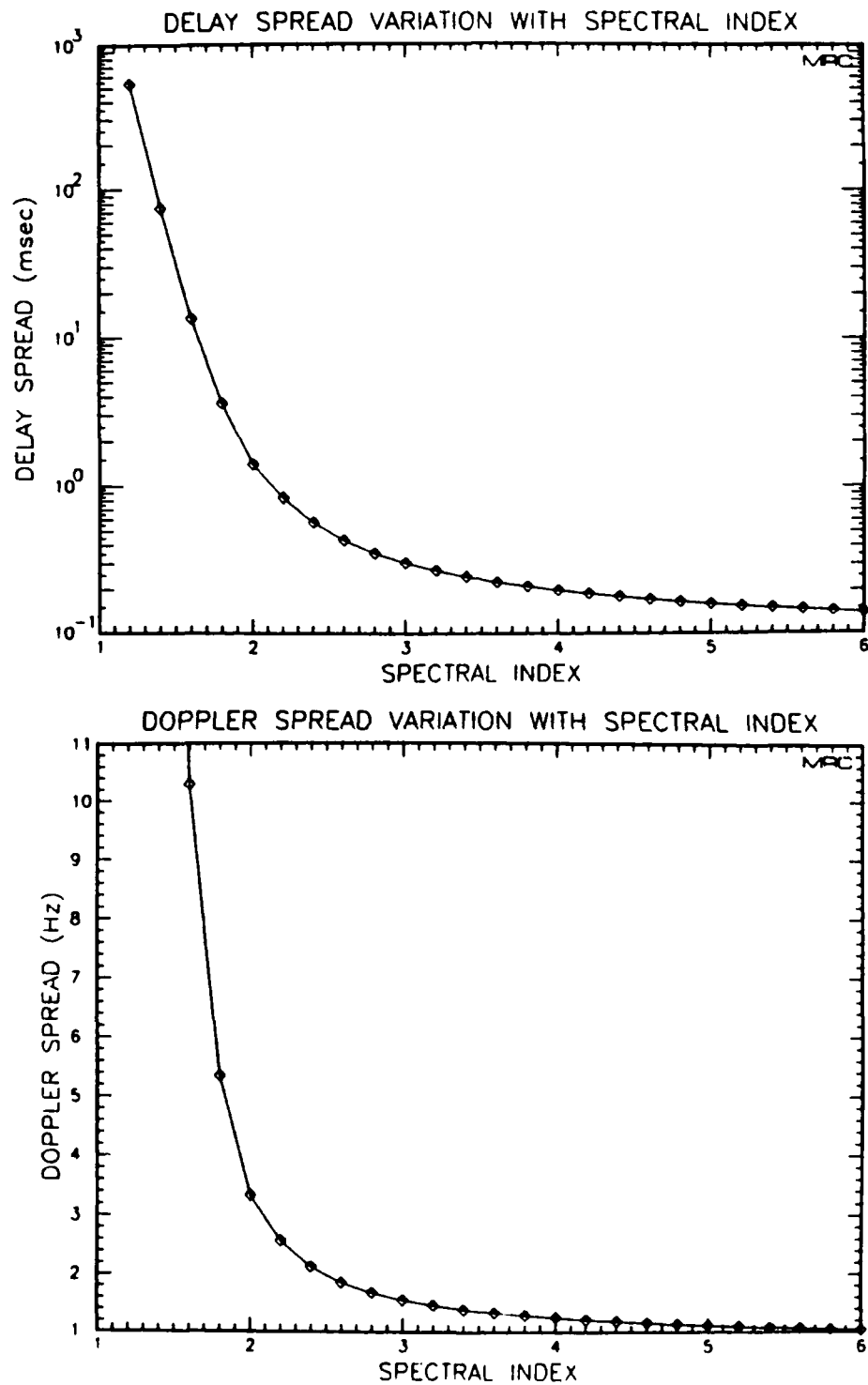


Figure 17. Delay and doppler spread variation with spectral index for the high ray of Figure 3. The remaining parameters are fixed at $L_{\perp} = 10$ km, $L_{\parallel} = 100$ km, $\xi = 0.2$, $\epsilon = 0.001$, $v_{\perp} = 50$ m/sec.

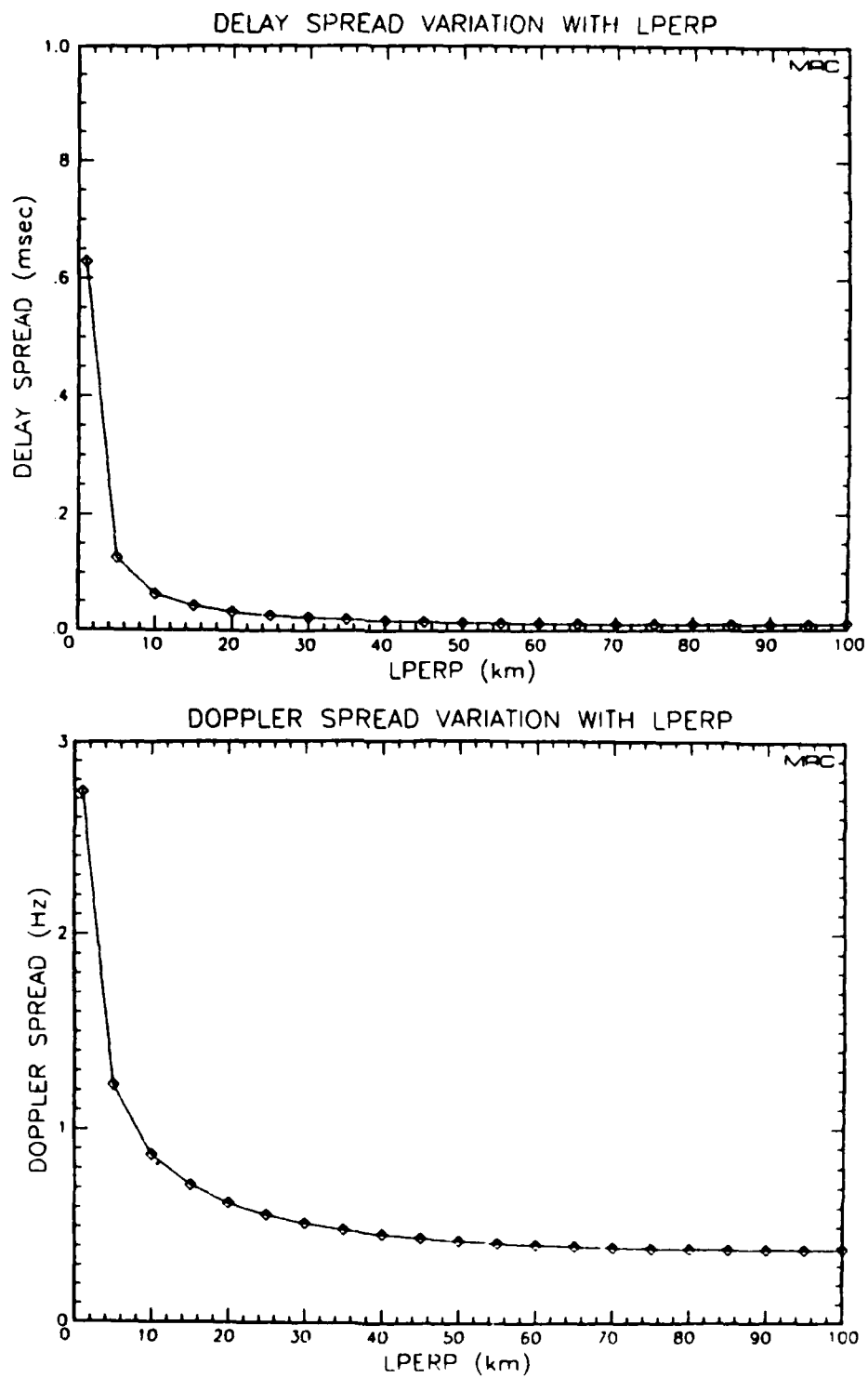


Figure 18. Delay and doppler spread variation with L_{\perp} for the low ray of Figure 3. The remaining parameters are fixed at $SI = 2$, $L_{\parallel} = 100$ km, $\xi = 0.2$, $\epsilon = 0.001$, $v_{\perp} = 50$ m/sec.

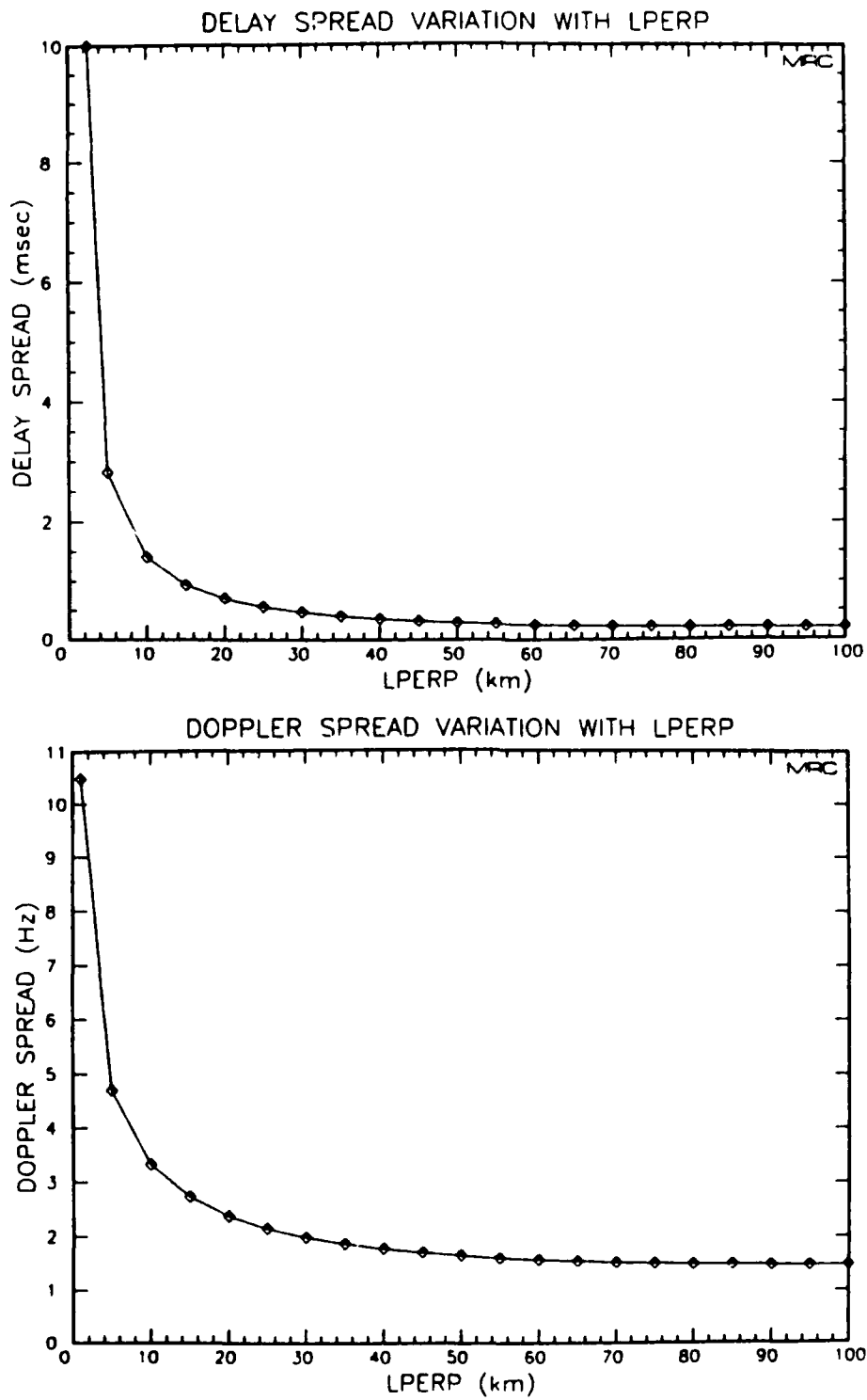


Figure 19. Delay and doppler spread variation with L_{\perp} for the high ray of Figure 3. The remaining parameters are fixed at $SI = 2$, $L_{\parallel} = 100$ km, $\xi = 0.2$, $\epsilon = 0.001$, $v_{\perp} = 50$ m/sec.

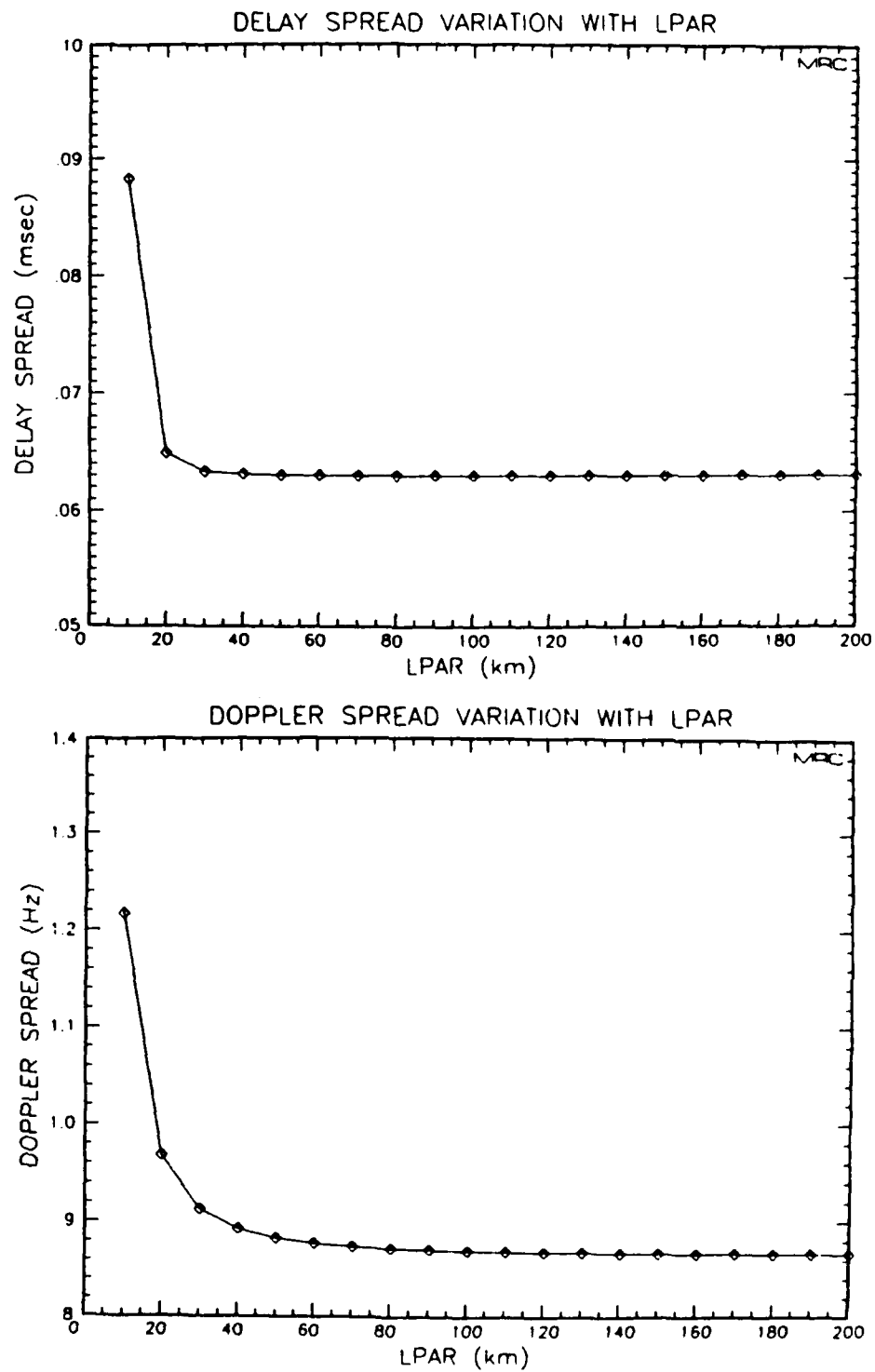


Figure 20. Delay and doppler spread variation with L_{\parallel} for the low ray of Figure 3. The remaining parameters are fixed at $SI = 2$, $L_{\parallel} = 10$ km, $\xi = 0.2$, $\epsilon = 0.001$, $v_{\perp} = 50$ m/sec.

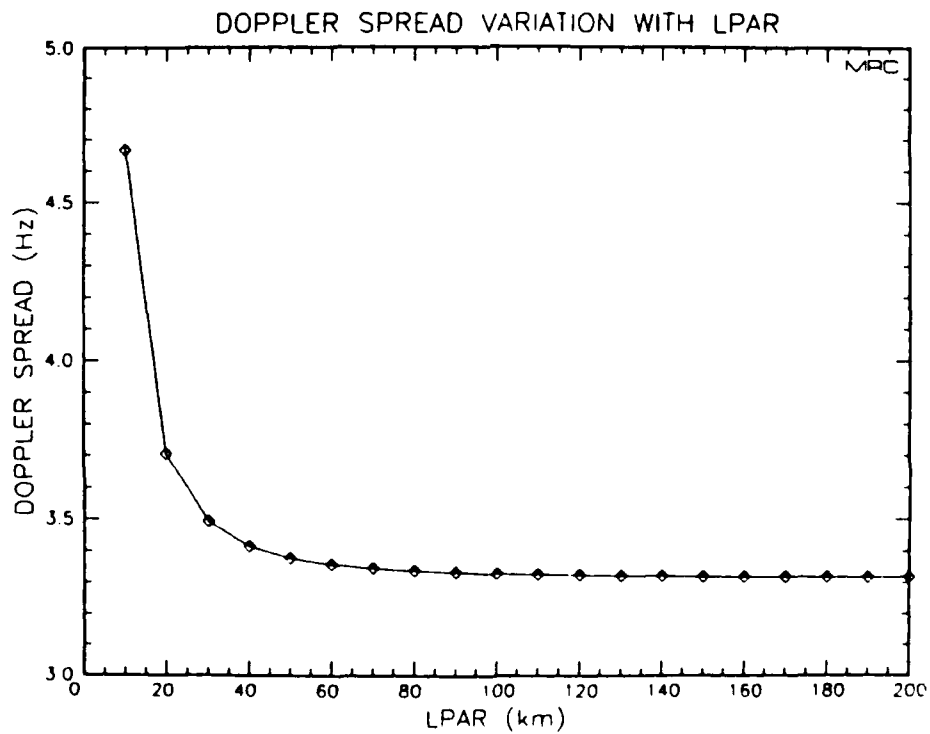
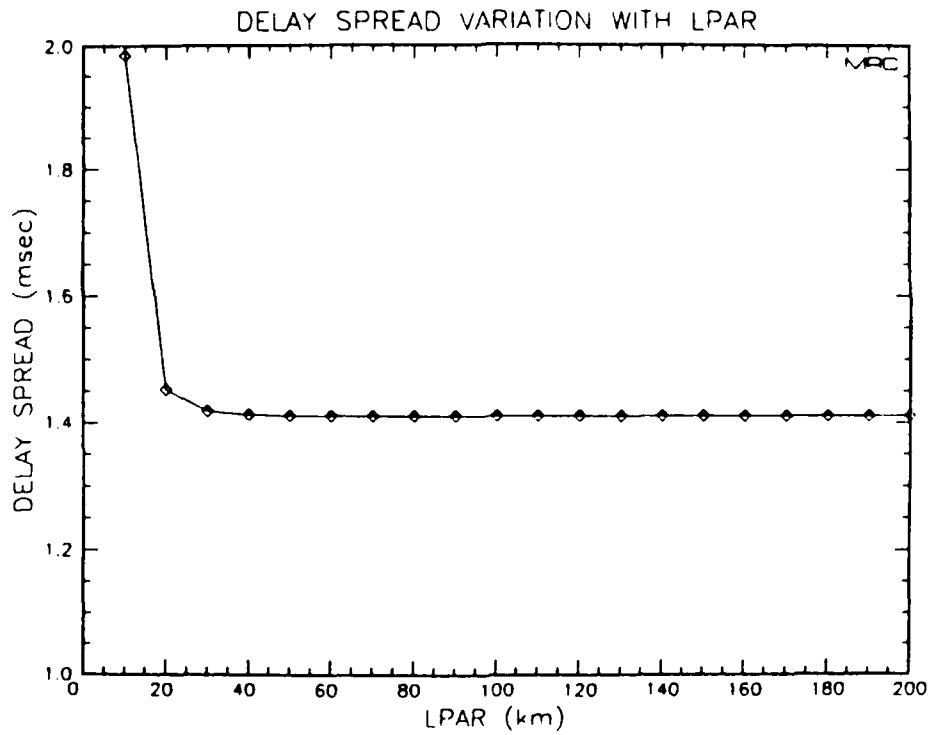


Figure 21. Delay and doppler spread variation with L_{\parallel} for the high ray of Figure 3. The remaining parameters are fixed at $SI = 2$, $L_{\perp} = 10$ km, $\xi = 0.2$, $\epsilon = 0.001$, $v_{\perp} = 50$ m/sec.

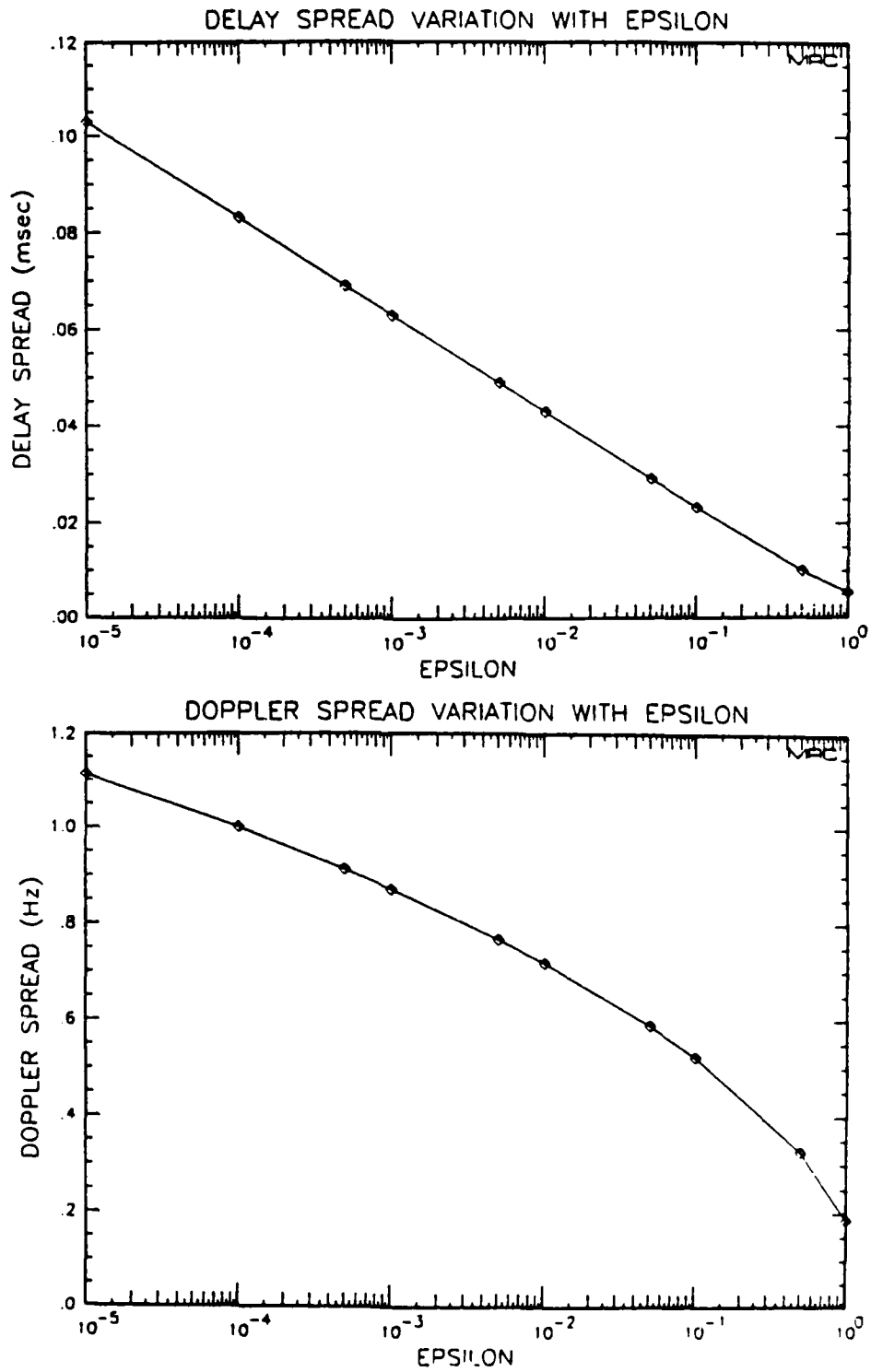


Figure 22. Delay and doppler spread variation with ϵ for the low ray of Figure 3. The remaining parameters are fixed at $S_I = 2$, $L_{\perp} = 10$ km, $L_{\parallel} = 100$ km, $\xi = 0.2$, $v_{\perp} = 50$ m/sec.

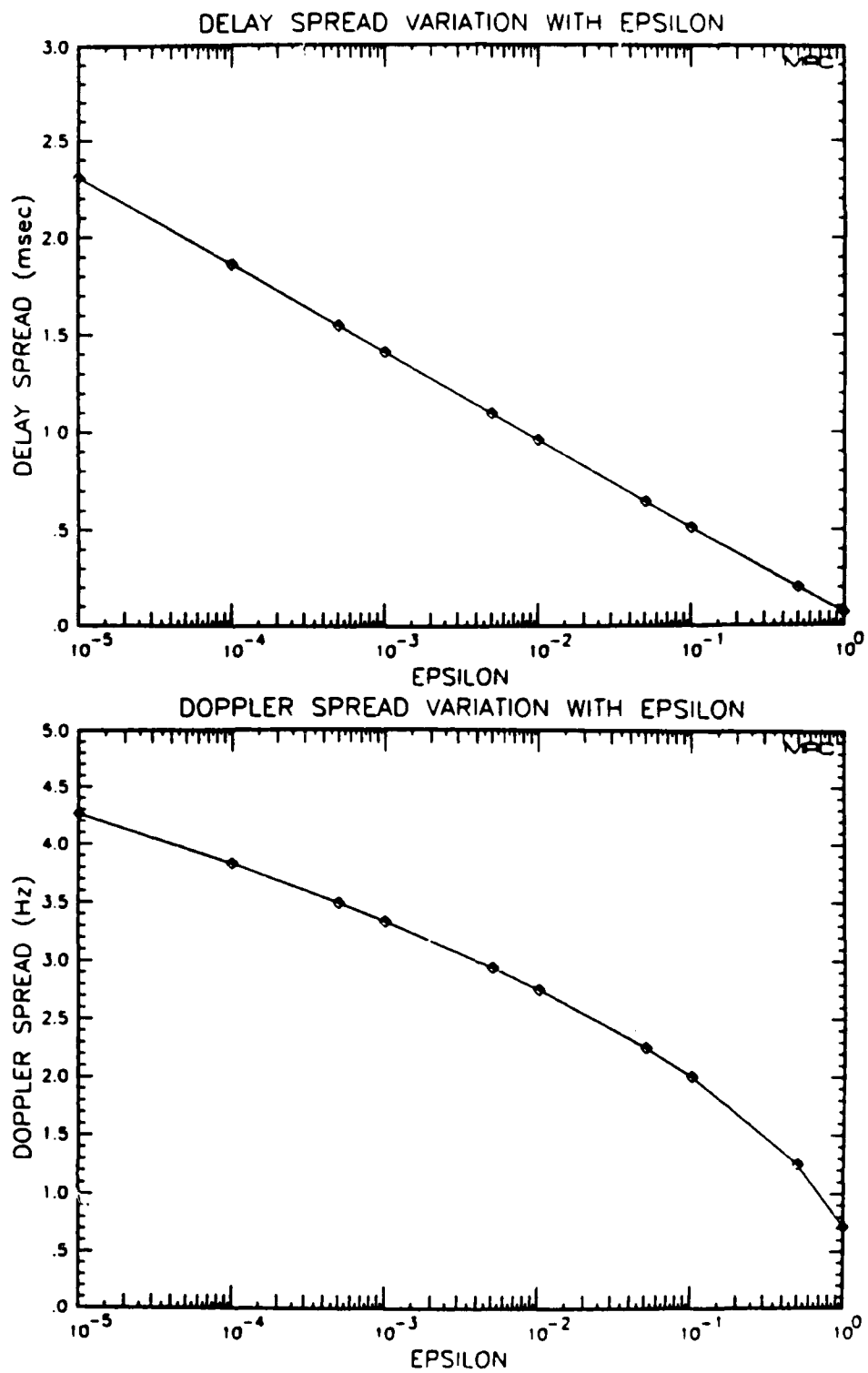


Figure 23. Delay and doppler spread variation with ϵ for the high ray of Figure 3. The remaining parameters are fixed at $SI = 2$, $L_{\perp} = 10$ km, $L_{\parallel} = 100$ km, $\xi = 0.2$, $v_{\perp} = 100$ m/sec.

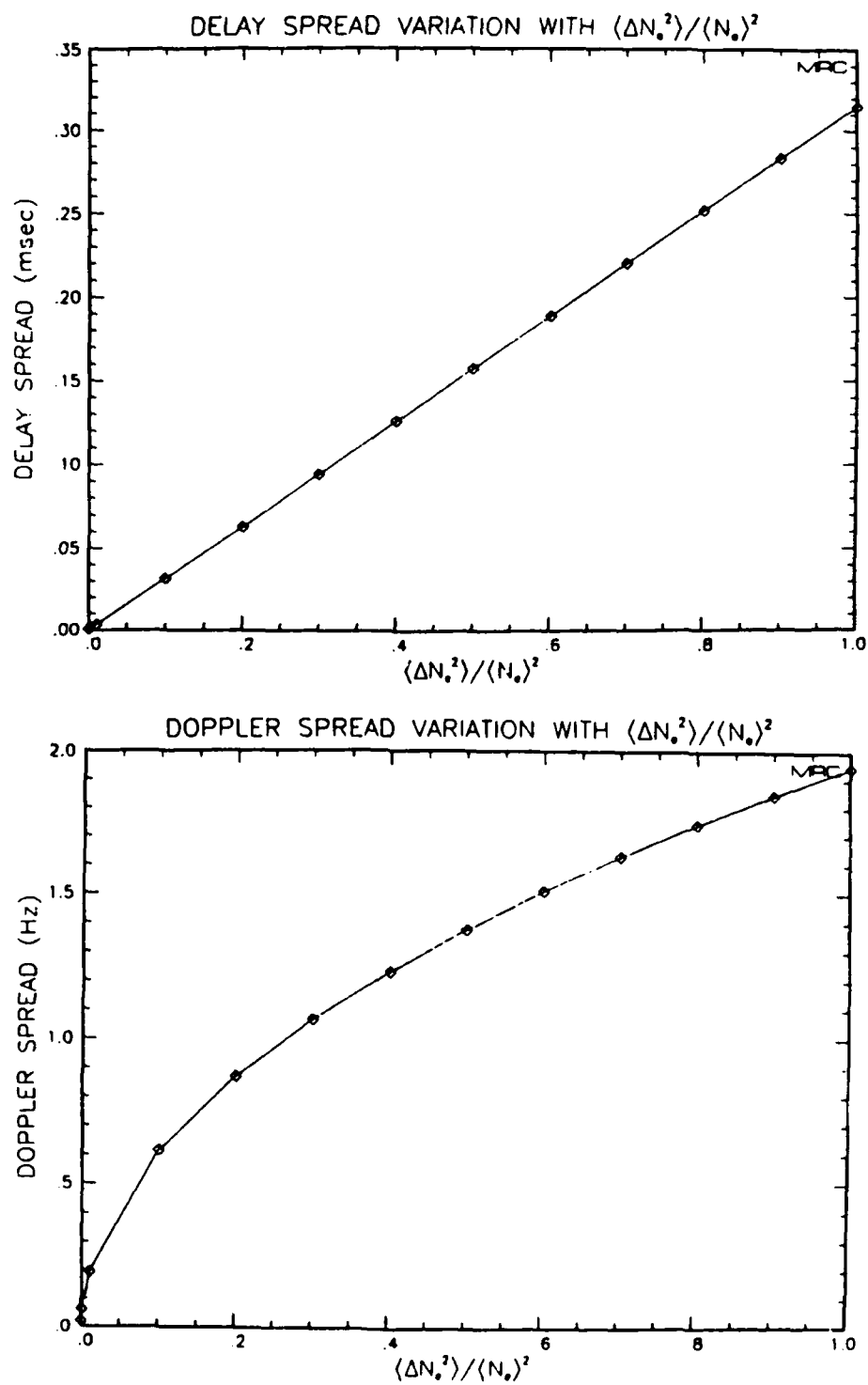


Figure 24. Delay and doppler spread variation with ξ for the low ray of Figure 3. The remaining parameters are fixed at $SI = 2$, $L_{\perp} = 10$ km, $L_{\parallel} = 100$ km, $\epsilon = 0.001$, $v_{\perp} = 50$ m/sec.

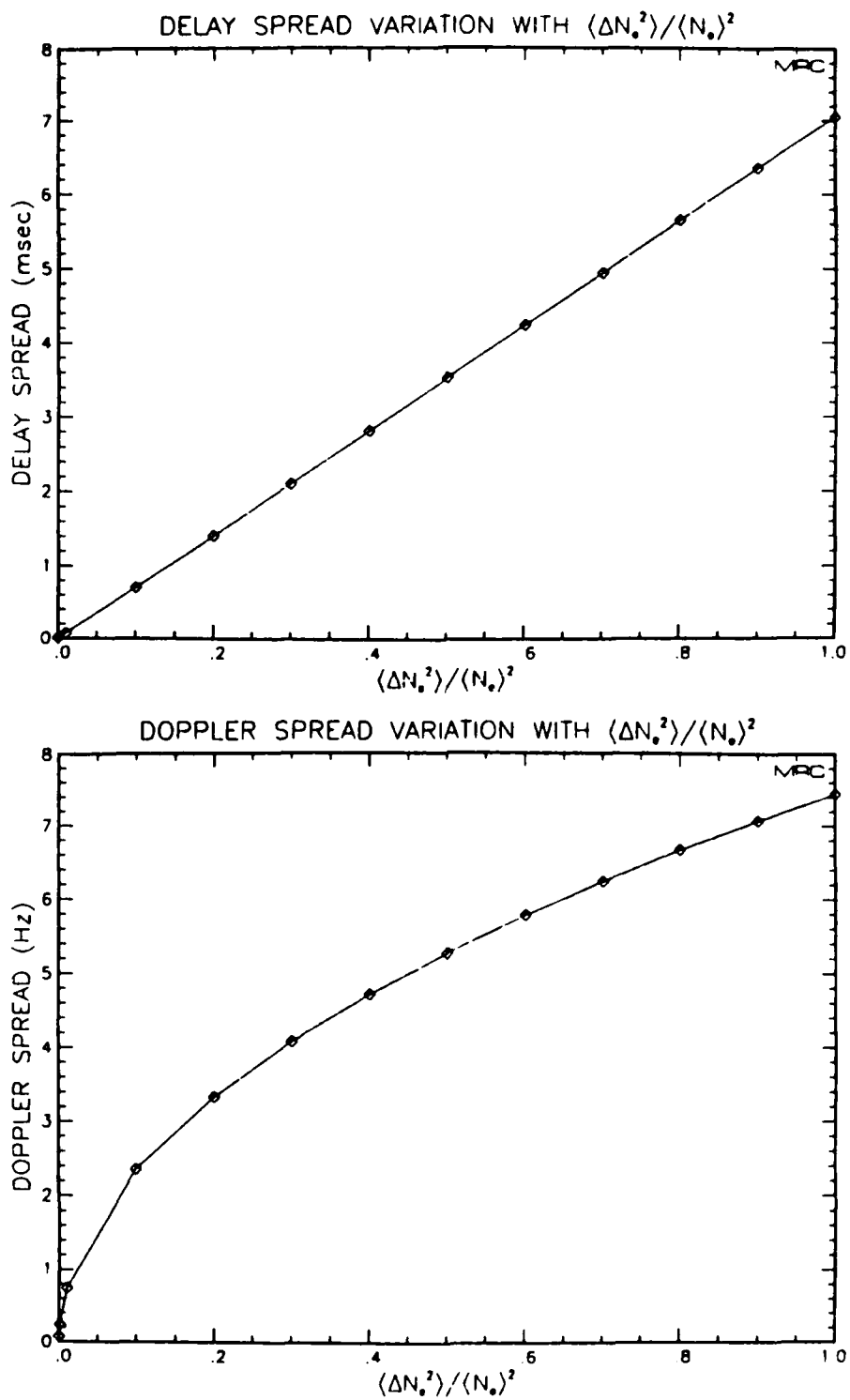


Figure 25. Delay and doppler spread variation with ξ for the high ray of Figure 3. The remaining parameters are fixed at $SI = 2$. $L_{\perp} = 10$ km, $L_{\parallel} = 100$ km, $\epsilon = 0.001$, $v_{\perp} = 50$ m/sec.

$\sigma_d \sim \sqrt{s} \sqrt{\xi} \langle N_e \rangle$ for $n = 2$. The scaling of delay spread can be similarly obtained by examining Eq. (40). While it was not explicitly shown, the Rayleigh phase variance scales as $\sigma_{\phi_R}^2 \sim s \xi \langle N_e \rangle^2$ (i.e. it goes like the integrated phase variance). The second term in Eq. (40) scales as $s^4 \xi^2 \langle N_e \rangle^4$ for $n = 2$. Remembering to take the square root of Eq. (40) to obtain the delay spread, Figures 24 and 25 clearly show that it is this second term which dominates. While these scaling rules change slightly as n becomes less than 2, it is clear that the dependence on ξ is sufficiently slowly varying to be of secondary concern in parameter fitting.

These figures show that the spectral index is substantially the most sensitive parameter in the formulation. Given the uncertainty in our present understanding of an appropriate value for the spectral index, or more correctly, the range of values over which this parameter has been observed to vary, it makes most sense at this stage to vary the spectral index in fitting the HF Channel Probe data while fixing the other parameters to reasonable values. L_1 or ξ might be varied secondarily when comparing data from associated modes.

The scaling rules just obtained, especially the one for delay spread, $\sigma_\tau \sim s^2 \xi \langle N_e \rangle^2$, show that the formulation is very sensitive to the ray path, in particular for the high ray which may have a significant path length near the layer critical frequency. As we saw in Section 2.5, the uncertainty in the ionogram delay measurements can result in large uncertainties in the fitted layer parameters. Hence there is some danger in fitting the scattering function measurements that ray path inaccuracies may be absorbed into the fitted parameters.

SECTION 4 TESTS OF THE SCINTILLATION MODEL

4.1 INTRODUCTION.

In the previous sections we have presented a method for scaling the HF Channel Probe oblique ionograms and have described the DNA scintillation model calculation for delay and doppler spreads. We now test this model against the HF Channel Probe scattering function measurements. Our approach will be to trace rays through the quasi-parabolic ionosphere obtained from an ionogram fit, and, with the scintillation model, calculate delay and doppler widths over these paths. We seek a set of model parameters which reproduce the measured scattering function widths.

This section begins with a description of how delay and doppler spreads are extracted from the data. We then consider initial fits to the low ray data and obtain some insight into how to handle associated low and high ray modes. Finally, we consider fits of these associated modes and discuss the significance of the resulting model parameter values.

4.2 THE DATA.

The fitting methods used in our analysis force us at present to look at each case individually. This makes the analysis sufficiently tedious that it is impossible to examine the whole volume of data supplied by the HF Channel Probe experiment. Hence we have selected six data sets which represent a variety of propagation conditions to analyze in detail.

An example scattering function measurement was shown in Figure 15. This measurement clearly displayed two distinct modes, associated with the low and high rays reflecting from the F-layer. Splitting between ordinary and extraordinary modes is not evident in this example and is only suggested in a few of the cases we have examined, so we confine ourselves to the examination of ordinary waves only (i.e., we ignore the external magnetic field of the earth when calculating ray trajectories, although it will be included in the calculation of stochastic effects).

The shape of the scattering function suggests that it may be well represented by a sum of two bivariate gaussians. Assuming such a functional form for the scattering function provides a convenient way to obtain delay and doppler widths from the measurements. We assume the form,

$$S(\tau, f_d) = P_1 e^{-\{(f_d - \mu_{d1})^2 / v_{d1}^2\}} e^{-\{(\tau - \mu_{\tau1})^2 / (2\sigma_{\tau1}^2)\}} \\ + P_2 e^{-\{(f_d - \mu_{d2})^2 / v_{d2}^2\}} e^{-\{(\tau - \mu_{\tau2})^2 / (2\sigma_{\tau2}^2)\}} , \quad (52)$$

where the subscripts 1 and 2 refer to the low and high ray modes respectively. We fit (least squares) the measured scattering function data to this form to obtain the best fit parameters P_i , μ_{di} , v_{di} , $\mu_{\tau i}$, $\sigma_{\tau i}$. Of these, we are primarily interested in the widths v_{di} and $\sigma_{\tau i}$ which we take to be the measured doppler and delay spreads.

The selected data sets, gaussian fits, and corresponding ionograms are shown in Figures 26 through 37 and Tables 3 through 8. Note that different mesh sizes are used in the fitted scattering function plots compared to the measured scattering function plots (half the frequency resolution and twice the delay resolution). The powers are normalized to a peak power of one. Comparison of the scattering functions with the associated ionograms shows in each case that the modes are properly interpreted as low and high ray F-layer reflections.

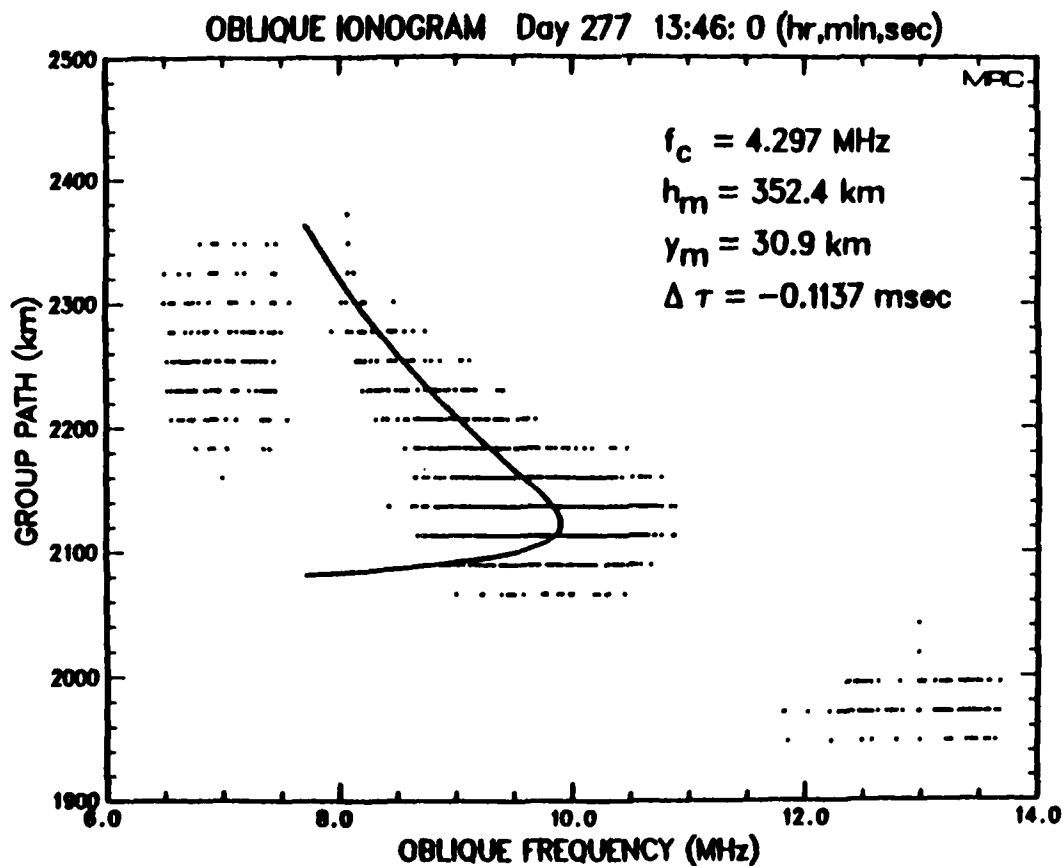
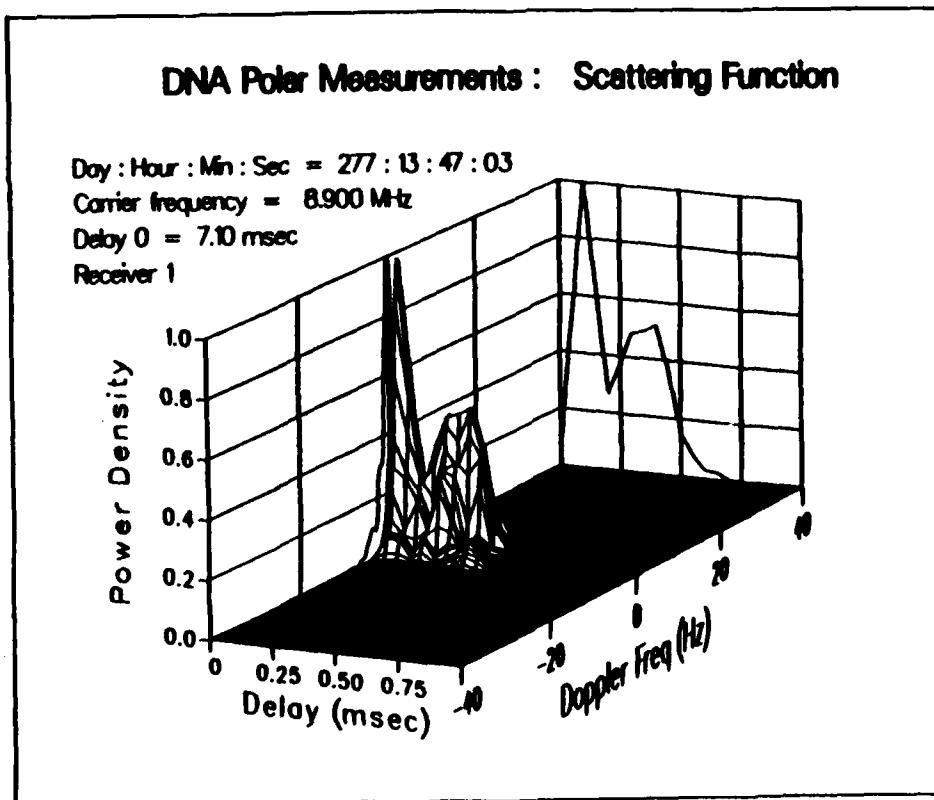


Figure 26. HF Channel Probe scattering function measurement, Oct. 3, 1984, 13:47 GMT (a) and corresponding oblique ionogram (b) including best fit parameters for a quasi-parabolic layer.

Scattering Function Fit

Day : Hour : Min : Sec = 277 : 13 : 47 : 03

Carrier frequency = 8.900 MHz

Delay 0 = 7.10 msec

Receiver 1 FT

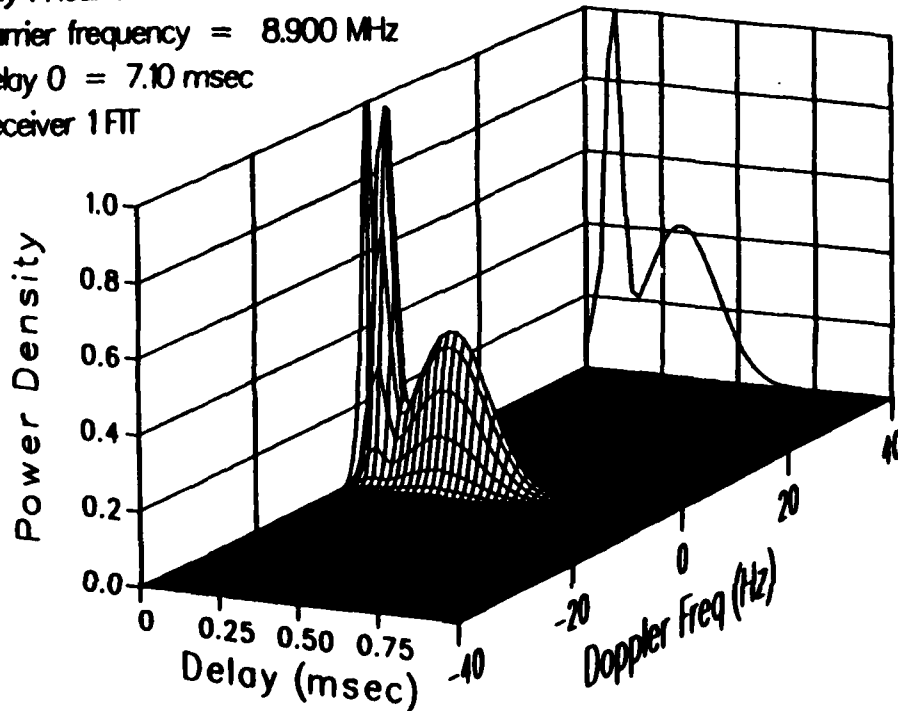


Figure 27. Fit to two bivariate gaussians of the scattering function measurement of Figure 26. Final fit parameters are shown in Table 3.

Table 3. Bivariate gaussian fit parameters for the scattering function of Figure 26, Day 277, 13:47 GMT.

$P_1 = 1.$	$P_2 = 0.4080$
$\mu_{d_1} = -0.4607 \text{ Hz}$	$\mu_{d_2} = -0.8369 \text{ Hz}$
$\nu_{d_1} = 1.336 \text{ Hz}$	$\nu_{d_2} = 1.731 \text{ Hz}$
$\mu_{\tau_1} = 7.166 \text{ msec}$	$\mu_{\tau_2} = 7.388 \text{ msec}$
$\sigma_{\tau_1} = 25.46 \mu\text{sec}$	$\sigma_{\tau_2} = 116.1 \mu\text{sec}$

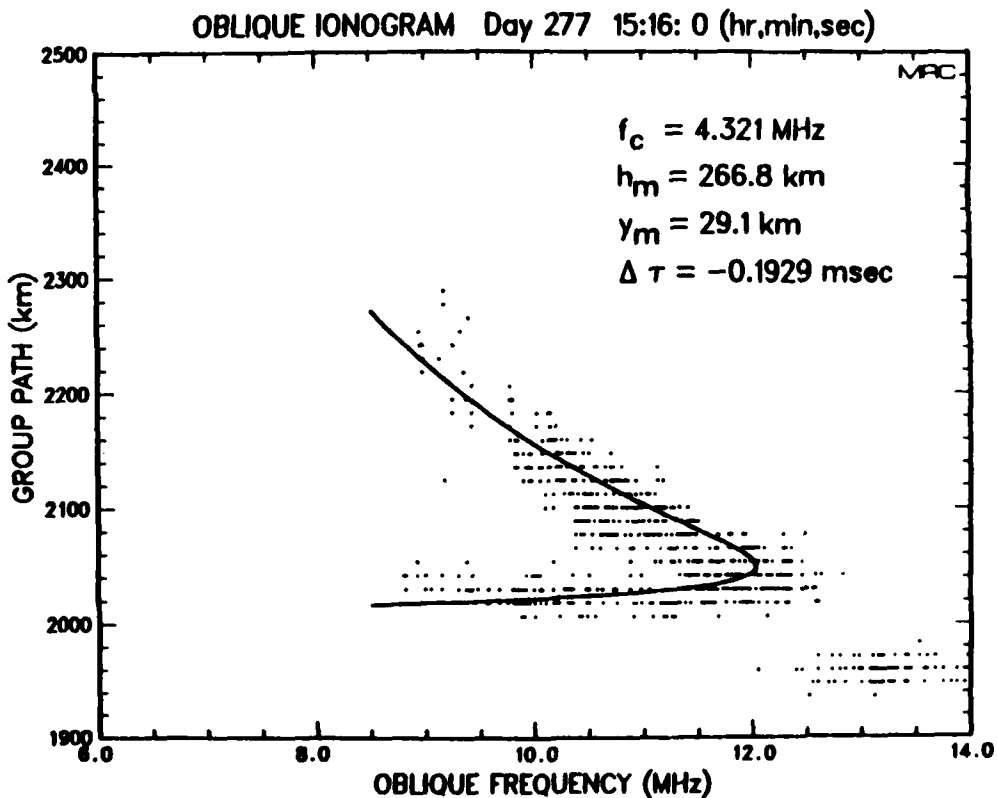
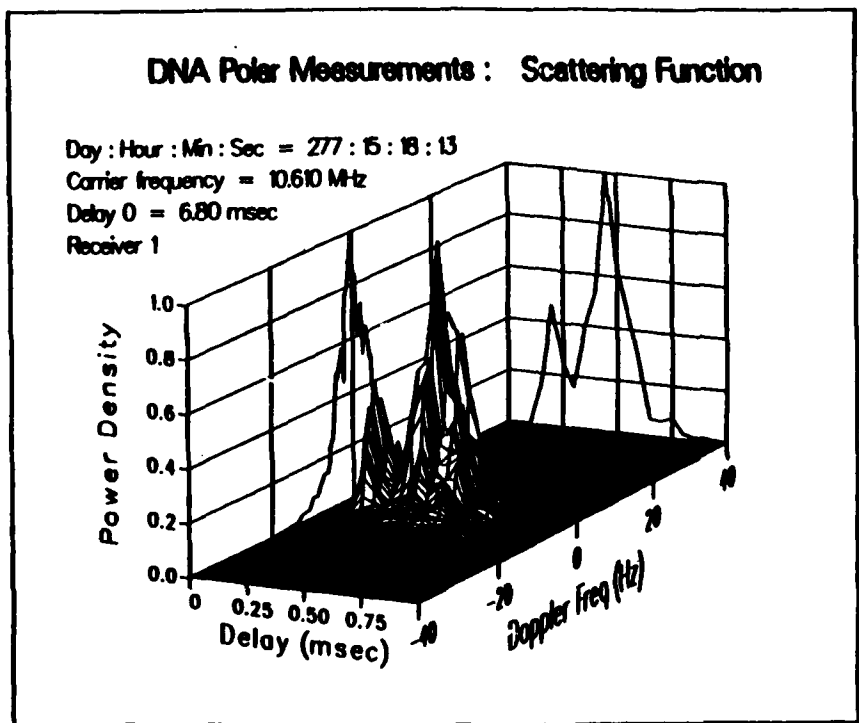


Figure 28. HF Channel Probe scattering function measurement, Oct. 3, 1984, 15:18 GMT (a) and corresponding oblique ionogram (b) including best fit parameters for a quasi-parabolic layer.

Scattering Function Fit

Day : Hour : Min : Sec = 277 : 15 : 18 : 13

Carrier frequency = 10.610 MHz

Delay 0 = 6.80 msec

Receiver 1 FTI

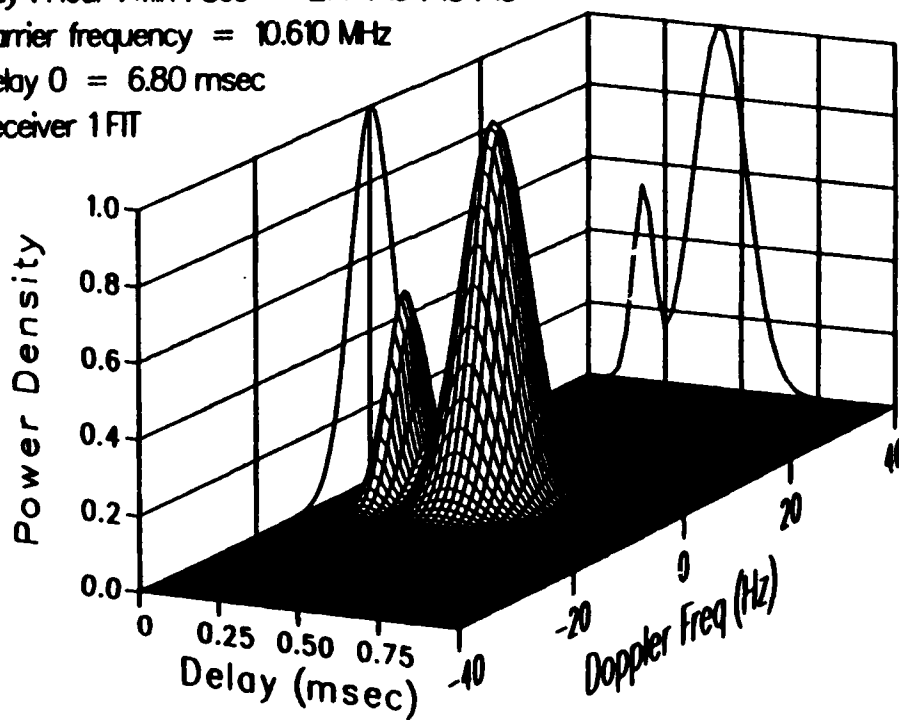


Figure 29. Fit to two bivariate gaussians of the scattering function measurement of Figure 28. Final fit parameters are shown in Table 4.

Table 4. Bivariate gaussian fit parameters for the scattering function of Figure 28, Day 277, 15:18 GMT.

$P_1 = 0.5303$	$P_2 = 1.$
$\mu_{d_1} = -2.037 \text{ Hz}$	$\mu_{d_2} = -0.2155 \text{ Hz}$
$\nu_{d_1} = 4.051 \text{ Hz}$	$\nu_{d_2} = 4.975 \text{ Hz}$
$\mu_{\tau_1} = 6.955 \text{ msec}$	$\mu_{\tau_2} = 7.207 \text{ msec}$
$\sigma_{\tau_1} = 32.92 \text{ } \mu\text{sec}$	$\sigma_{\tau_2} = 85.87 \text{ } \mu\text{sec}$

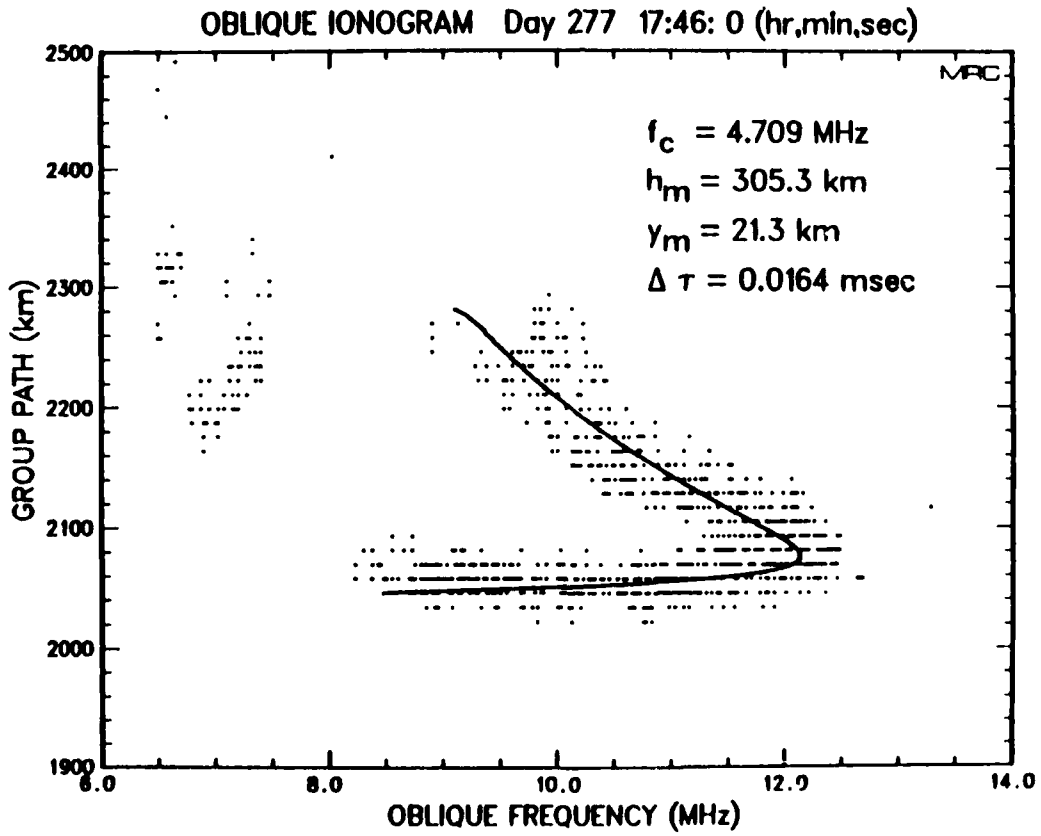
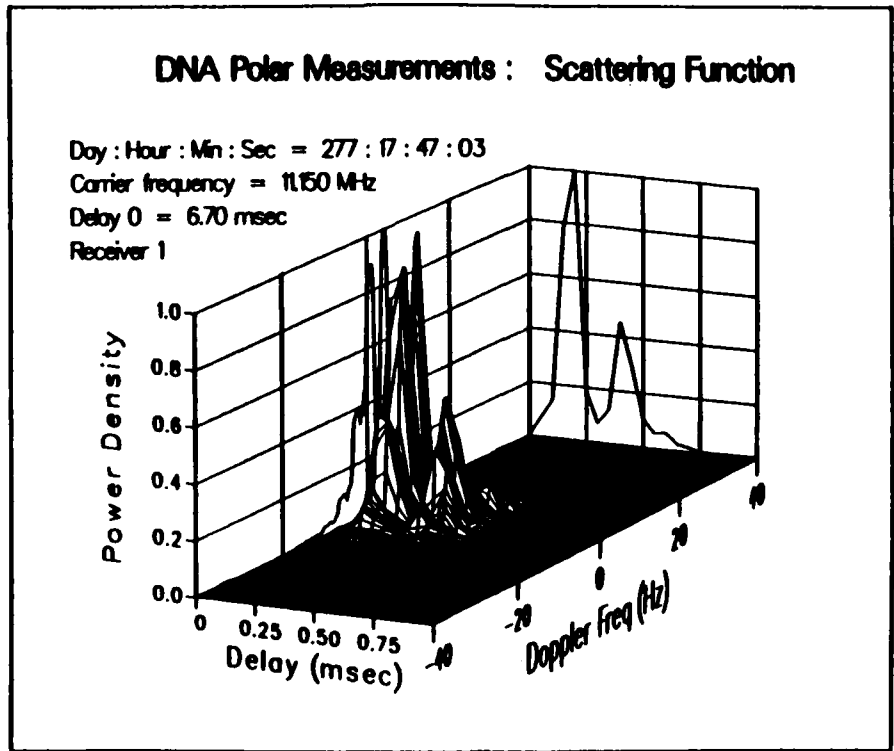


Figure 30. HF Channel Probe scattering function measurement, Oct. 3, 1984, 17:47 GMT (a) and corresponding oblique ionogram (b) including best fit parameters for a quasi-parabolic layer.

Scattering Function Fit

Day : Hour : Min : Sec = 277 : 17 : 47 : 03

Carrier frequency = 11.150 MHz

Delay 0 = 6.70 msec

Receiver 1FIT

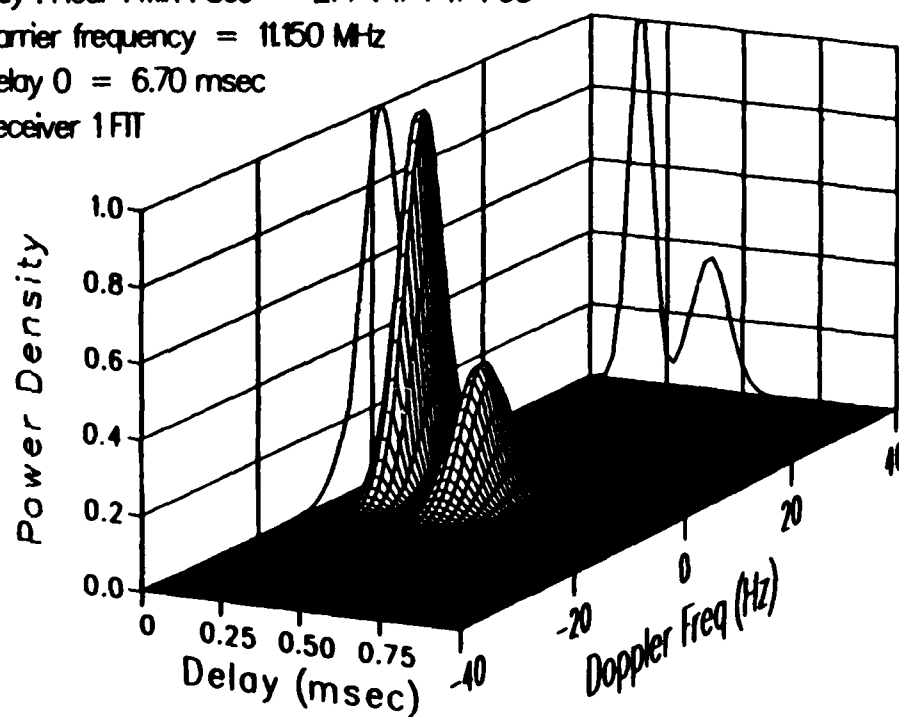


Figure 31. Fit to two bivariate gaussians of the scattering function measurement of Figure 30. Final fit parameters are shown in Table 5.

Table 5. Bivariate gaussian fit parameters for the scattering function of Figure 30, Day 277, 17:47 GMT.

$P_1 = 1.$	$P_2 = 0.3453$
$\mu_{d_1} = 1.063 \text{ Hz}$	$\mu_{d_2} = -0.8755 \text{ Hz}$
$\nu_{d_1} = 4.568 \text{ Hz}$	$\nu_{d_2} = 5.189 \text{ Hz}$
$\mu_{\tau_1} = 6.838 \text{ msec}$	$\mu_{\tau_2} = 7.069 \text{ msec}$
$\sigma_{\tau_1} = 37.04 \text{ } \mu\text{sec}$	$\sigma_{\tau_2} = 60.66 \text{ } \mu\text{sec}$

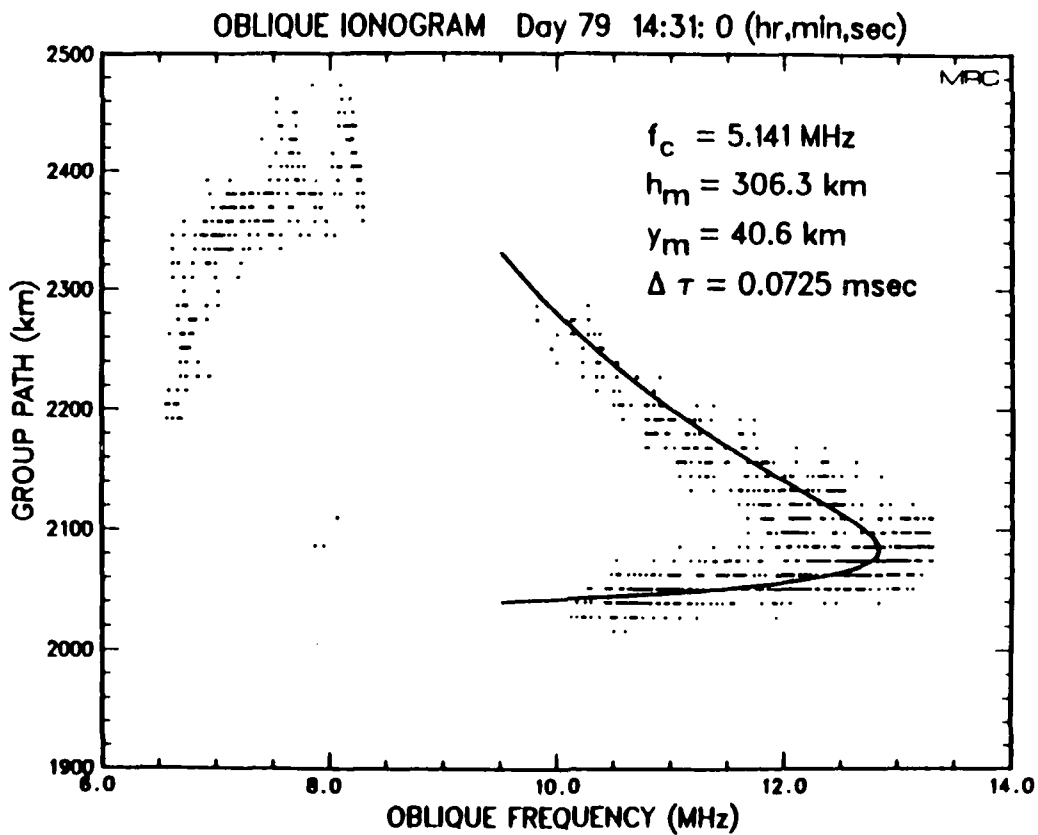
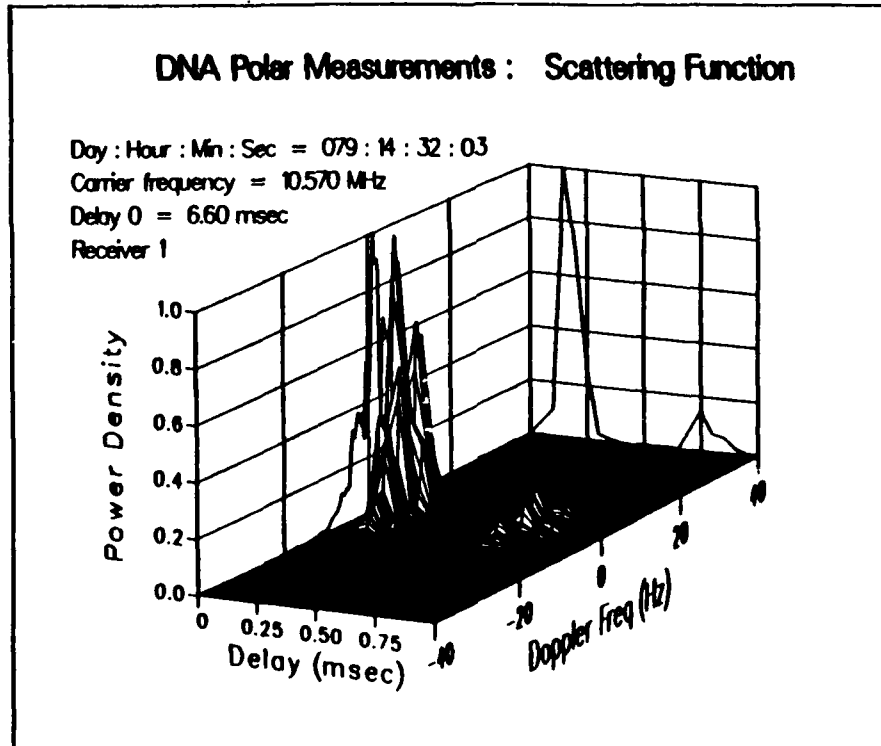


Figure 32. HF Channel Probe scattering function measurement, Mar. 20, 1985, 14:32 GMT (a) and corresponding oblique ionogram (b) including best fit parameters for a quasi-parabolic layer.

Scattering Function Fit

Day : Hour : Min : Sec = 079 : 14 : 32 : 03

Carrier frequency = 10.570 MHz

Delay 0 = 6.60 msec

Receiver 1 FIT

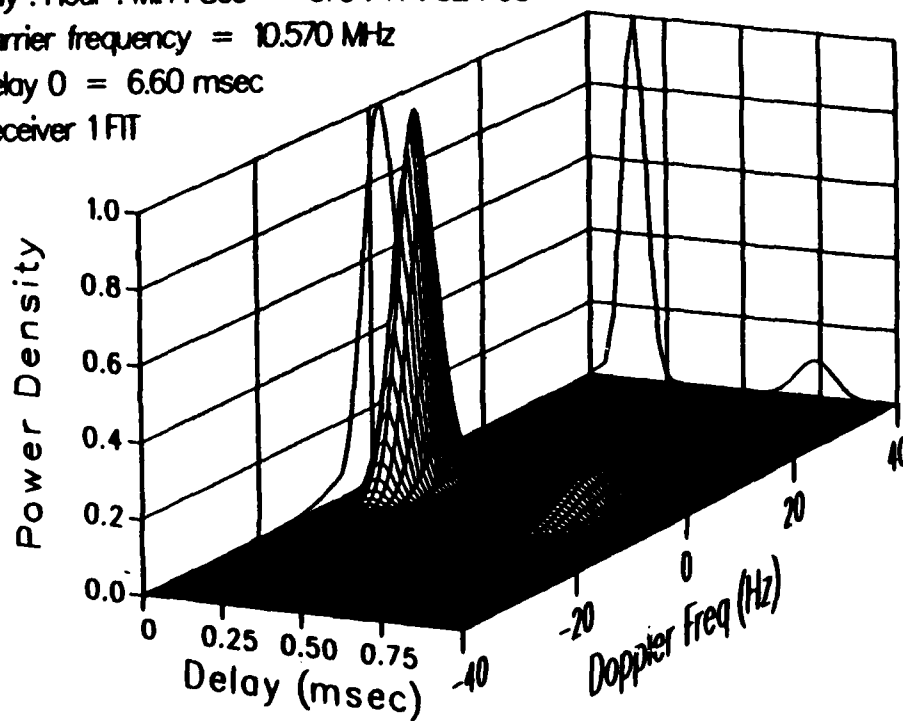


Figure 33. Fit to two bivariate gaussians of the scattering function measurement of Figure 32. Final fit parameters are shown in Table 6.

Table 6. Bivariate gaussian fit parameters for the scattering function of Figure 32, Day 79, 14:32 GMT.

$P_1 = 1.$	$P_2 = 0.09955$
$\mu_{d_1} = 1.147 \text{ Hz}$	$\mu_{d_2} = -0.4527 \text{ Hz}$
$\nu_{d_1} = 4.115 \text{ Hz}$	$\nu_{d_2} = 7.624 \text{ Hz}$
$\mu_{\tau_1} = 6.722 \text{ msec}$	$\mu_{\tau_2} = 7.311 \text{ msec}$
$\sigma_{\tau_1} = 37.37 \text{ } \mu\text{sec}$	$\sigma_{\tau_2} = 58.41 \text{ } \mu\text{sec}$

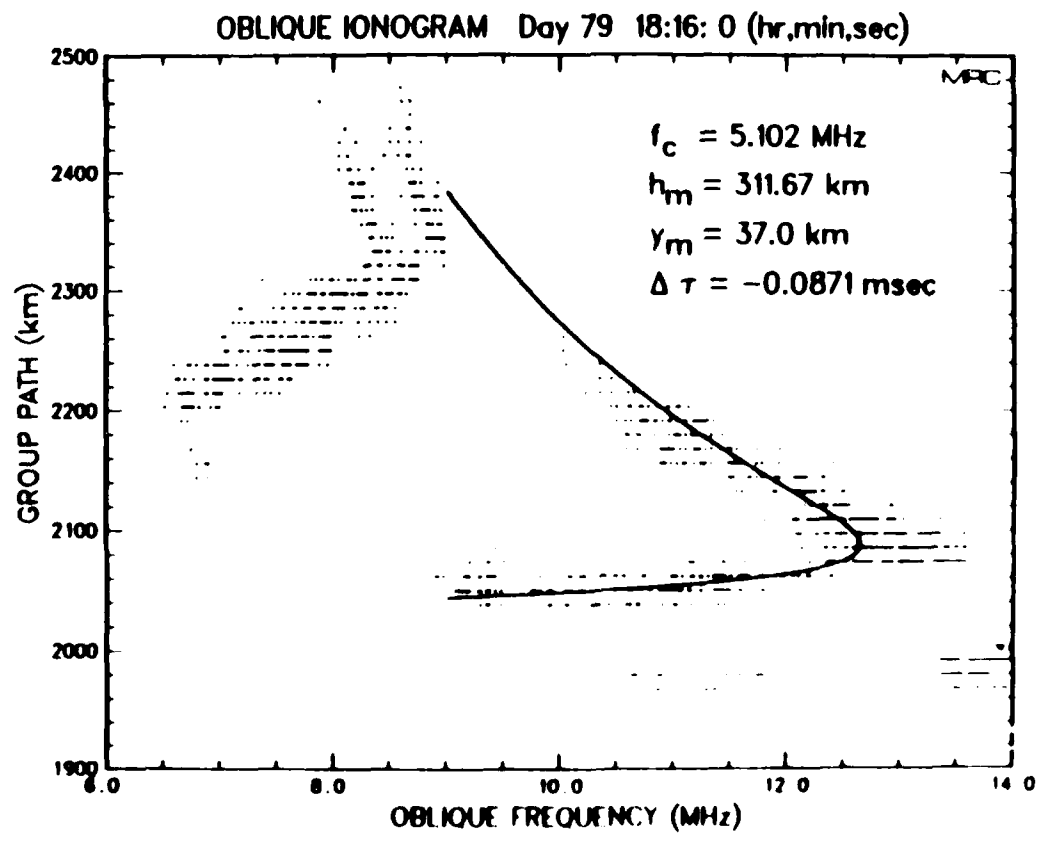
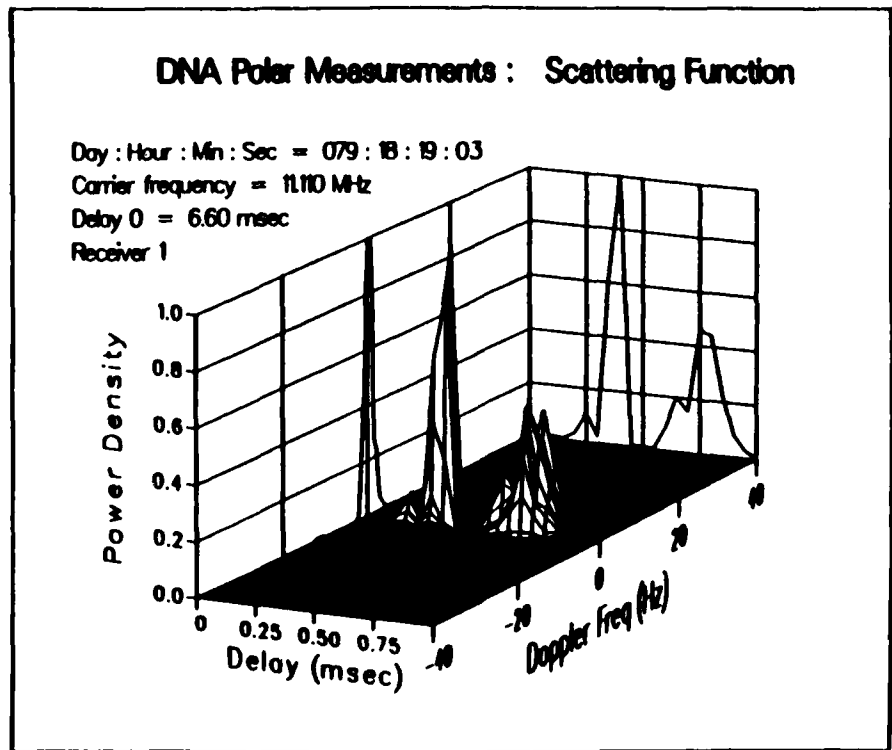


Figure 34. HF Channel Probe scattering function measurement, May 1995, 12:19 GMT. The solid line represents the fit to the data including both fit parameters. The dashed line represents the fit to the data.

Scattering Function Fit

Day : Hour : Min : Sec = 079 : 18 : 19 : 03

Carrier frequency = 11.110 MHz

Delay 0 = 5.60 msec

Receiver 1FTT

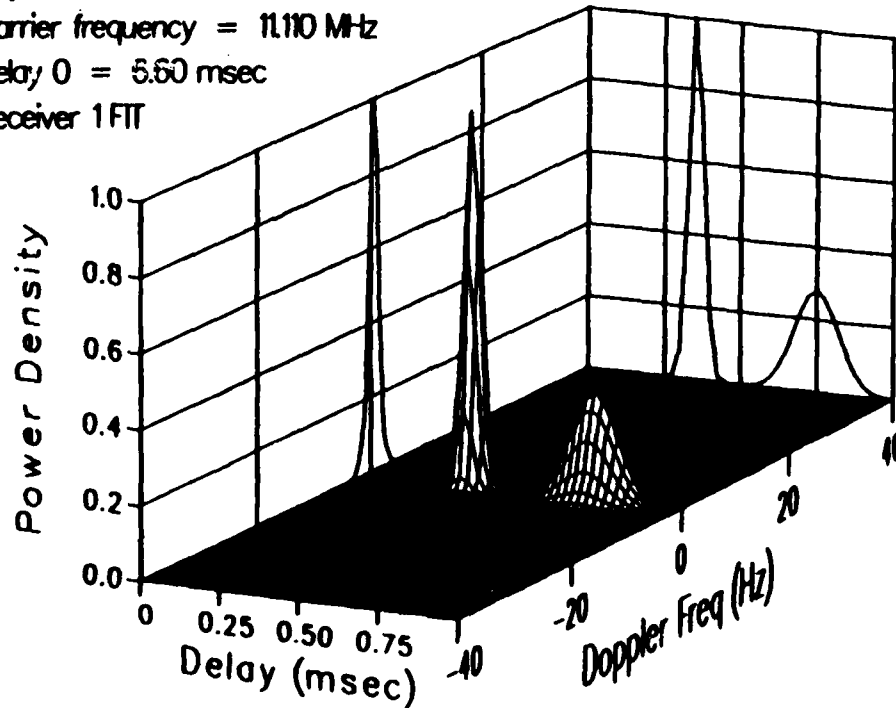


Figure 35. Fit to two bivariate Gaussians of the scattering function measurement of Figure 34. Final fit parameters are shown in Table 7.

Table 7. Bivariate Gaussian fit parameters for the scattering function of Figure 34, Day 79, 18:19 GMT.

P_1 - 1.	P_2 - 0.2701
μ_{d_1} - 0.01025 Hz	μ_{d_2} - -0.09315 Hz
ν_{d_1} - 1.071 Hz	ν_{d_2} - 1.752 Hz
μ_{r_1} - 6.930 msec	μ_{r_2} - 7.325 msec
σ_{r_1} - 24.11 μ sec	σ_{r_2} - 71.26 μ sec

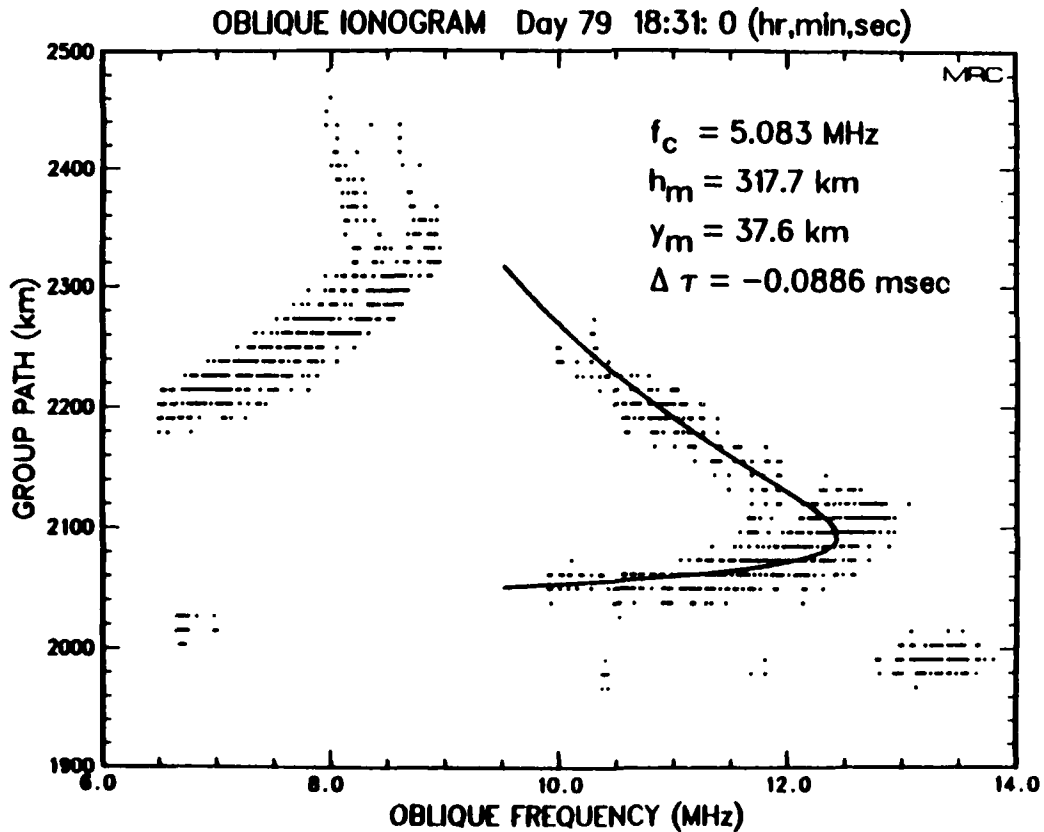
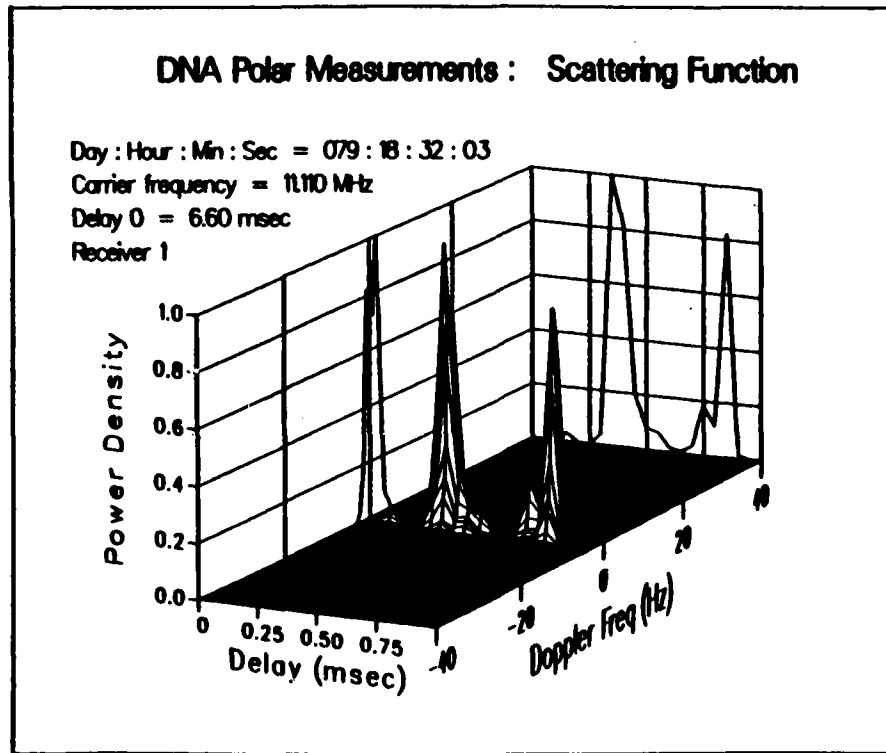


Figure 36. HF Channel Probe scattering function measurement, Mar. 20, 1985, 18:32 GMT (a) and corresponding oblique ionogram (b) including best fit parameters for a quasi-parabolic layer.

Scattering Function Fit

Day : Hour : Min : Sec = . 079 : 18 : 32 : 03

Carrier frequency = 11.110 MHz

Delay 0 = 6.60 msec

Receiver 1FTT

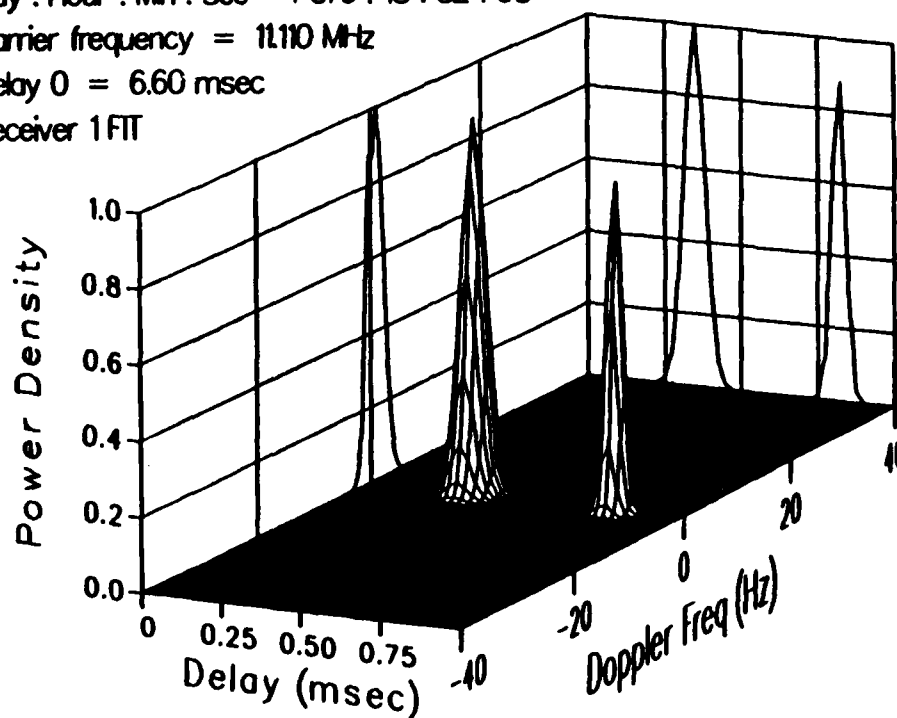


Figure 37. Fit to two bivariate gaussians of the scattering function measurement of Figure 36. Final fit parameters are shown in Table 8.

Table 8. Bivariate gaussian fit parameters for the scattering function of Figure 36, Day 79, 18:32 GMT.

$P_1 = 1.$	$P_2 = 0.9351$
$\mu_{d_1} = 0.5113 \text{ Hz}$	$\nu_{d_1} = -0.6392 \text{ Hz}$
$\nu_{d_1} = 1.778 \text{ Hz}$	$\nu_{d_2} = 1.073 \text{ Hz}$
$\mu_{\tau_1} = 6.924 \text{ msec}$	$\nu_{d_2} = 7.393 \text{ msec}$
$\sigma_{\tau_1} = 33.94 \mu\text{sec}$	$\sigma_{\tau_2} = 21.62 \mu\text{sec}$

4.3 INITIAL FITS.

The DNA scintillation model parameter dependence investigation performed in Section 3.4 suggested that the spectral index is the most sensitive parameter in the model. As a starting point then, we have fit exactly the low ray delay spread by fixing the other parameters to reasonable values and adjusting the spectral index. The doppler spread for the low ray was then exactly fit by adjusting the plasma velocity parameter. These resulting parameters were subsequently used to calculate delay and doppler spreads for the high ray. Comparison of the calculated high ray results to the data will be used to gain insight into a better fitting method for these associated modes to be performed in the next subsection.

We have fixed the structure outer scale sizes to $L_{\perp} = 10$ km, $L_{\parallel} = 100$ km, the ratio of inner to outer structure scale size to $\epsilon = 0.001$, and the fractional electron density variance to $\xi = 0.2$. Table 9 lists the spectral index SI and the plasma velocity v_{\perp} required to fit each of the low ray modes exactly as well as the results obtained when these parameters are applied to the high ray (listed in the table as the ratio [calculated spread]/data). The resulting spectral index values are somewhat large compared to the DNA HILAT results quoted in Section 3.3 (SI ≈ 1.5 to 1.63), but are still well within the observed bounds of the HILAT measurements. The plasma velocities are also very reasonable when compared to electron drift velocity measurements made using the Sondre Stromfjord incoherent-scatter radar, located on the path at about one third of the link distance from the HF Channel Probe transmitter [Basler et al., 1985]. As yet we have been unable to obtain the velocity data from the days of these scattering function measurements (although it exists), but we can say that velocities ranging from zero to 400 m/s (and often much higher) are typically observed.

Table 9. Result of adjusting the spectral index and plasma velocity parameters to fit the low ray modes exactly and subsequent application of these parameters to the high ray modes (listed as the ratio [calculated spread]/data). Fixed parameters are $L_{\perp} = 10$ km, $L_{\parallel} = 100$ km, $\epsilon = 0.001$, $\xi = 0.2$.

<u>Day/time</u>	<u>SI</u>	<u>v_{\perp}(m/s)</u>	<u>High ray spreads</u> (calculated/data)	
			<u>Delay</u>	<u>Doppler</u>
277 13:47	2.422	125.1	5.0	2.82
15:18	1.956	279.3	11.4	3.40
17:47	1.996	271.0	11.1	2.86
79 14:32	1.998	265.9	39.7	3.15
18:19	2.320	84.9	9.4	2.51
18:32	2.226	119.9	34.4	6.11

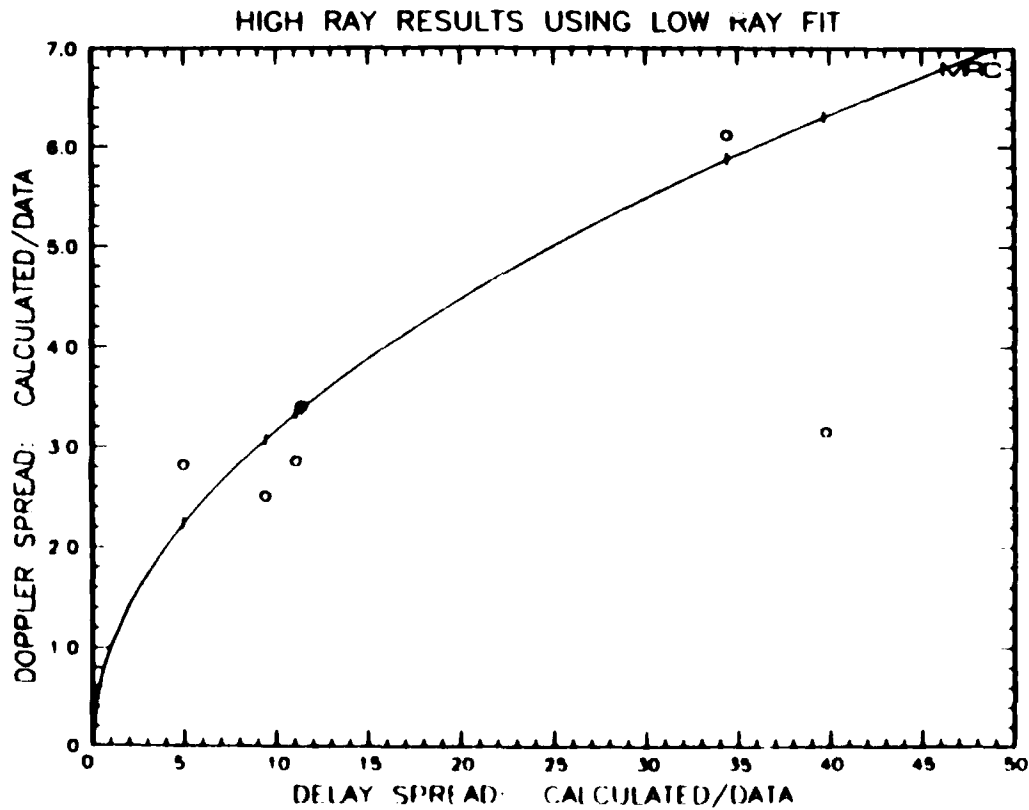


Figure 38. Doppler spread discrepancy versus delay spread discrepancy for the high ray when fit parameters for the low ray are used (circles). The solid curve is the square root of the delay spread discrepancy.

Somewhat disturbing, however, is the observation from Table 9 that delay and doppler spreads calculated for the high ray using these parameters (which fit the low ray quantities exactly) are in every case considerably too large. These results are shown graphically in Figure 38. Here we plot the calculated doppler spread divided by the measured doppler spread as a function of the calculated delay spread divided by the measured delay spread (circles). The solid curve is the square root of the delay axis. We see that in five of the six cases the doppler spread discrepancy is quite close to the square root of the delay spread discrepancy. We note from the analysis of Section 3.4 and the scaling rules obtained there that there is one parameter that scales in precisely this way, the fractional electron density variance, ξ . Figure 38 suggests that allowing this one parameter to vary between the low and high ray trajectories will, to a substantial degree, bring the calculated values of both delay and doppler spread into agreement with the data.

4.4 FITTING ASSOCIATED MODES.

The parameters of the power spectral density of index of refraction variations (PSD, Eq. 37) are considered locally homogeneous quantities [Tatarskii, 1961,1971], which means that they may be slowly varying functions in any spatial direction. In fact, there is no a priori reason to expect any of the model parameters to be essentially constant over any particular ray path, much less over different ray paths. The results of the initial fits described in the previous subsection suggest that to get agreement between model calculations and measured data at least one of the parameters will have to be considered variable. We have suggested that the fractional electron density variance ξ may be an appropriate choice, although one might do as well by varying the spectral index or L_1 (since one can argue that the few points in Figure 38 may be fit with any number of curves). Since our model ionosphere is spherically stratified, the

vertical direction is the only direction in which such variations can be justified in the model. However, the peak altitudes for the low and high ray trajectories differ by only 10 to 25 km in the cases we are examining. These distances are a fraction of the parallel outer scale size, which is the appropriate scale size to consider for vertical variations since the magnetic dip is so high in the polar region. The spectral index should be only slowly varying over distances defined by the outer scale size in that direction for the formalism to be valid, and the same is true about the scale sizes themselves. The expression assumed for electron density variances (Eq. 39), on the other hand, is a low order approximation designed to give a rough order of magnitude account of the layer as a whole. It should not be expected to hold in a detailed fashion over different modes. A more accurate model for these variances may be expected to include some spatial dependence in ξ (perhaps scaling as the gradient of the mean electron density).

As a first cut at introducing a spatially dependent ξ , we consider separate, but constant, values for the high and low rays. This should be roughly equivalent to using a smoothly varying ξ since each ray path within the layer can be well represented by a constant altitude segment (see e.g., Figure 3). All other parameters will be considered constant over the entire layer. Simultaneously fitting associated low and high ray modes allows four parameters to be varied since there are four data points (two delay spreads and two doppler spreads). We choose to fit the spectral index, plasma velocity, and the fractional electron density variances ξ_1 and ξ_2 (low and high rays respectively).

The results of these fits are shown in Table 10. Fractional electron density variances for the high ray modes overall are an order of magnitude smaller than those for the low ray. This, though, corresponds to only a factor of three or four in the root mean square quantity σ_{N_e}/N_e . The plasma velocities are little changed from the values obtained

Table 10. Results of a four parameter simultaneous fit of the low and high ray modes. Fit parameters are the spectral index SI, plasma velocity v_{\perp} , and the fractional electron density variance for the low and high rays, ξ_1 and ξ_2 . Fixed parameters are $L_{\perp} = 10$ km, $L_{\parallel} = 100$ km, $\epsilon = 0.001$.

<u>Day/time</u>	<u>Parameters</u>	<u>Data</u>	<u>Fit</u>	<u>% error</u>
277 1347	SI = 1.652	$\nu_{d_1} = 1.336$ Hz	1.223 Hz	-8.46
	$v_{\perp} = 105.8$ m/s	$\sigma_{\tau_1} = 25.46$ μ sec	29.17 μ sec	14.57
	$\xi_1 = 0.03612$	$\nu_{d_2} = 1.731$ Hz	1.806 Hz	4.33
	$\xi_2 = 0.00514$	$\sigma_{\tau_2} = 116.1$ μ sec	110.4 μ sec	-4.91
277 1518	SI = 1.605	$\nu_{d_1} = 4.051$ Hz	4.039 Hz	-0.30
	$v_{\perp} = 277.7$ m/s	$\sigma_{\tau_1} = 32.92$ μ sec	32.98 μ sec	0.18
	$\xi_1 = 0.06882$	$\nu_{d_2} = 4.975$ Hz	4.976 Hz	0.02
	$\xi_2 = 0.00588$	$\sigma_{\tau_2} = 85.87$ μ sec	85.86 μ sec	-0.01
277 1747	SI = 1.609	$\nu_{d_1} = 4.568$ Hz	4.621 Hz	1.16
	$v_{\perp} = 274.4$ m/s	$\sigma_{\tau_1} = 37.04$ μ sec	36.80 μ sec	-0.65
	$\xi_1 = 0.05926$	$\nu_{d_2} = 5.189$ Hz	4.588 Hz	-11.58
	$\xi_2 = 0.00557$	$\sigma_{\tau_2} = 60.66$ μ sec	62.78 μ sec	3.49
79 1432	SI = 1.616	$\nu_{d_1} = 4.115$ Hz	4.149 Hz	0.83
	$v_{\perp} = 268.0$ m/s	$\sigma_{\tau_1} = 37.37$ μ sec	37.26 μ sec	-0.29
	$\xi_1 = 0.06294$	$\nu_{d_2} = 7.624$ Hz	4.061 Hz	-46.73
	$\xi_2 = 0.00180$	$\sigma_{\tau_2} = 58.41$ μ sec	65.45 μ sec	12.05
79 1819	SI = 1.659	$\nu_{d_1} = 1.071$ Hz	1.102 Hz	2.89
	$v_{\perp} = 90.03$ m/s	$\sigma_{\tau_1} = 24.11$ μ sec	22.27 μ sec	-7.63
	$\xi_1 = 0.03435$	$\nu_{d_2} = 1.752$ Hz	1.543 Hz	-11.93
	$\xi_2 = 0.00358$	$\sigma_{\tau_2} = 71.26$ μ sec	73.72 μ sec	3.45
79 1832	SI = 1.703	$\nu_{d_1} = 1.778$ Hz	1.768 Hz	-0.56
	$v_{\perp} = 118.2$ m/s	$\sigma_{\tau_1} = 33.94$ μ sec	34.18 μ sec	0.71
	$\xi_1 = 0.04845$	$\nu_{d_2} = 1.073$ Hz	1.090 Hz	1.58
	$\xi_2 = 0.00157$	$\sigma_{\tau_2} = 21.62$ μ sec	21.20 μ sec	-1.94

in our initial fits of the previous subsection. The spectral index values, however, have changed significantly and are now very close to the mean values inferred from the DNA HILAT measurements. It is gratifying to see that the freedom introduced by making ξ a fit parameter has worked in such a way as to move the spectral index in this direction.

SECTION 5 CONCLUSIONS

We have tested the DNA scintillation model calculations of delay width and doppler spread against the HF Channel Probe measurements of these quantities for the case of high frequency waves propagated through the naturally occurring ionization structure of the polar region. Our analysis has required the scaling of oblique ionograms taken over the channel probe link in order that a model ionosphere could be constructed through which rays could be numerically traced and the model calculations performed. Measured delay widths and doppler spreads were extracted from the data by fitting the measured scattering functions to two bivariate gaussians corresponding to the low and high ray modes of reflection from the F-layer. We attempted to reproduce these observed widths by varying the parameters of the DNA scintillation model in a fit of the data. Initially we fit the low ray modes exactly by varying the spectral index and plasma velocity parameters, fixing the other model parameters to nominal values. When these resulting parameters were applied to the high ray modes, predicted delay widths and doppler spreads were consistently too large. It was observed that in all but one case these spreads could be brought back into substantial agreement with the data by allowing one parameter, the fractional electron density variance $\xi = \langle \Delta N_e^2 \rangle / \langle N_e \rangle^2$, to take on different values for the high and low rays. This result was assumed to be an approximation to a single spatially dependent ξ . When the high and low ray modes were simultaneously fit by varying the spectral index, plasma velocity, and fractional electron densities for the high and low rays, the results were found to be in good agreement with the data. Furthermore, the resulting spectral indices were very near those inferred from the DNA HILAT measurements carried out in the same region.

We have scaled the oblique ionograms of the HF channel Probe by fitting them directly to the delays produced by a quasi-parabolic layer. This method avoids the approximate step of transforming the oblique ionogram to its vertical equivalent. The three parameters of the quasi-parabolic layer; the critical frequency, height of layer maximum, and layer semi-thickness were supplemented with a fourth parameter, an absolute delay shift of the ionogram data. This was done to account for a 200 usec uncertainty in the absolute delay measurements of the HF Channel probe. We found that fits to the layer obtained by including this fourth parameter resulted in better positioning of the E-layer trace when that was visible in the data. Still, these delay uncertainties are a troublesome point in our analysis because of the sensitivity of the DNA scintillation model calculations to ray path and plasma frequency. For instance, the success attained by considering variable fractional electron density variances could conceivably be explained by some consistent problem with our model ionosphere and the subsequent high rays obtained from it. In future campaigns of the HF Channel Probe, this delay uncertainty will be reduced by an order of magnitude, so this question should be answered by future analysis of this new data.

Our investigation of the parameter dependence of the DNA scintillation model showed that of the six model parameters, the spectral index is substantially the most sensitive. Order of magnitude changes of the calculated spreads occurred as the spectral index varied over the range of values inferred from the DNA HILAT measurements. The model showed less sensitivity to the other parameters. The perpendicular structure outer scale size L_{\perp} , for instance, produced variations in delay and doppler spreads of less than a factor of two when ranged over reasonable values. The plasma velocity parameter only enters the doppler spread calculation and has a linear dependence. The delay spread was shown to depend on the fractional electron density variance ξ in a nearly linear

fashion. The doppler spread scaled essentially as the square root of this parameter. The remaining parameters, the parallel structure outer scale size L_{\parallel} and the ratio of inner to outer structure scale size ϵ , were shown to have little effect on the calculated spreads for any reasonable range of values.

Our initial fit of the low ray spreads by varying only the spectral index and plasma velocity and the subsequent application of these parameters to the high ray yielded results that, even though the high ray spreads were consistently too large, were accurate to an order of magnitude or so. This provides some validity to the scintillation model as a predictive tool for highly oblique paths at HF. By fixing most of the model parameters to nominal values and varying the spectral index over a sensible range, say $SI \approx 1.5$ to 2.5 , expected delay spread bounds can be reasonably estimated, especially for low ray modes which are the predominant modes of interest for HF communication.

Interpreting the good agreement with the data obtained in our four parameter fit summarized in Table 10 is more speculative. As we have already remarked, agreement might also have been obtained by altering the layer parameters to vary the high ray path or by choosing to make the spectral index or L_{\perp} spatially dependent. It is important to note, however, that by making this single parameter ξ effectively spatially dependent, both the calculated high ray delay and doppler spread were reconciled to the data. Also, freeing up ξ as a fit parameter resulted in fit spectral indices which are very close to the values of SI obtained. As yet we have no theoretical justification for why the electron density variances should be relatively small for the high ray. As a rough test where we examined the electron density profiles for the low and high rays for each case, we found that the electron density gradient at the magnitude of the gradient of the electron density profile for the high ray

six data sets could be explained. Theoretical work and further examination of the data is obviously required to substantiate any of these speculations.

The DNA scintillation model has been shown to be capable of reproducing the spreads in delay and doppler observed by the HF Channel Probe in the polar region for quite reasonable values of the model parameters. It must be born in mind that these tests were for highly oblique HF propagation paths only (i.e., launch elevation angles less than twenty degrees or so), and no test of the model has been made in situations where the local plasma frequency of the ionosphere is close to the wave carrier frequency, as would be the case in nearly vertical paths. The model, however, showed no gross failure when applied to oblique HF propagation.

SECTION 6 LIST OF REFERENCES

Basler, R. P., P. B. Bently, G. H. Price, C. L. Rino, and D. K. Rust, "HF Channel Probe," Final Technical Report, Contract DNA-001-83-C-0325, SRI International, Menlo Park, CA (in review July 1985).

Basler, R. P. and T. D. Scott, "Ionospheric Structure from Oblique-Backscatter Soundings", Radio Science, Vol. 8, No. 5, pp. 425-429 (May 1973).

Bello, P. A., "Characterization of Randomly Time-Variant Linear Channels," IEEE Trans. Commun. Syst., CS11, 360 (1963).

Budden, K. G., Radio Waves in the Ionosphere, Cambridge University Press, (1961).

Croft, T. and H. Hoogasian, "Exact Ray Calculations in a Quasi-Parabolic Ionosphere With No Magnetic Field," Radio Science, Vol. 3, No. 1, pp. 69-74 (January 1968).

Davies, K., Ionospheric Radio Propagation, National Bureau of Standards Monograph 80 (1965).

Jones, R. M., and J. J. Stephenson, A Versatile Three-Dimensional Ray Tracing Computer Program for Radio Waves in the Ionosphere, U.S. Dept. of Commerce, Office of Telecommunications, OT Report 75-76 (October 1975).

Kelley, M. C., J. F. Vickrey, C. W. Carlson, and R. Torbert, "On the Origin and Spatial Extent of High-Latitude F Region Irregularities," J. Geophys. Res., Vol. 87, No. A6, pp. 4469-4475 (June 1982).

Reilly, M. H. , "Ionospheric True Height Profiles from Oblique Ionograms," Radio Science, Vol. 20, No. 3, pp. 280-286, (May-June 1985).

Rino, C. L., "On the Application of Phase Screen Models to the Interpretation of Ionospheric Scintillation Data," Radio Science, Vol. 17, No. 4, pp. 855-867 (July-August 1982).

Smith, N., "The Relation of Radio Skywave Transmission to Ionosphere Measurements," Proc. IRE, Vol. 27, pp. 332-347 (1939).

LIST OF REFERENCES (continued)

Tatarskii, V. I., Wave Propagation in a Turbulent Medium, Dover Publications, Inc., New York (1961).

Tatarskii, V. I., The Effects of the Turbulent Atmosphere on Wave Propagation, translated by the Israel Program for Scientific Translations, National Technical Information Service, U.S. Department of Commerce (1971).

Wittwer, L. A., "Radio Wave Propagation in Structured Ionization for Satellite Applications," DNA 5304D, Defense Nuclear Agency, Washington, DC (1979).

Wittwer, L. A., "Radio Wave Propagation in Structured Ionization for Satellite Applications II," DNA-IR-82-02, Defense Nuclear Agency, Washington, DC (1982).

Wortman, W. R. and R. W. Kilb, "The Relation Between PSD's and Striation Properties," (unpublished).

DISTRIBUTION LIST

DEPARTMENT OF DEFENSE

ASST SECY OF DEF CMD CONT COMM & INTEL
ATTN: DASD(I)

ASSISTANT TO THE SECRETARY OF DEFENSE
ATTN: EXECUTIVE ASSISTANT

BOSTON COLLEGE, THE TRUSTEES OF
2 CYS ATTN: CHAIRMAN DEPT OF CHEMISTRY
2 CYS ATTN: CHAIRMAN DEPT OF PHYSICS

DEFENSE ADVANCED RSCH PROJ AGENCY
ATTN: GSD R ALEWINE
ATTN: T TETHER

DEFENSE COMMUNICATIONS AGENCY
ATTN: A200

DEFENSE COMMUNICATIONS ENGINEER CENTER
ATTN: CODE R123 TECH LIB

DEFENSE INTELLIGENCE AGENCY
ATTN: RTS-2B

DEFENSE NUCLEAR AGENCY
3 CYS ATTN: RAAE
ATTN: RAAE K SCHWARTZ
ATTN: RAAE P CROWLEY
ATTN: RAAE P LUNN
ATTN: STNA
4 CYS ATTN: STTI-CA

DEFENSE TECHNICAL INFORMATION CENTER
12 CYS ATTN: DD

FIELD COMMAND DNA DET 2
LAWRENCE LIVERMORE NATIONAL LAB
ATTN: FC-1

FIELD COMMAND DEFENSE NUCLEAR AGENCY
ATTN: FCTT
ATTN: FCTT W SUMMA
ATTN: FCTXE

JOINT CHIEFS OF STAFF
ATTN: C3S EVAL OFFICE (HDOO)

JOINT STRAT TGT PLANNING STAFF
ATTN: JLAA
ATTN: JLK (ATTN: DNA REP)
ATTN: JLKS
ATTN: JPTM
ATTN: JPTP

NATIONAL SECURITY AGENCY
ATTN: B432 C GOEDEKE

STRATEGIC DEFENSE INITIATIVE ORG
ATTN: KE
ATTN: SLKT
ATTN: SN
ATTN: SY

UNDER SECY OF DEF FOR RSCH & ENGRG
ATTN: DEFENSIVE SYSTEMS
ATTN: STRAT & SPACE SYS (OS)
ATTN: STRAT & THEATER NUC FOR F VAJDA

DEPARTMENT OF THE ARMY

HARRY DIAMOND LABORATORIES
2 CYS ATTN: SCHLD-NW-P

U S ARMY ATMOSPHERIC SCIENCES LAB
3 CYS ATTN: SLCAS-AE-E

U S ARMY BALLISTIC RESEARCH LAB
ATTN: SLCBR-SS-T TECH LIB

U S ARMY FOREIGN SCIENCE & TECH CTR
ATTN: DRXST-SD

U S ARMY INFO SYS ENGINEERING SUP ACT
ATTN: ASBH-SET-D W NAIR

U S ARMY MATERIAL COMMAND
ATTN: DRCLDC J BENDER

U S ARMY NUCLEAR & CHEMICAL AGENCY
ATTN: LIBRARY

U S ARMY RESEARCH OFFICE
ATTN: R MACE

U S ARMY STRATEGIC DEFENSE CMD
ATTN: DASD-H-SAV
ATTN: DASD-H-SAV R C WEBB

U S ARMY STRATEGIC DEFENSE COMMAND
ATTN: ATC-O W DAVIES
ATTN: ATC-R D RUSS
ATTN: ATC-R W DICKSON

U S ARMY TRADOC SYS ANALYSIS ACTVY
ATTN: ATAA-PL

DEPARTMENT OF THE ARMY (CONTINUED)

US ARMY MISSILE COMMAND
ATTN: DRSMI-YSO J GAMBLE

US ARMY WHITE SANDS MISSILE RANGE
ATTN: STEWS-TE-N K CUMMINGS

USA ELECT WARF/SEC SURV & TARG ACQ CTR
ATTN: AMSEL-EW-SS S KRONENBERG

DEPARTMENT OF THE NAVY

NAVAL AIR PROPULSION CENTER
ATTN: PE34 F HUSTED

NAVAL ELECTRONICS ENGRG ACTVY, PACIFIC
ATTN: CODE 250 D OBRVHIM

NAVAL OCEAN SYSTEMS CENTER
ATTN: CODE 532
ATTN: CODE 54 J FERGUSON

NAVAL POSTGRADUATE SCHOOL
ATTN: CODE 1424 LIBRARY

NAVAL RESEARCH LABORATORY
ATTN: CODE 2000 J BROWN
ATTN: CODE 2627 TECH LIB
ATTN: CODE 4128.2 J JOHNSON
ATTN: CODE 4139 D MCNUIT
ATTN: CODE 4180 J GOODMAN
ATTN: CODE 4700 W ALI
ATTN: CODE 4700 S OSSAKOW
ATTN: CODE 4720 J DAVIS
ATTN: CODE 4732 B RIPIN
ATTN: CODE 4780 D STROBEL
A J: CODE 4780 J HUBA

NAVAL SURFACE WEAPONS CENTER
ATTN: CODE X211 TECH LIB

NAVAL UNDERWATER SYS CENTER
ATTN: CODE 3411 J KATAN

SPACE & NAVAL WARFARE SYSTEMS CMD
ATTN: CODE 501A
ATTN: PD 50TD
ATTN: PDE-110-X1 B KRUGER
ATTN: PDE-110-11021 G BRUNHART
ATTN: PME 106-4 S KEARNEY

STRATEGIC SYSTEMS PROGRAMS(PM-1)
ATTN: NSP-L63 TECH LIB
ATTN: NSP-2141
ATTN: NSP-2722

THEATER NUCLEAR WARFARE PROGRAM OFC
ATTN: PMS-42331F D SMITH

DEPARTMENT OF THE AIR FORCE

AIR FORCE CTR FOR STUDIES & ANALYSIS
ATTN: AFCSA/SASC

AIR FORCE GEOPHYSICS LABORATORY
4 CYS ATTN: CA A STAIR
2 CYS ATTN: LID W SWIDER
ATTN: LIS J BUCHAU
2 CYS ATTN: LIU R HUFFMAN
ATTN: LS
2 CYS ATTN: LS R MURPHY
ATTN: LS R O'NIEL
ATTN: LSI H GARDINER
2 CYS ATTN: LSI R SHARMA
2 CYS ATTN: LSP D PAULSON
ATTN: LSP D SMITH
2 CYS ATTN: LSP R NADILE
2 CYS ATTN: LYD K CHAMPION

AIR FORCE OFFICE OF SCIENTIFIC RSCH
ATTN: AFOSR/NC
ATTN: ASOSR/NP MAJ JOHN PRINCE

AIR FORCE SYSTEMS COMMAND
ATTN: DLAE
ATTN: DLTW
ATTN: DLXP
ATTN: SDR

AIR FORCE TECHNICAL APPLICATIONS CTR
ATTN: CA
ATTN: TN
ATTN: TX

AIR FORCE WEAPONS LABORATORY, AFSC
ATTN: D H HILLAND
ATTN: SUL

AIR FORCE WRIGHT AERONAUTICAL LAB/AAAD
ATTN: A JOHNSON
ATTN: W HUNT

AIR UNIVERSITY LIBRARY
ATTN: AUL-LSE

DEPUTY CHIEF OF STAFF/AFRDS
3 CYS ATTN: AFRDS SPACE SYS & C3 DIR

ROME AIR DEVELOPMENT CENTER, AFSC
ATTN: OCD J SIMONS
ATTN: TSLD

STRATEGIC AIR COMMAND/INCR
ATTN: INCR

STRATEGIC AIR COMMAND/NRI-STINFO
ATTN: NRI/STINFO

DEPARTMENT OF ENERGY

EG&G, INC

ATTN: D WRIGHT

LAWRENCE LIVERMORE NATIONAL LAB

ATTN: L-10 A GROSSMAN
ATTN: L-262 D WUEBBLES
ATTN: L-31 R HAGER
ATTN: L-325 G HAUGAN
ATTN: L-48 E WOODWARD
ATTN: L-53 TECH INFO DEPT LIB
ATTN: L-71 J CHANG
ATTN: L-84 H KRUGER

LOS ALAMOS NATIONAL LABORATORY

ATTN: D SAPPENFIELD
ATTN: D SIMONS
ATTN: G M SMITH
ATTN: J WOLCOTT
ATTN: M PONGRATZ
ATTN: M SANDFORD
ATTN: MS J ZINN
ATTN: P364 REPORT LIBRARY
ATTN: R JEFFRIES
ATTN: R W WHITAKER ESS-5
ATTN: REPORT LIBRARY
ATTN: T BIENIEWSKI
ATTN: T KUNKLE ESS-5

SANDIA NATIONAL LABORATORIES

ATTN: C N VITTITOE
ATTN: D DAHLGREN
ATTN: L ANDERSON
ATTN: M KRAMM
ATTN: ORG 1231 T P WRIGHT
ATTN: ORG 314 W D BROWN
ATTN: ORG 332 R C BACKSTROM
ATTN: TECH LIB 3141 RPTS RCVG CLRK

OTHER GOVERNMENT

CENTRAL INTELLIGENCE AGENCY

ATTN: OSWR/NED
ATTN: OSWR/SSD FOR K FEUERPFETL

NATIONAL BUREAU OF STANDARDS

ATTN: A PHELPS

NATIONAL OCEANIC & ATMOSPHERIC ADMIN

3 CYS ATTN: E FERGUSON
3 CYS ATTN: F FEHSENFELD

U S DEPARTMENT OF COMMERCE

ATTN: G FALCON
ATTN: W UTLAUT

DEPARTMENT OF DEFENSE CONTRACTORS

AUSTIN RESEARCH ASSOCIATES

ATTN: J THOMPSON

BERKELEY RSCH ASSOCIATES, INC

ATTN: C PRETTIE
ATTN: J WORKMAN
ATTN: S BRECHT

BOEING CO

ATTN: D CLAUSEN

COMPUTER SCIENCES CORP

ATTN: F EISENBARTH

ELECTROSPACE SYSTEMS, INC

ATTN: P PHILLIPS

EOS TECHNOLOGIES, INC

ATTN: B GABBARD
ATTN: W LELEVIER

GENERAL ELECTRIC CO

ATTN: R EDSALL

GEO CENTERS, INC

ATTN: E MARRAM

GTE GOVERNMENT SYSTEMS CORPORATION

ATTN: A MURPHY

HARRIS CORP

ATTN: E KNICK

HSS, INC

ATTN: D HANSEN
ATTN: M SHULER

INSTITUTE FOR DEFENSE ANALYSES

ATTN: E BAUER
ATTN: H WOLFHARD

JAYCOR

ATTN: J SPERLING

JOHNS HOPKINS UNIVERSITY

ATTN: C MENG
ATTN: K POTOCKI

KAMAN SCIENCES CORP

ATTN: E CONRAD

KAMAN TEMPO

ATTN: B GAMBILL
5 CYS ATTN: DASIAC
ATTN: W MCNAMARA

KAMAN TEMPO

ATTN: DASIAC

M I T LINCOLN LAB

ATTN: D TOWLE

DEPT OF DEFENSE CONTRACTORS (CONTINUED)

MAXIM TECHNOLOGIES, INC

ATTN: J LEHMAN
ATTN: J MARSHALL
ATTN: J SO
ATTN: R MORGANSTERN

METEOR COMMUNICATIONS CORP

ATTN: R LEADER

MISSION RESEARCH CORP

ATTN: B R MILNER
ATTN: C LAUER
ATTN: D ARCHER
ATTN: D KNEPP
ATTN: D SOWLE
ATTN: F FAJEN
ATTN: F GUIGLIANO
ATTN: G MCCARTOR

2 CYS ATTN: L NICKISCH
ATTN: M SCHEIBE
ATTN: R BIGONI
ATTN: R BOGUSCH
ATTN: R DANA
ATTN: R HENDRICK
ATTN: R KILB
ATTN: S GUTSCHE

2 CYS ATTN: TECH LIBRARY

MISSION RESEARCH CORP

ATTN: C LONGMIRE
ATTN: R PETERKIN
ATTN: R STELLINGWERF

MITRE CORP

ATTN: R DRESP

MITRE CORP

ATTN: J WHEELER
ATTN: R C PESCI
ATTN: W FOSTER

PACIFIC-SIERRA RESEARCH CORP

ATTN: H BRODE, CHAIRMAN SAGE

PHOTOMETRICS, INC

ATTN: I L KOFSKY

PHYSICAL DYNAMICS, INC

ATTN: E FREMOUW

PHYSICAL RESEARCH, INC

ATTN: R DELIBERIS
ATTN: T STEPHENS

PHYSICAL RESEARCH, INC

ATTN: J DEVORE
ATTN: J THOMPSON
ATTN: W SCHLUETER

PHYSICAL SCIENCE LAB

ATTN: W BERNING

R & D ASSOCIATES

ATTN: F GILMORE
ATTN: M GANTSWEG
ATTN: W KARZAS

R & D ASSOCIATES

ATTN: G GANONG

RAND CORP

ATTN: C CRAIN
ATTN: E BEDROZIAN
ATTN: P DAVIS

SCIENCE APPLICATIONS INTL CORP

ATTN: D HAMLIN
ATTN: L LINSON

SCIENCE APPLICATIONS INTL CORP

ATTN: R LEADABRAND

SCIENCE APPLICATIONS INTL CORP

ATTN: D TELAGE
ATTN: M CROSS

SRI INTERNATIONAL

ATTN: D MCDANIEL
ATTN: W CHESNUT
ATTN: W JAYE

TECHNOLOGY INTERNATIONAL CORP

ATTN: W BOQUIST

TELECOMMUNICATIONS SCIENCES ASSOCIATES

ATTN: R BUCKNER

TOYON RESEARCH CORP

ATTN: J GARBARINO
ATTN: J ISE

VISIDYNE, INC

ATTN: J CARPENTER

DIRECTORY OF OTHER

GOVERNMENT PUBLICATIONS LIBRARY-M

ATTN: J WINKLER

YALE UNIVERSITY

ATTN: ENGINEERING DEPT